2011

An Experimental Investigation On The Dynamics Of Bubbles Utilizing Refrigerant R134a Under Pressurized Flow Boiling Conditions

Keon Vereen
University of Central Florida

STARS Citation
Vereen, Keon, "An Experimental Investigation On The Dynamics Of Bubbles Utilizing Refrigerant R134a Under Pressurized Flow Boiling Conditions" (2011). *Electronic Theses and Dissertations, 2004-2019*. 1723.
https://stars.library.ucf.edu/etd/1723

AN EXPERIMENTAL INVESTIGATION ON THE DYNAMICS OF BUBBLES UTILIZING REFRIGERANT R134A UNDER PRESSURIZED FLOW BOILING CONDITIONS

by

KEON VEREEN
B.S.A.E University of Central Florida, 2010

A thesis submitted in partial fulfillment of the requirements
for the degree of Master in Science in Aerospace Engineering
in the department of Mechanical, Materials and Aerospace Engineering
in the College of Engineering and Computer Science
at the University of Central Florida
Orlando, Florida

Fall Term
2011

ABSTRACT

Flow boiling heat transfer allows for the dissipation of large amounts of heat. In this work, the effect of heat flux and pressure on flow boiling of liquid refrigerant R-134a is studied in a vertical thin channel. The experimental setup mimics a refrigeration cycle and specifically looks at the effect of pressure and wall heat flux on the departure size and bubble generation rate.

The experimental setup consists of a closed loop which includes a vertical narrow rectangular channel and two synchronized high speed cameras for optical measurements at either sides of the channel. The setup is built to employ an accurate measurement technique to define wall temperatures of the representative flow boiling process. Instead of using thermocouples on the surface channel, the thermochromic liquid crystallography (TLC) technique is used to determine non-invasively the heater surface temperature at high temporal and spatial resolution. The TLC interval range is 30-50°C. The TLC is attached to a Fecralloy heating section. The high speed Prosilica cameras simultaneously capture, colored TLC images as well as bubble nucleation and departure at very high frame rates. Experiments on subcooled flow boiling heat transfer have been conducted with refrigerant R-134a under a mass flux range of 484.838 kg/m^{2}s to 1212.1 kg/m^{2}s. With the low mass flux, the wall heat flux ranged from 167.2 to 672.1 kW/m^2, the inlet subcooling ranged from 0.35°C to 16.55 °C, the system pressure ranged from 621 kPa to 1034 kPa. At high mass flux, the wall heat flux ranged from 329.8 kW/m^2 to 744 kW/m^2, the inlet subcooling from 0.16°C to 17.21 °C, and the system pressure from 621 kPa to 1034 kPa. A parametric study was done by maintaining various input parameters constant.

From the high speed images, bubble parameters such as size and frequency are calculated. Temperature contours are utilized to determine the surface wall temperature at specific points. Sequential wall temperatures are traced over a short period of time to understand the cooling effects. The bubble propagation and coalescence are also visualized. Results show that bubble size and frequency increased with heat flux at any particular pressure. At higher pressure, the trend would be for the bubble size to decrease; however, the inlet subcooling and heat flux also affect bubble size. The bubble frequency is also seen to be affected by the inlet subcooling and the heat flux. Even though the inlet subcooling is maintained approximately constant, any slight decrease in subcooling increased bubble growth rate. Another trend that is observed is that at higher the heat flux, the bubble generation frequency is faster; however no specific trend is observed for wall superheat. With an increase in heat flux, the wall superheats are expected to increase; however, the localized nature of the nucleation activity sites is seen to affect the results. The variables are non-dimensionalized to note trends in parameters. In summary, the data analysis demonstrates that both heat flux and pressure significantly influence the bubble generation rate, size, propagation and coalescence.

ACKNOWLEDGMENTS

I would like to give my deepest appreciation to my adviser Dr. Ranganathan Kumar who gave me invaluable guidance and opportunities while working in the two phase flow group. I became a better researcher under his mentorship. I would also like to give thanks to my lab mates Ben Patrick, Josh Lee, Ahbishek Saha, and Ehsan Yakhsi-Tafti who provided insight on conducting graduate level research. I greatly appreciate the funding Knolls Atomic Power Laboratory (KAPL) provided us for the research on flow boiling heat transfer. I also want to give a special thanks to those individuals who contributed heavily toward the KAPL project which set a solid foundation for me to continue the research. Special thanks are in order for Dr. Sohel Murshed, Jim Strater, and Daniel Joo. I would also like to thank the graduate school for providing me with the RAMP Master's Fellowship. By having this fellowship, I was able to stay focused on my coursework and heavily on my research. The McNair program provided me with constant positive encouragement. I would also like to thank my parents and external family for the constant support. Once again, thank you all it is greatly appreciated.

TABLE OF CONTENTS

LIST OF FIGURES

LIST OF TABLES

CHAPTER ONE: INTRODUCTION

In order to design better cooling devices such as heat exchangers, the principles of flow boiling heat transfer need to be understood. During nucleate boiling “bubbles are formed over the cavities that are present on a heater surface” [26]. The bubbles grow until they reach some critical size at which point they are separated from the wall and are carried into the main fluid stream. The bubbles collapse in the bulk fluid due to subcooling. The importance and relevance of flow boiling heat transfer, specifically nucleate boiling, are its application to electronic cooling, pressurized reactors and in any application where a heat exchanger is used.

With the necessity for higher heat fluxes, thermal designers have to consider refrigerant flow boiling over air cooling to dissipate heating [30]. Comparing single phase flow such as air cooling, refrigerant flow boiling is useful due to the fluids’ heat of vaporization [34]. Moreover, the incipience of boiling occurs when there is a considerable rise in wall temperature above the saturation temperature [47]. This temperature overshoot is called the degree of superheat. By understanding this degree of superheat, thermal designers can avoid Critical Heat Flux (CHF) and the subsequent catastrophe in applications ranging from electronics to pressurized reactors. Designers want systems that are efficient, safe, and cost-effective. By having high heat transfer coefficients, large heat fluxes can be dissipated [47]. High heat transfer coefficients allow for an enhancement in efficiency.

This present experiment investigated flow boiling of refrigerant R-134a in a vertical high aspect ratio channel. In order to determine accurate surface temperature measurements, a sandwich formation of TLC and Fecralloy heating foil are utilized. Various bubble parameters at pressure ranges varying from 621-1034 kPa (90-150psi) are investigated. In order to analyze the data from this flow boiling heat transfer research, a proper literature review is conducted. The literature review will include thermochromic liquid crystallography and flow boiling heat transfer.

CHAPTER TWO: LITERATURE REVIEW

Thermochromic Liquid Crystallography

The importance of thermochromic liquid crystals is that they can be used for various applications where heat is applied and therefore gives a certain color represented by a hue angle that corresponds to a certain temperature. The three groups of liquid crystals are sematic, nematic and cholesteric. Cholesteric liquid crystals are seen to be the most versatile out of the three because of its ability to be encapsulated which extends the life of the TLC as well as reduce color variation [25, 45]. The temperature range for an encapsulated liquid crystal is from -30°C to 115°C. The narrowest color-play interval is 1°C while the widest is about 20°C [22]. The TLC color interval ranges from red, yellow, green, blue, and violet. The TLC is black below and above the color interval [53]. The wavelength of reflected light falls within the visible color spectrum and the hue angle. The hue angle varies with temperature within a certain temperature range which provides high resolution thermal mapping [52]. When dealing with complex applications, for instance at the microscale level, traditional sensors such as thermocouples or resistance thermometers might be intrusive and would impede the flow; Therefore, TLCs provide a reliable and repeatable method that is non-intrusive [17]. The liquid crystals have a constant response time of about 3ms which depends on experimental conditions as well as the sophistication of image processing software [21, 23]. . Many researchers chose between two types of calibration methods for liquid crystals to calibrate hue angle versus temperature [7]. There is the narrow-band technique which employs liquid crystals with a narrow activation bandwidth (1° or less) where a single color is chosen like yellow to reduce uncertainty [52]. The other method is known as point wise technique or wide band technique. This technique establishes the relationship between the hue and temperature for each position on the sensing surface. The resulting array of calibration curves converts data images from hue to temperature in a point-wise manner with high accuracy [50]. Other researchers have compared steady state and transient techniques on film cooling measurements, concluding that transient technique reduces the uncertainty with multiple sampling whereas steady state has uncertainty [12, 37, and 58]. When looking at the transient technique for calibrating thermochromic liquid crystals, hysteresis is only an issue when the crystals are heated well above their color-play interval. As long as TLCs are kept within the color-play interval, calibrations will be quite repeatable with minimal degradation of the liquid crystal [2, 4]. When looking at evaporating liquid meniscus, TLCs enable temperature measurement at high spatial resolution. The local cooling caused by the strong evaporation in the microregion on the stainless steel foil can be observed by a temperature drop in the wall at the microregion [8, 19]. By using analysis of liquid crystal images, the local temperature-time series can be identified for analysis of nucleation sites. High speed TLCs provide important mechanisms of interaction between bubble nucleation and the heat transfer driven by bubble motion [32].

Flow Boiling Heat Transfer Studies

Tran et.al, 1997 addressed nucleate flow boiling in small channels. The researchers made an assessment that nucleation is the dominant heat transfer mechanism over a broad range of heat flux and wall superheats. Local heat transfer coefficients and overall two phase pressure drops are measured for three different refrigerants in a range of pressures. Based on the results, researchers believe that forced convection region needs to be studied because this region dominates at low mass flux, high quality, and low wall superheat [57]. Thorncroft et al, 1998 presented experimental investigation of bubble growth and detachment in vertical upflow and downflow boiling. They presented a visual study to observe the bubble growth and departure in a flowing system where forced convection boiling occurred. The researchers used FC-87 and had a range of mass fluxes and a range of heat fluxes used in the experiment. Based on some results, vapor bubble lift-off is not generally observed in upflow boiling, but only in downflow boiling [55]. Steinke and Kandlikar, 2004 focused on obtaining the fundamental heat transfer data and two phase flow patterns presented during flow boiling in microchannels. The researchers performed an experimental investigation by using water in six parallel, horizontal microchannels. There are ranges for mass flux and heat flux. Using flow visualization, researchers are able to observe flow reversal due to bubble nucleation. According to their results, the local heat transfer coefficient had a negative trend with an increase in quality. The role of nucleate boiling in microchannels is more prevalent than previously thought [54]. Mudawar, 2001 explored high heat flux thermal management schemes. Cooling schemes such as pool boiling, detachable heat sinks, channel flow boiling, microchannel and minichannel heat sinks, jet impingement, and sprays have also been addressed in the literature. Whenever there is high heat flux, there is a need for novel heat dissipation techniques to solve challenging thermal problems. The researcher addressed the need to enhance the critical heat flux using methods such as surface enhancement, high coolant velocity, and subcooling [41]. Dhir's, 1998 review on boiling heat transfer addresses concepts in nucleate boiling, maximum heat flux, transition boiling, film boiling, minimum heat flux, pool boiling, and flow boiling.. Peng et.al, 1998 addressed bubble nucleation during liquid flow in microchannels.

The purpose of this current study is to understand the boiling characteristics and determine the conditions for liquids to undergo phase changes. The fundamental thermodynamics and interaction of bubble growth provides criterion for phase change of liquids. From this study, there needs to be more experiments conducted to coincide with the theoretical conclusions [46]. Auracher and Buchholz, 2005 discussed experiments on the fundamental mechanisms of boiling heat transfer. Their results highlighted dry spot geometry, dynamics, and stability of boiling mechanisms. They also addressed the two phase behavior above the heater to explain void fraction distribution [3]. Qu and Mudawar, 2003 published their paper on flow boiling heat transfer in two phase microchannel heat sinks. The purpose of their study is concerned with measurement and prediction of saturated flow boiling heat transfer in water cooled design such that the microchannel heat sink contained 21 parallel channels using deionized water. A parametric study was conducted based on mass velocity range, inlet temperatures, and outlet pressure. Based on these results, the correlations for the experiment could not be determined to predict the correct trends for the heat transfer coefficient [49]. Kandlikar et al, 2001 conducted an experiment to explore the flow regimes during flow boiling of water in mini-channels. High speed cameras are used for flow visualization to capture flow phenomena from subcooled flow boiling all the way to critical heat flux conditions. The experimental system consisted of a reservoir, a pump, valves, flow meters, a test section, a condenser, a coolant inlet, and thermocouples. Based on the results, there are large pressure fluctuations, slug growth, reverse flow, and annular flow [31]. Zhang et.al, 2004 performed an experiment in the pursuit of identifying the trigger mechanism for subcooled flow boiling critical heat flux (CHF). This study was focused on the events that take place at the CHF transient. The researchers used high speed cameras and image analysis software to explore vapor formation during CHF transient. From the results, they were able to effectively estimate the void fraction and vapor layer. The development of a wavy vapor layer propagates along the heated wall permitting cooling. The CHF transient is accompanied by gradual lift-off of wetting fronts. From the study, the interfacial lift-off model was found to be equally valid for subcooled flow boiling CHF as it is for saturated conditions [60]. Hohmann and Stephan, 2002 created an experiment for a microscale temperature measurement technique to investigate the heat transfer at an evaporating liquid meniscus. The experimental setup includes a single capillary slot created by two flat parallel plates. The plates have a foil and liquid crystal combination. A CCD camera and microscope were used to observe the phenomena. From the results, the high evaporation rate in the contact line region leads to a local cooling of the surface. A representation of the microregion effect was detected [19]. Kenning and Yan, 1996 created an experiment to investigate pool boiling heat transfer on a thin plate. The liquid used was water on a thin plate that was electrically heated. High speed photography and thermochromic liquid crystals were used to capture bubble phenomena as well as to observe the contour plot region as the bubble grows and departs from the wall. From the results, the researchers were able to conclude that at a given heat flux, each nucleation site has a characteristic nucleation superheat [33]. Hsieh et.al, 2001 conducted this study in order to observe subcooled flow boiling heat transfer characteristics of refrigerant R-134a in a vertical plate heat exchanger. The experiment system consisted of a refrigerant loop, two water loops, a cold water glycol loop, and a data acquisition system. The boiling curves change significantly with the onset of nucleate boiling. There are drastic changes when there is low mass flux and high saturation temperature. From flow visualization, the researchers indicated that higher heat fluxes corresponds to more bubble being covered on the plate bubble generation frequency is higher and bubbles tend to coalesce to form bigger bubbles [20]. Lee and Mudawar, 2004 investigated two phase flow and heat transfer characteristics of R-134a in microchannel heat sink incorporated as an evaporator in a refrigeration cycle. There is a controlled heat flux, vapor quality over a range of mass velocity. This study indicated that there are different mechanisms associated with heat transfer: low, medium, high quality. They found that nucleate boiling process occurs only at low quality corresponding to low heat fluxes whereas high heat fluxes corresponds to medium, high quality dominated by annular film evaporation [36].

CHAPTER THREE: MATERIALS AND METHODOLOGY

Design and fabrication of experimental facility

An experimental facility is designed and fabricated to investigate the vertical flow boiling of refrigerant R134a at pressurized environment. Experimental setup consists of three major parts: test section, flow loop, and cameras (extender tubes, light emitting diodes) for flow visualization and TLC image recording. The test section is made of acrylic plate which contains thin rectangular flow channel (46 cm length, 3.8 cm width, and 3 mm depth), heater, and TLC sheet. The test section can withstand high pressure up to 2.1MPa (304.5 Psi) and the flow loop comprises of tube, pump, intercooler, pressure sensor, and flow regulators. Intercooler and flow regulator allow regulating both the pressure and flow rate of the refrigerant. Schematic of entire experimental setup is shown in Figure 1.

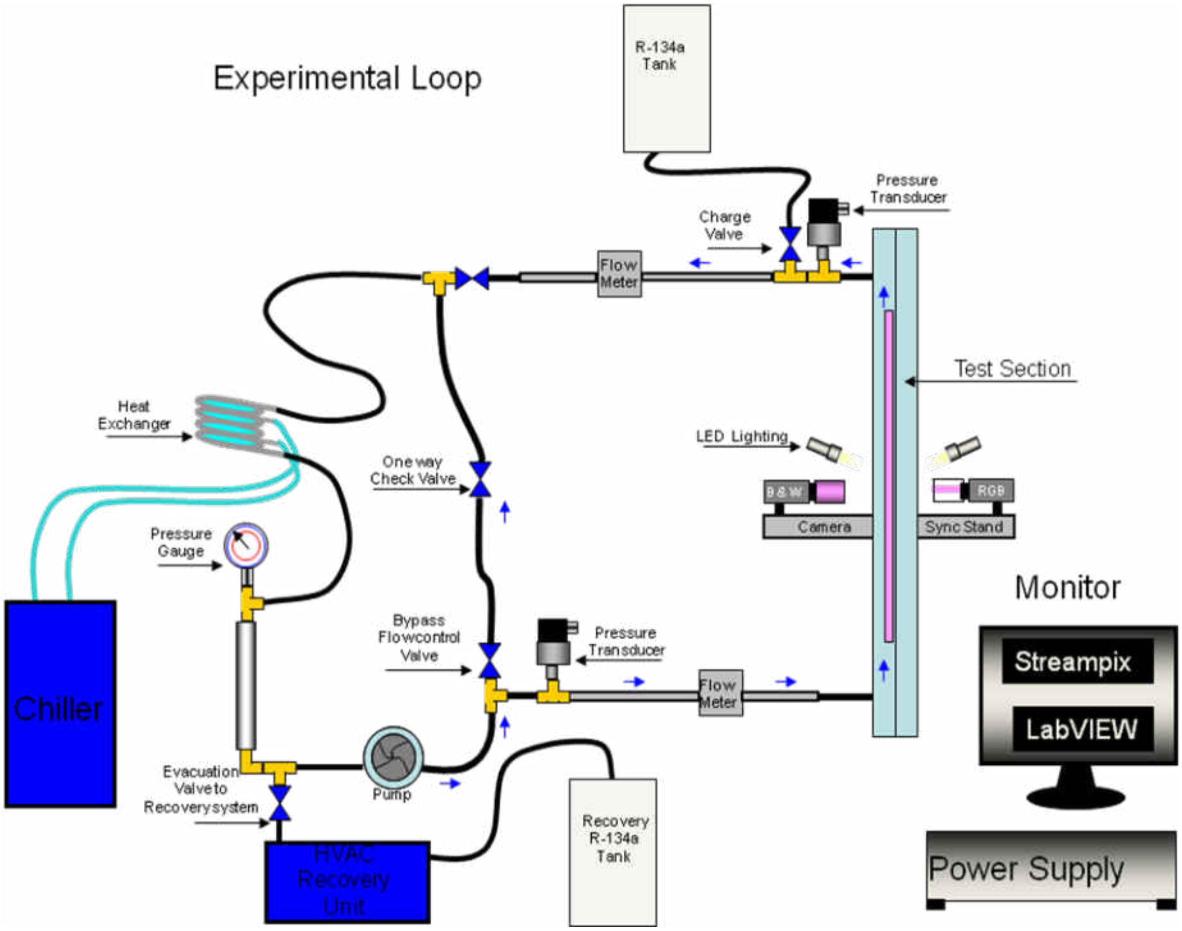

Figure 1: Experimental Setup

Test section and flow loop.

The test section is clear enough for front, back and side visual access to the TLC, instrumentation, and bubbles. The test section also allows for easy physical access to the TLC, heater, and thermocouples. An exploded view of test section is shown in Figure 2. An acrylic insert-plate which contains heater foil, TLC and thermocouple located at the middle of Cap and Flow sections (Figure 2). The test section is made of three parts which are Flow section, the Instrumentation acrylic insert plate, and the Cap section. The acrylic insert plate has a dimension of 0.635 cm thick × 7.62 cm × 45.72 cm and is attached to the TLC with the heater foil. The hydraulic diameter, D_h, is 5.86 mm and is characteristic of a conventional channel. For accurate reflection of heater surface temperature to TLC, very thin (50 µm) Fecralloy (Iron, Chromium, and Aluminum alloy) heating foil is used. The heater surface area for boiling activity measures 1 × 1 cm^2.The length of the flow channel is 60.7 cm. There are numerous methods that have been attempted to bond the heating foil to the TLC and the TLC to the insert plate. The best method found is to use a two part epoxy to glue the foil to the TLC and silicon based transparent semi-permanent adhesive to glue the TLC to the acrylic insert plate.

Figure 3 shows a CAD drawing of the flow section. The acrylic plate holder edge is 0.635 cm deep, which is the same thickness as the acrylic insert plate. Therefore, the plate sets into the flow section, and is flush with the flow section upper surface. This allows for a thin flow channel below the plate. Liquid R-134a can easily flow into the slot through the hole at the bottom of the flow section and moves through the flow straighteners (thin channels machined into acrylic). It then passes an open region before exiting at the top of the flow section. Figure 4 shows a schematic of the heater design. This butterfly shape design is necessary in order to direct the heat toward the center, particularly the region of interest (ROI). Figure 5 shows the sandwich formation of TLC and Fecralloy heating foil. The TLC and Fecralloy region of interest are portrayed. The onset of nucleate boiling will take place within this region.

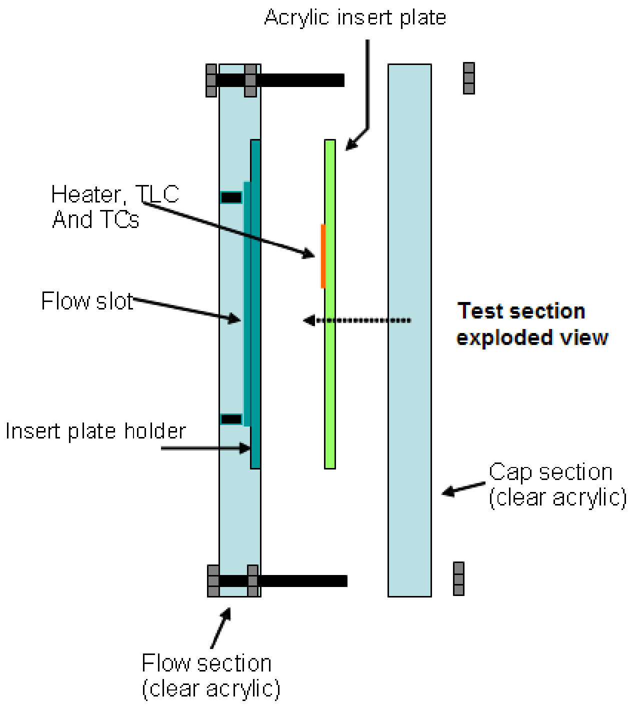

Figure 2: Exploded View of Test Section

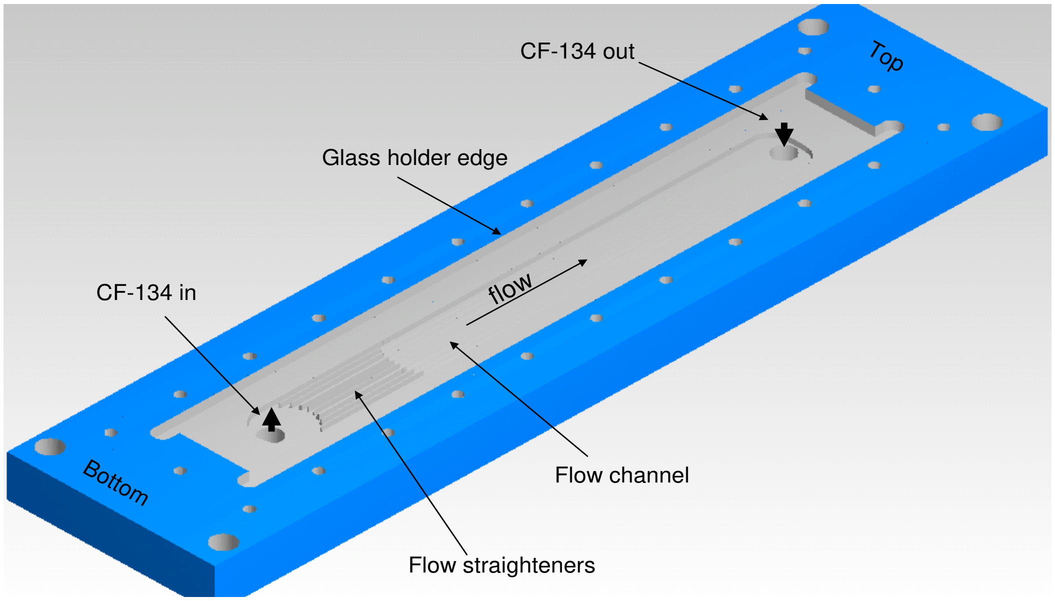

Figure 3: CAD Drawing of Flow Section

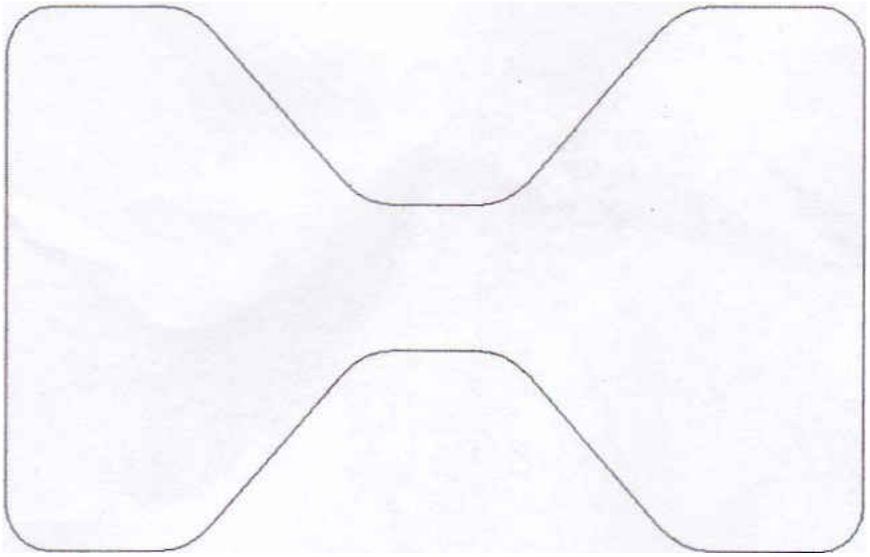

Figure 4: Butterfly Design of Heating Element

Figure 5: TLC and Fecralloy Heating Foil Combination; Boiling Activity ROI is shown

Experimental methodology

The first step before conducting test is to make sure that the loop can maintain the operating pressure. A pressure pump is used to pump the loop up to the appropriate pressure. After the pressure holds for about sixty minutes, a vacuum pump is turned on to vacuum all of the pressure out of the loop. This is a necessary step because there cannot be any contamination with the R-134a. After the vacuum pump has been running for a while, all lines are closed off. We then check to make sure that the proper valves are open or close and there is no more air pressure in the loop. The R-134a tank is placed at the top of the loop on a mount. The line is connected and the charge valve opens to allow the R-134a to change from the gaseous phase to the liquid phase in the loop. Once the R-134a has filled the loop, the test is ready to begin. A more detailed experimental setup can be found in the appendix section. R-134a loop pressure is varied by controlling chiller's temperature and flow rate is changed by bypass flow control valve. Using DC power supply (BK Precision regulated DC power supply with output of 0-30Volt and 0-30Amp), the surface of the heating section is heated to a temperature beyond the R-134a saturation temperature at a particular operating pressure. When loop is held at any desired constant pressure, flow pump is turned on to run the experiments. The heat flux is adjusted through the power supply to reach certain heat flux. Rising through the test section, the R-134A is heated and changes to a saturated fluid. In the test section, the flow and the TLC are imaged with high speed cameras. The saturated R-134A flows out through the top of the test section where long tube separates the gaseous and liquid portions of the fluid, and the gas flows through a water-cooled heat exchanger condensing to liquid. All of the liquid recombines and is pumped back to the bottom of the test section. When R-134a starts boiling and generates bubble; both cameras are run at certain frame rate to capture the bubbling events and TLC images simultaneously. Recorded images are saved in computer based on real-captured time in millisecond. Thus for same frame rate of both cameras, it can easily give the TLC image (RGB) of corresponding bubble image (BW) at any particular time leading to determine time-based temperature and bubble characteristics. Inlet temperature and system pressure are measured with thermocouples and pressure sensors, respectively. Figures 6-14 display the equipment necessary to run this experiment.

Suva tank and scale   Suva recovery system   Chiller

Figure 6: Experimental Equipment 1

Leak detector Recovery Tank Heat exchanger

Figure 7: Experimental Equipment 2

Figure 8: Experimental Equipment 3: Yellow Jacket Manifold (Left) and High Pressure Refrigerant Flow meter (Right)

Power supply HS Camera

Figure 9: Experimental Equipment 4: Flow Meter Power Supply (Left) and High Speed (HS) Prosilica Camera (Right)

Figure 10: Experimental Equipment 5: Single LED Module (Left) and LED Controller Box (Right)

Figure 11: Experimental Equipment 6: BK Precision High Current DC Regulated Power Supply (0-32V/0-30A)

Figure 12: Experimental Equipment 7: Platinum JB (2 Stage) Vacuum Pump (Left) and Procon Pump with Motor (Right)

Figure 13: Experimental Equipment 8: NI cDAQ 9172 chassis (Left), NI 9211 module (Middle), and NI 9203 module (Right)

Figure 14: Experimental Equipment 9: Chicago Electric Power Tools Heat Gun #47269 (Left) and a Husky 1.5Gal 135psi Max Compressor (Right)

Discharge of R-134a after experiments

After the experiment has run and collected data, R-134a is discharged into a recovery tank that is connected to a recovery pump that takes all the R-134a out of the loop. The recovery pump works in similar manner as the vacuum pump except that this pump is used primarily for refrigerants. All valves are open to make sure that all of the R-134a is going into the recovery tank. This process has to be done meticulously because there should not be any R-134a leaking into the air. The R-134a can be dangerous if a lot of R-134a is leaked into the air. After a while, the pressure gauges should indicate that the R-134a has been completely vacuumed. A more detailed discharge procedure is shown in the appendix section.

Calibration details

Before performing boiling experiments it is the first key step to calibrate the TLC in order to determine the heater surface temperature accurately. As mentioned before, from TLC color image we can get hue value which is correlated with temperature value obtained by using thermocouple or any other means. In order to use TLC for temperature measurement, hue versus temperature relationship is first established through *in-situ* calibration. Then this calibrated relation between hue and temperature is used to obtain the temperature data for experimental runs. The process for calibrating the TLC can be shown in the figure below.

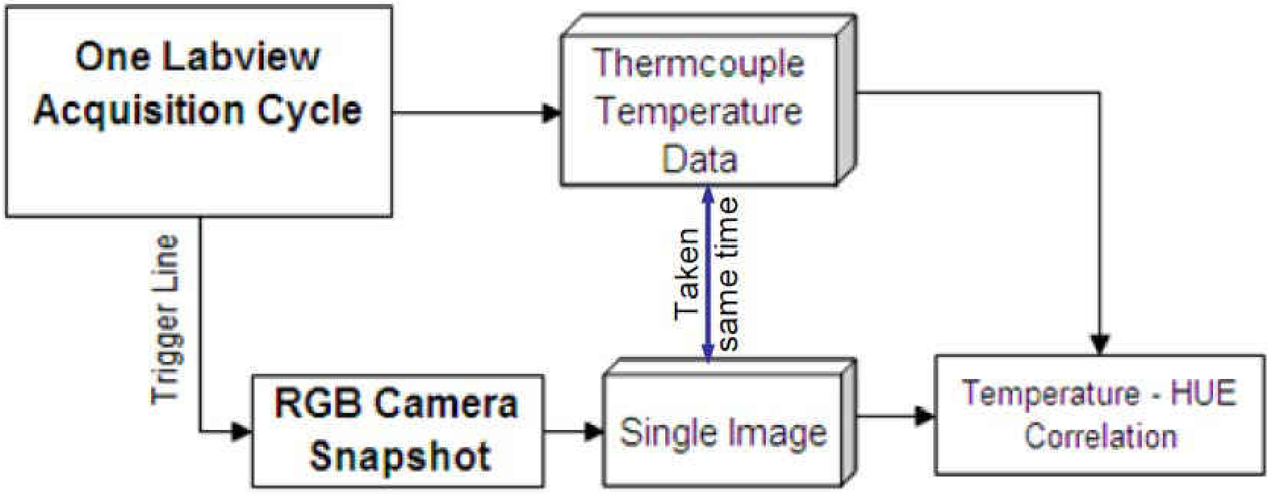

Figure 15: TLC Calibrating Process

The TLC attached behind the heater surface is calibrated in the temperature range of 30 ºC- 50 ºC which is within the R-134A boiling temperature at present experimental pressures.

For calibrating the TLC, a thermocouple is placed onto the butterfly heating element section which has dimensions of 6 cm × 4 cm. Within the butterfly section, the thermocouple is placed within the region of interest where heating will commence. The region of interest is 1 cm x 1 cm. The thermocouple is placed on a (x, y) coordinate that is utilized when capturing the TLC images from the high speed camera. The (x, y) location is important for finding the correct region of interest (ROI). Without the correct ROI, the temperature values from the thermocouple would not match the hue angles from the TLC images. The heating section is brought to 50° C by using a constant power source of 2.0 V x 5.0A and then slowly cooled while acquiring temperature readings and TLC images. Temperature is recorded using the K-type calibrated thermocouple through a LabVIEW DAQ template and the RGB camera captured the TLC images at the location of thermocouple. Both images and thermocouple readings are taken simultaneously at every 100 milliseconds. The hue angle of the TLC is calculated from the RGB (Red, Green and Blue) values of the individual pixels within an image:

$$h \equiv \arctan(\frac{\sqrt{3}(G-B)}{2R-G-B})$$

A customized GUI software is used to obtain hue value from the TLC images and corresponding recorded temperature values (same time) are obtained from LabVIEW.

A typical calibration curve of C. Hohmann and P. Stephan is given in Figure 16. The range of temperatures on this TLC is 26°C-34°C. The current TLC range is 30°C-50°C. It represents the widest interval band width.

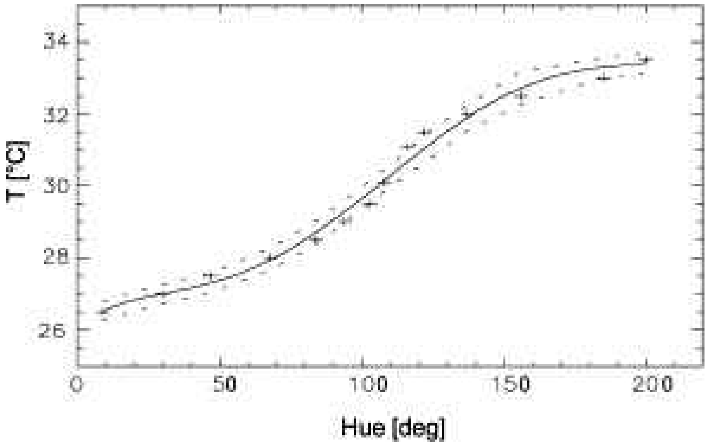

Figure 16: Calibration Curve by C. Hohmann and P. Stephan observing temperatures ranging from 26°C to 34°C [19].

The hue values and temperatures are plotted and a least square regression is performed to get the best ($R^2 = 0.98815$) polynomial fit (fifth order) of the data (Figure 17). The co-relation between hue (x) and temperature (y) obtained from the calibration is as follows:

$$y = 1.1658E\text{-}09x^5 - 4.4119E\text{-}07x^4 + 8.0335E\text{-}05x^3 - 7.5859E\text{-}03x^2 + 3.7567E\text{-}01x + 2.6700E{+}01$$

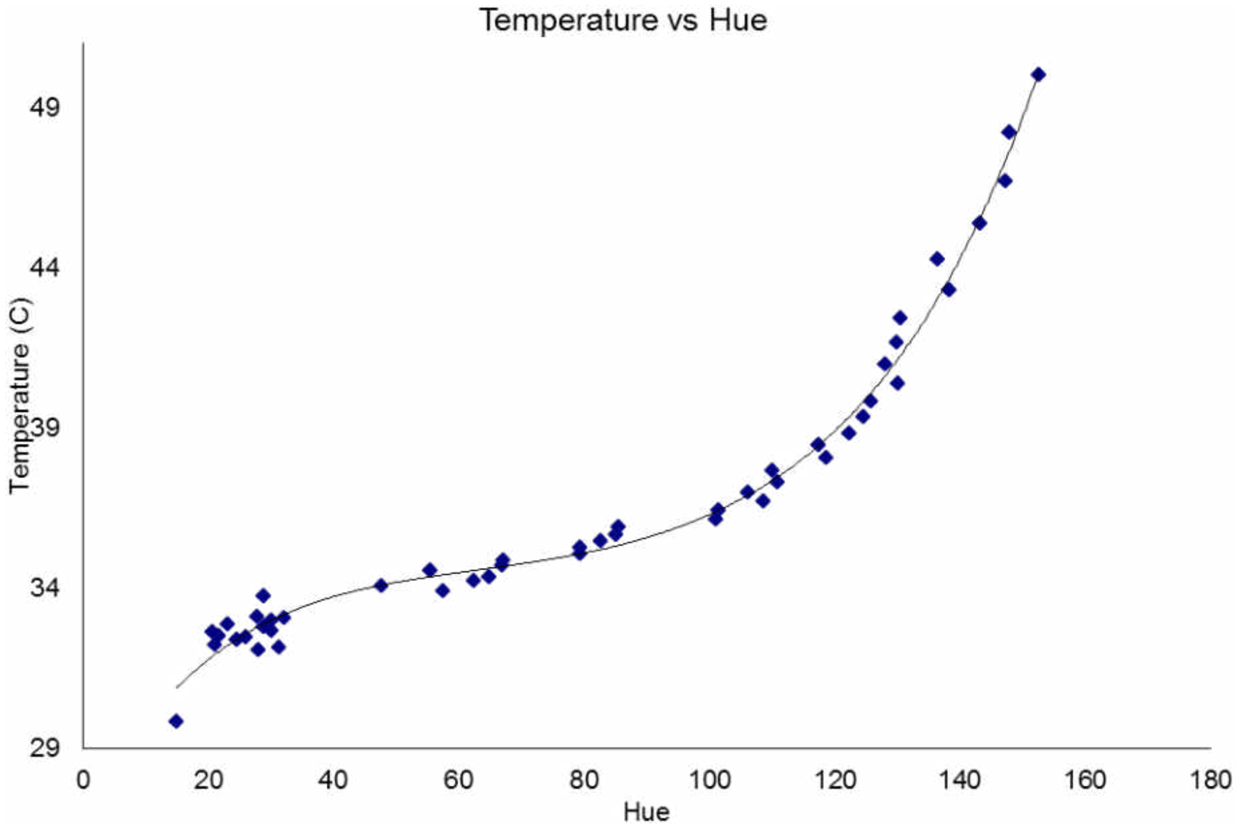

Figure 17: Experimental Calibration Curve ranging from 30°C-50°C.

Data acquisition and post-processing

Data acquisition starts by triggering both cameras to record images at their set frame rate. Simultaneously temperature and flow rate data collection are also triggered by LabVIEW. After stopping or pausing data recording the data can be permanently stored in raw format or exported to bitmap file for post-processing. As mentioned previously, the visualization and image recording process is performed by employing two synchronized high resolution and high speed cameras which simultaneously capture colored TLC images as well as bubble nucleation and departure at high frame rates. Although the Prosilica cameras used in this study are capable of capturing as high as 1000 frames per second (fps), the frame rate is limited to 400 fps in order to capture the bubbling event in larger region. The Streampix 4 recording software is used for image recording using these two cameras. While a LabVIEW software works as data and image acquisition system, a customized Matlab program is used to post-process the images which include determining hue angle from TLC images, bubble size, location and frequency. The diagram for data and image acquisition can be shown below in Figure 18. The LabVIEW logic and software interface can be shown in Figures 19 and 20. Figure 21 outlines the process for post processing. Figure 22 displays the GUI interface used to post process TLC images.

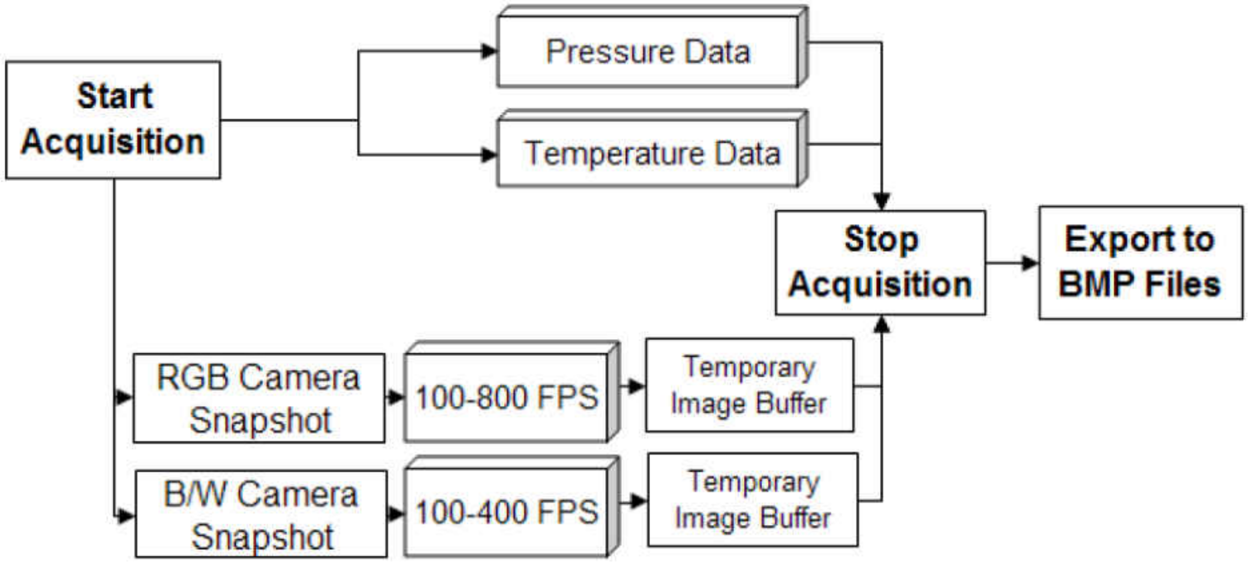

Figure 18: Data and Image Acquisition Diagram

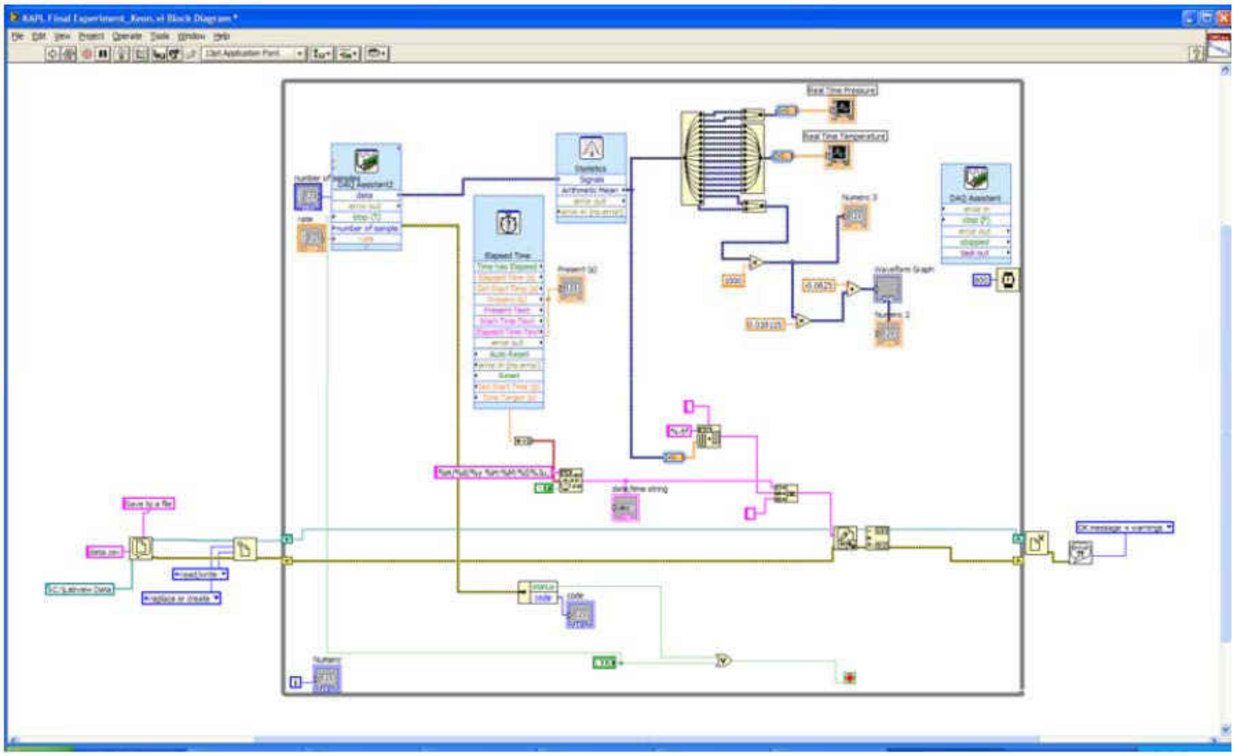

Figure 19: LabVIEW logic for pressure, inlet temperature, and flow rate register

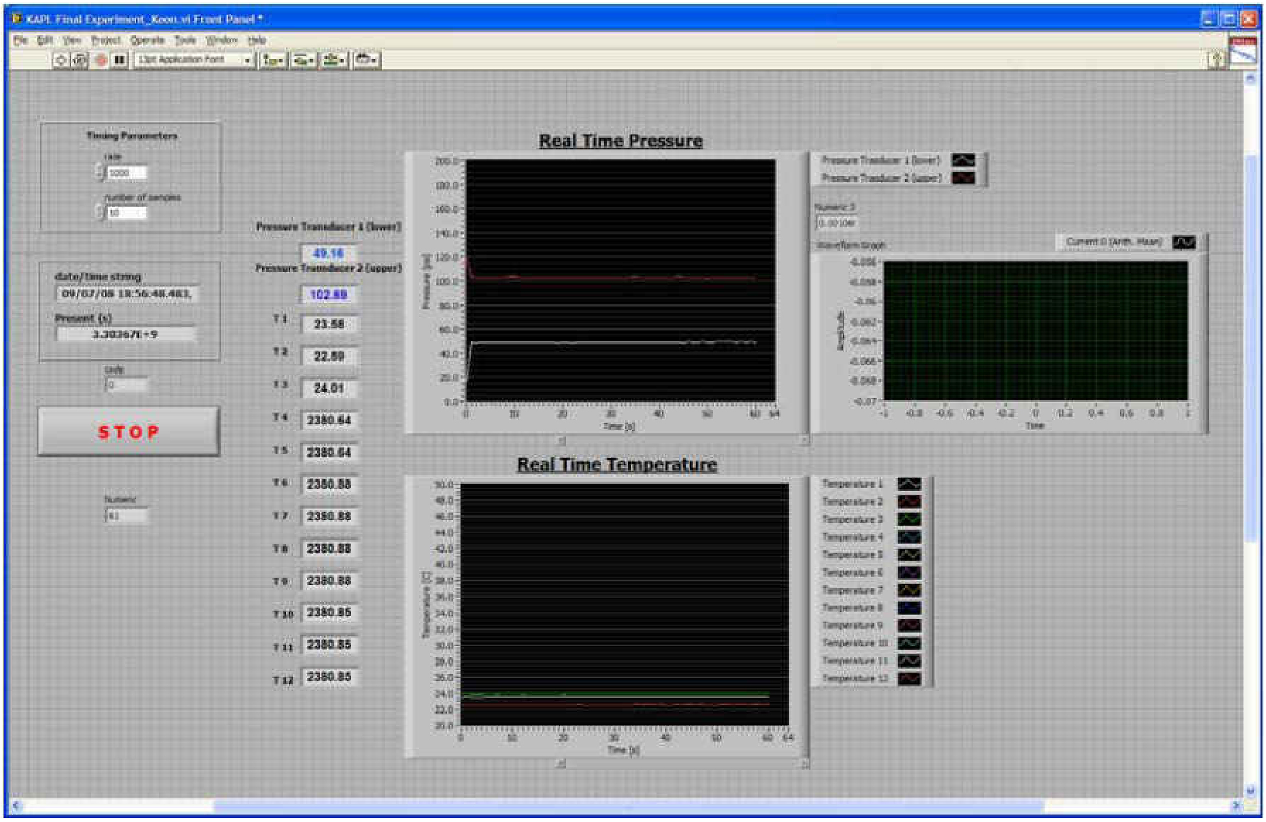

rate 1000

number of samples 10

date/time string 09/07/08 18:56:48.483,

Present (s) 3.30367E+9

code 0

Numeric 61

Pressure Transducer 1 (lower) 49.16

Pressure Transducer 2 (upper) 102.89

T 1 23.58

T 2 22.89

T 3 24.01

T 4 2380.64

T 5 2380.64

T 6 2380.88

T 7 2380.88

T 8 2380.88

T 9 2380.88

T 10 2380.85

T 11 2380.85

T 12 2380.85

Numeric 3 0.00104

Figure 20: LabVIEW interface of pressure, inlet temperature, and flow rate register

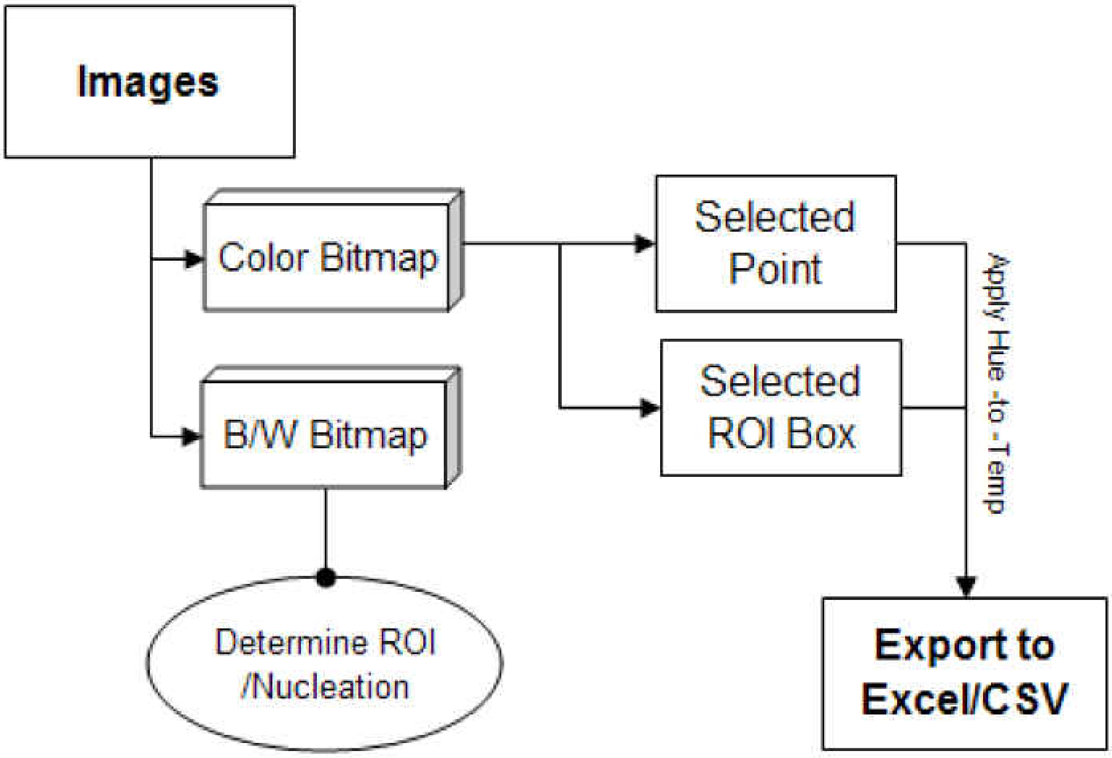

Figure 21: Image Post Processing Diagram

Image #: 0

Image Type: ● Bitmap ○ Tiff

Cursor Location: X 315, Y 1, HUE 0

TC Location: X 10, Y 10, HUE 321.8357

Calibration: 211.2+222.3*H+232.5*H^2+223.5*H3

☐ Apply Calibration

Figure 22: GUI Software Interface for TLC Image Post Processing

Defined Parameters and Calculations

The defined parameters useful for understanding the results are shown below. The operating pressure range is shown for the experiments. After defining parameters, variables can be non-dimensionalized to show trends in the results and discussion section.

Pressure Range:

$621\ kPa \cong 90\ psi$

$689\ kPa \cong 100\ psi$

$758\ kPa \cong 110\ psi$

$827\ kPa \cong 120\ psi$

$896\ kPa \cong 130\ psi$

$965\ kPa \cong 140\ psi$

$1034\ kPa \cong 150\ psi$

$Area\ (ROI) = 1 \times 10^{-4} m^2$

$q = Power = V \times I\ (W)$

$q" = \frac{q}{Area}$

$q" = heat\ flux\ (\frac{W}{m^2})$

$T_w = wall\ temperature\ (°C)$

$T_{sat} = saturation\ temperature\ (°C)$

$T_{in} = inlet\ bulk\ temperature\ (°C)$

$Inlet\ Subcooling = T_{sat} - T_{in}\ (°C)$

$Degree\ of\ Superheat = T_w - T_{sat}\ (°C)$

$D_b = bubble\ size = diameter\ of\ bubble\ (m)$

$f = bubble\ frequency = \frac{bubbles\ generated\ at\ nucleation\ site}{time}\ (Hz)$

$bubble\ velocity = \frac{vertical\ bubble\ distance}{time}\ (\frac{m}{s})$

$$R134a\ thermal\ diffusivity = \alpha = 4.82 \times 10^{-8} \left(\frac{m^2}{s}\right)$$
$$\equiv Good\ approximate\ for\ pressures\ between\ 621\ kPa\ to\ 1034\ kPa$$

$G = mass\ flux = \frac{kg}{m^2 s}$

$h_{le} = liquid\ enthalpy\ (\frac{kJ}{kg})$

$$D_o = 4.65 \times 10^{-4} \sqrt{\frac{2\sigma}{g(\rho_l - \rho_v)}} Ja^{*\frac{5}{4}}\ (m)$$

$$Ja^* = \frac{\rho_l C_{p_l} T_{sat}}{\rho_v h_{lv}}$$

$\frac{D}{D_o} = Dimensionless\ Bubble\ Deparature\ Ratio$

$\sigma = surface\ tension\ (\frac{N}{m})$

$g = 9.8 \frac{m}{s^2}$

$\rho_l = liquid\ density\ (\frac{kg}{m^3})$

$\rho_v = vapor\ density\ (\frac{kg}{m^3})$

$C_{P_l} = liquid\ specific\ heat\ (\frac{kJ}{kgK})$

$h_{lv} = liquid - vapor\ enthalpy\ (\frac{kJ}{kg})$

$Bo = Boiling\ Number = \frac{q"}{h_{le} G}$

$N_f = Dimensionless\ Bubble\ Generation\ Frequency = \frac{f {D_b}^2}{\alpha}$

CHAPTER FOUR: RESULTS AND DISCUSSION

Experiments on subcooled flow boiling heat transfer have been conducted with refrigerant R-134a under a mass flux (G) of 484.838 kg/m^{2}s. With this particular flow velocity, the wall heat flux ranged from 167.2 kW/m^2 to 672.1 kW/m^2, the inlet subcooling ranged from 0.3538 °C to 16.5553 °C, the system pressure ranged from 621 kPa to 1034 kPa (90 to 150 psi). All experiments are heat flux dependent whereby other parameters such as mass flux and system pressure are held constant. There will also be a comparison between data at a particular pressure for mass fluxes of 484.838 kg/m^{2}s and 1212.1 kg/m^{2}s. The trends for the flow velocity of 1212.1 kg/m^{2}s can be illustrated in more depth in Appendix F.

In order to properly determine where bubbles are generated, it is important to define the critical crack size (notch). The critical crack size is defined as the location where enough superheat is present to make a surface imperfection (heater) active. The critical crack size, r_c, is defined below.

$$r_c = \frac{2\sigma T_{sat} v_{lv}}{h_{lv} R}$$

$\sigma = surface\ tension\ (\frac{N}{m})$

$T_{sat} = saturation\ temperature\ (C)$

$v_{lv} = liquid - vapor\ specific\ volume\ (\frac{m^3}{kg})$

$h_{lv} = liquid - vapor\ enthalpy\ (\frac{J}{kg})$

$R = R134a\ gas\ constant$

$d_c = 2r_c$

Plugging in R134a values:

$d_c \geq \approx 0.2\mu m$

Since, d_c is approximately 0.2μm; this crack (notch) site will have enough superheat to generate bubbles. It should also be noted that the researchers are not able to see the notch site due to camera limitations. Therefore, when researchers are performing data analysis, the first bubble realized is not the nucleation site (notch location), but actually the first initial bubble captured due to the limitations in resolution and acquisition times from cameras used.

For the set of analysis on mass flux of 484.838 kg/m^2s, the data is presented in non-dimensional form to show the trends; this manner of data presentation is performed similarly within literature. As can be seen by the upcoming figures, the dimensional data will also be shown alongside the non-dimensional data to show the correspondence.

Effect of non-dimensional heat flux on degree of superheat:

An increase in the heat flux will lead to an increase in the degree of superheat. By examining the experimental data in figures 23-36 below, the degree of superheat does not increase monotonically with the increase in heat flux. Based on current literature knowledge, there are no studies showing the oscillations in superheat after increasing the heat flux. A possible explanation for these superheat plots differentiating from literature trends would be due to the isolated nucleation sites that formed. Highlighting this last point, Kenning and Yan in 1995 concluded from their study that a particular nucleation site has its own specific nucleation superheat [33]. Therefore, the oscillations in superheat may be attributed to several factors at the local nucleation site leading to different wall temperatures. With an increase in heat flux, the selection of the local nucleation site typically changes to account for the occasional collision and coalescence of bubbles.

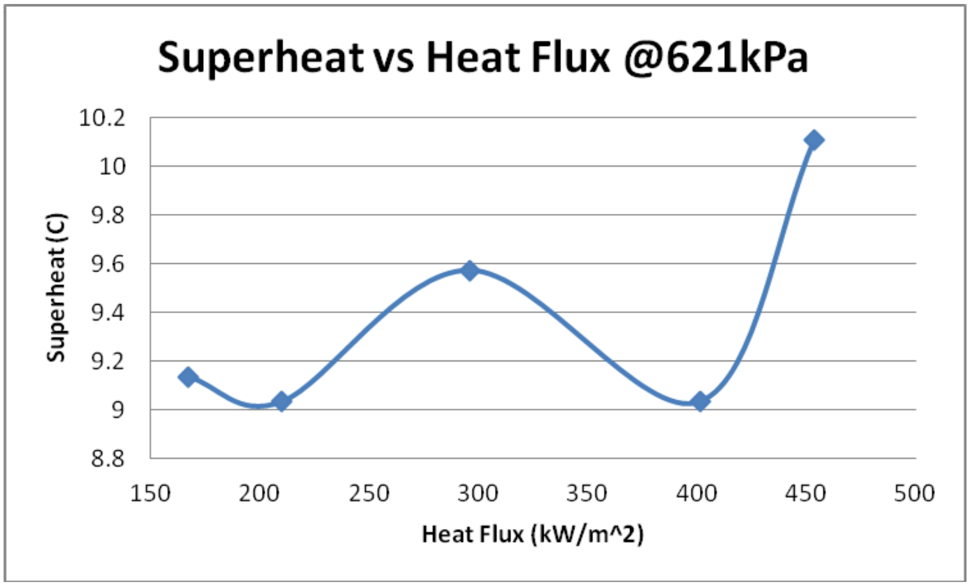

Figure 23: Superheat vs. Heat Flux @ 621 kPa

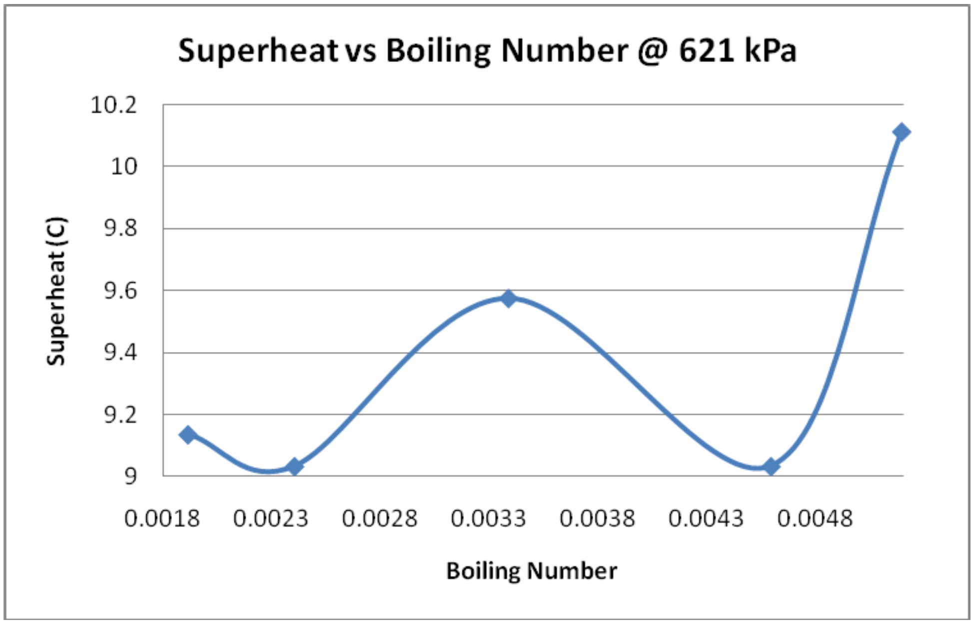

Figure 24: Superheat vs. Boiling Number @ 621 kPa

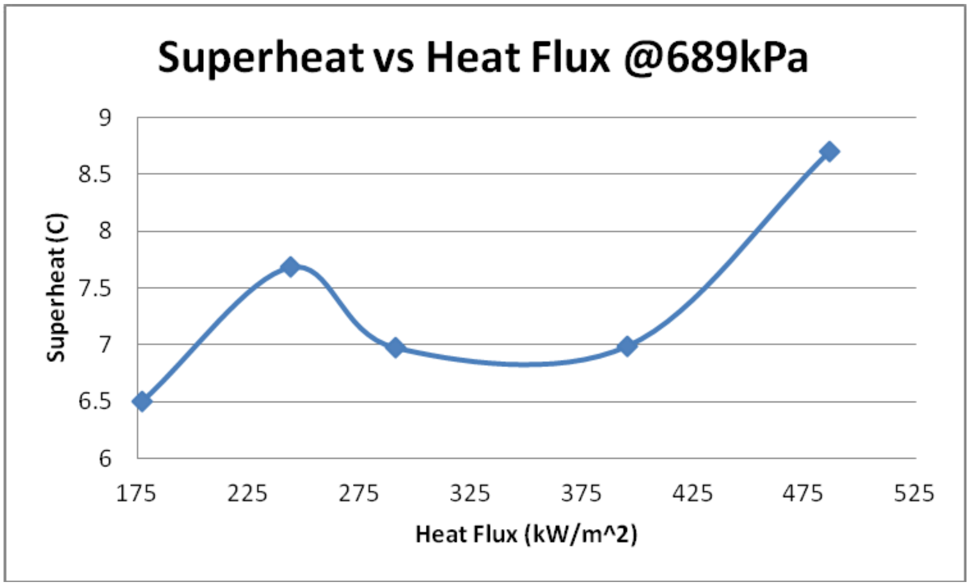

Figure 25: Superheat vs. Heat Flux @ 689 kPa

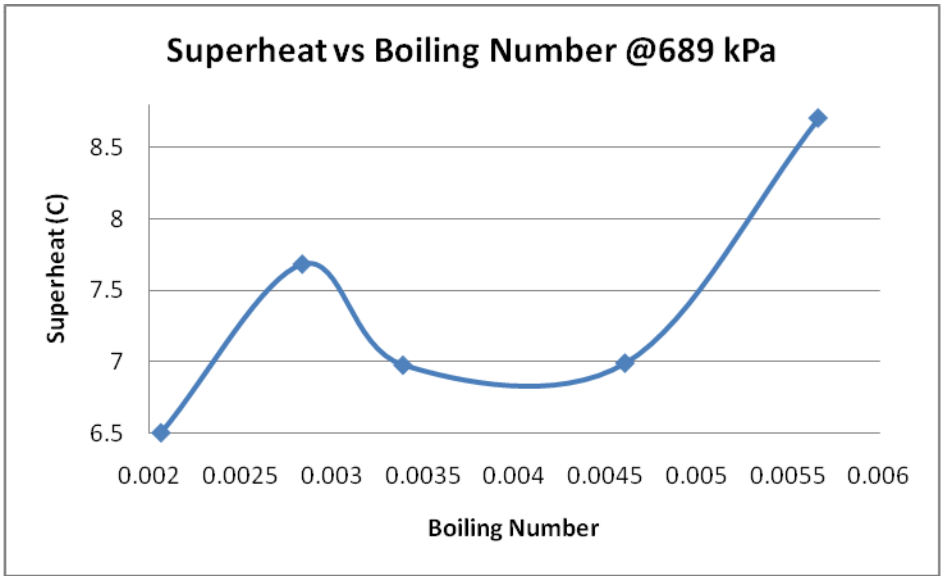

Figure 26: Superheat vs. Boiling Number @ 689 kPa

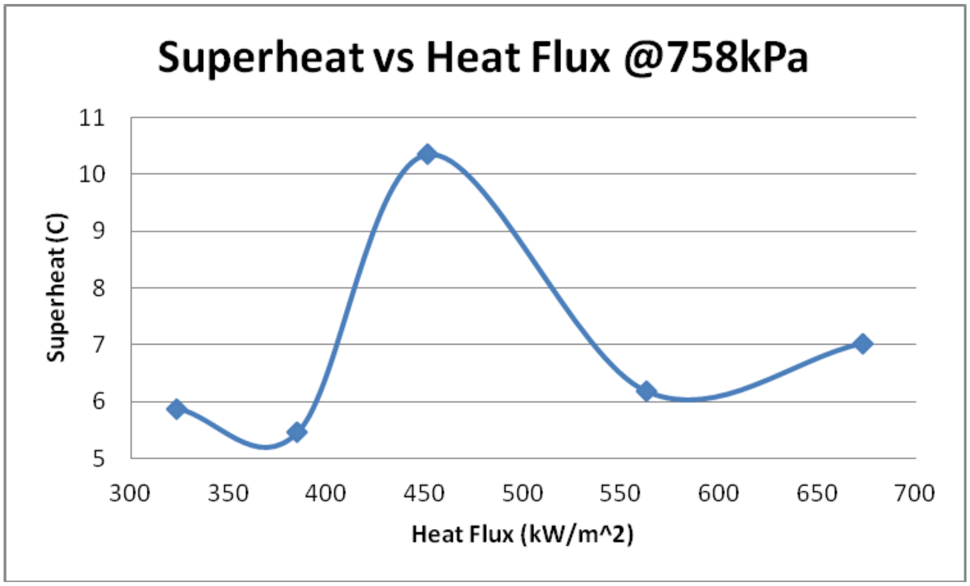

Figure 27: Superheat vs. Heat Flux @758kPa

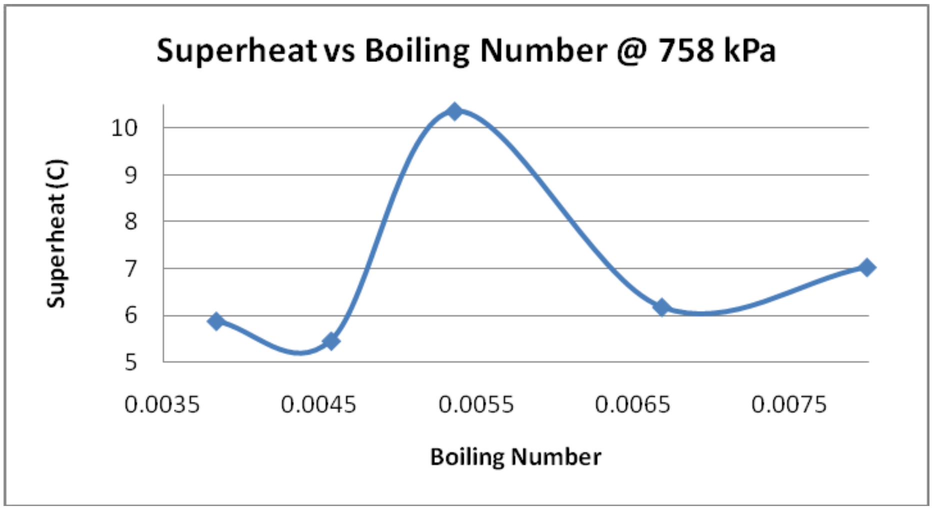

Figure 28: Superheat vs. Boiling Number @ 758 kPa

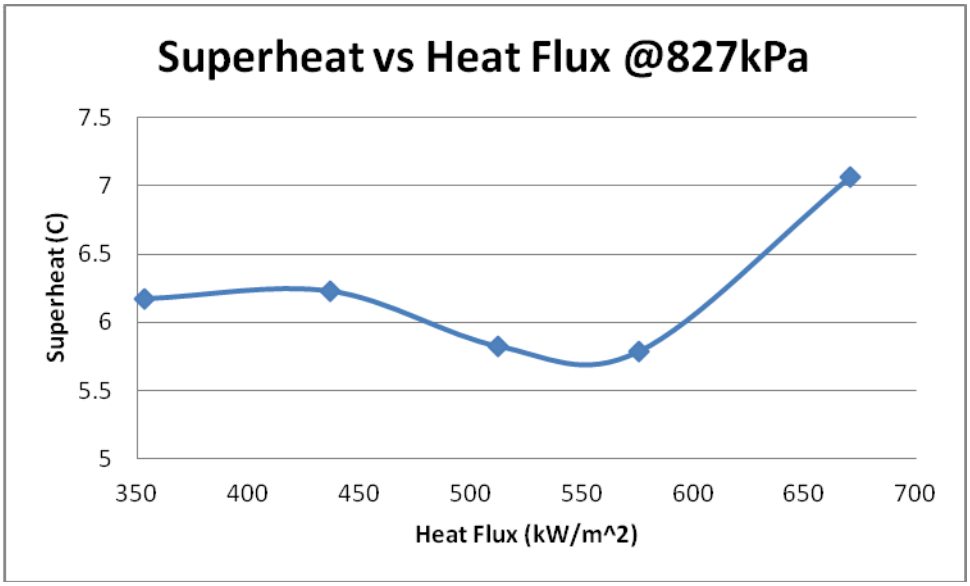

Figure 29: Superheat vs. Heat Flux @ 827kPa

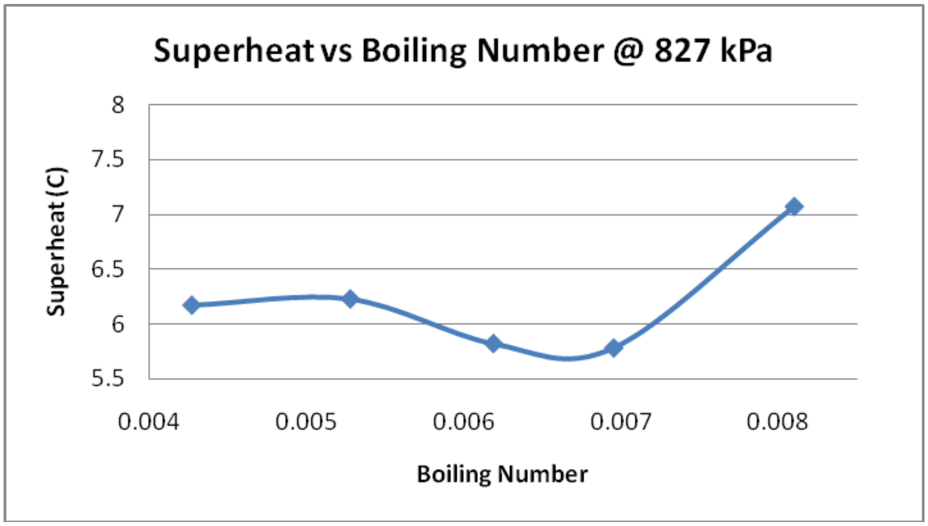

Figure 30: Superheat vs. Boiling Number @ 827kPa

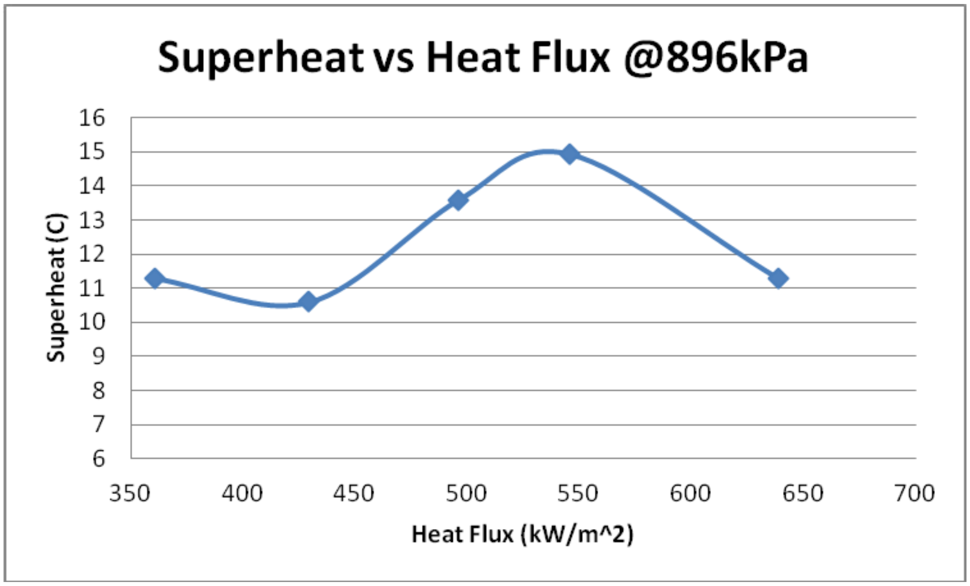

Figure 31: Superheat vs. Heat Flux @ 896kPa

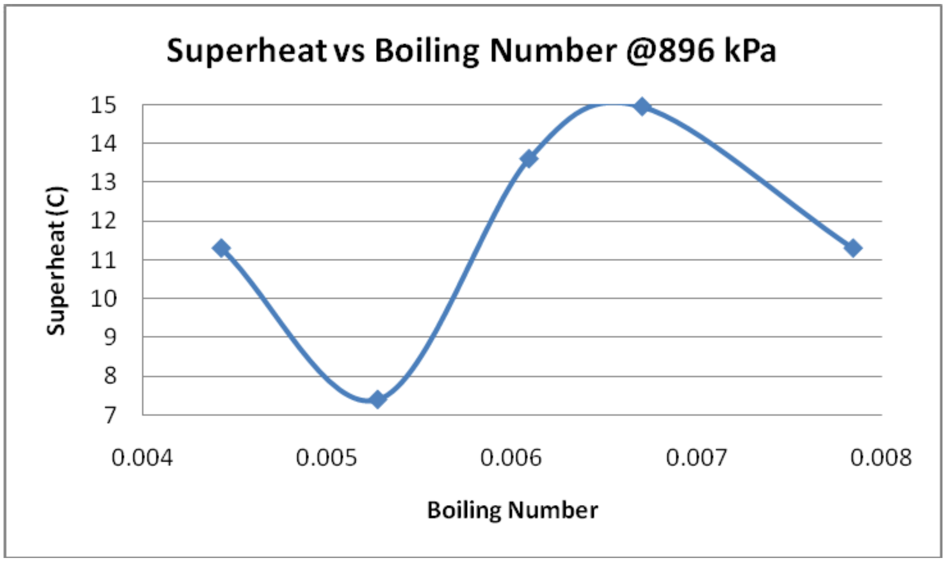

Figure 32: Superheat vs. Boiling Number @ 896kPa

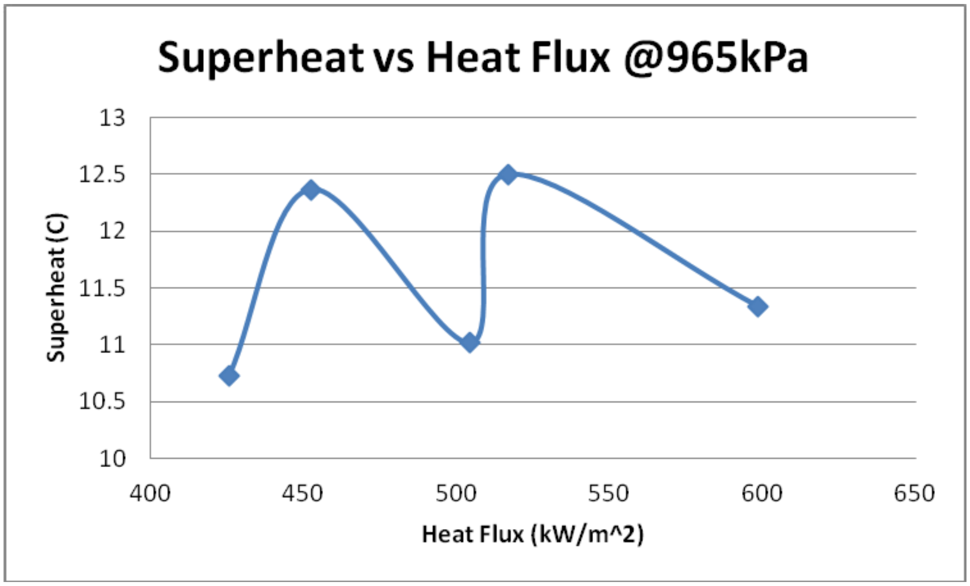

Figure 33: Superheat vs. Heat Flux @ 965kPa

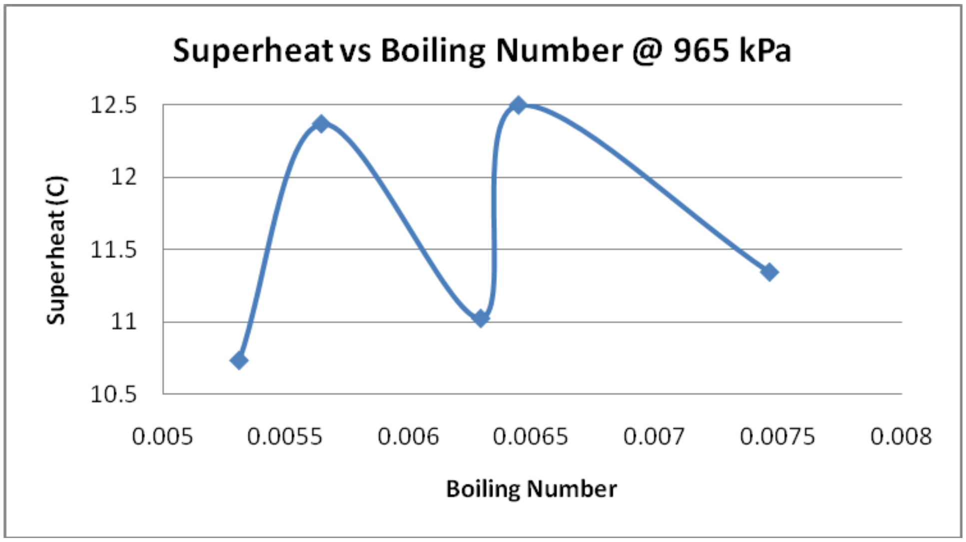

Figure 34: Superheat vs. Boiling Number @ 965kPa

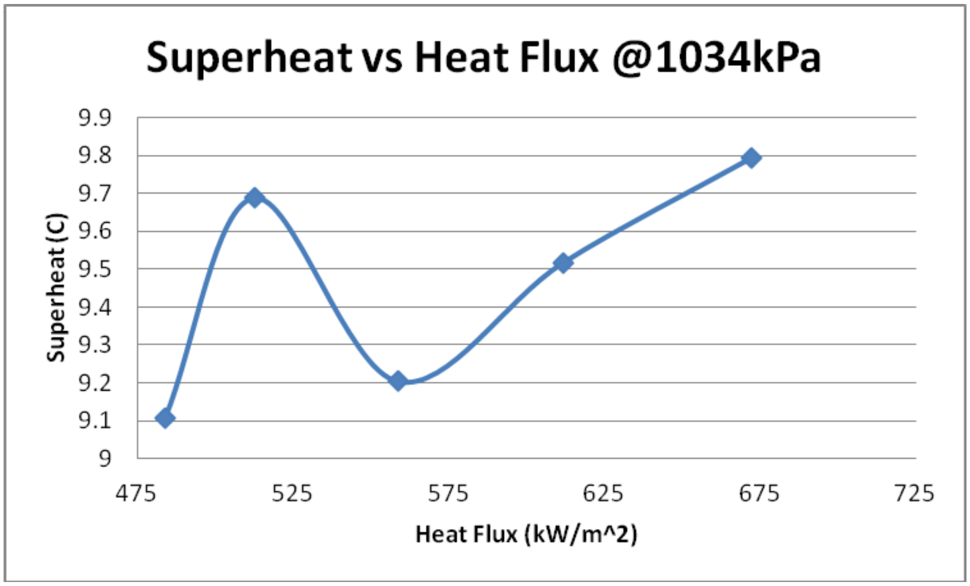

Figure 35: Superheat vs. Heat Flux @ 1034kPa

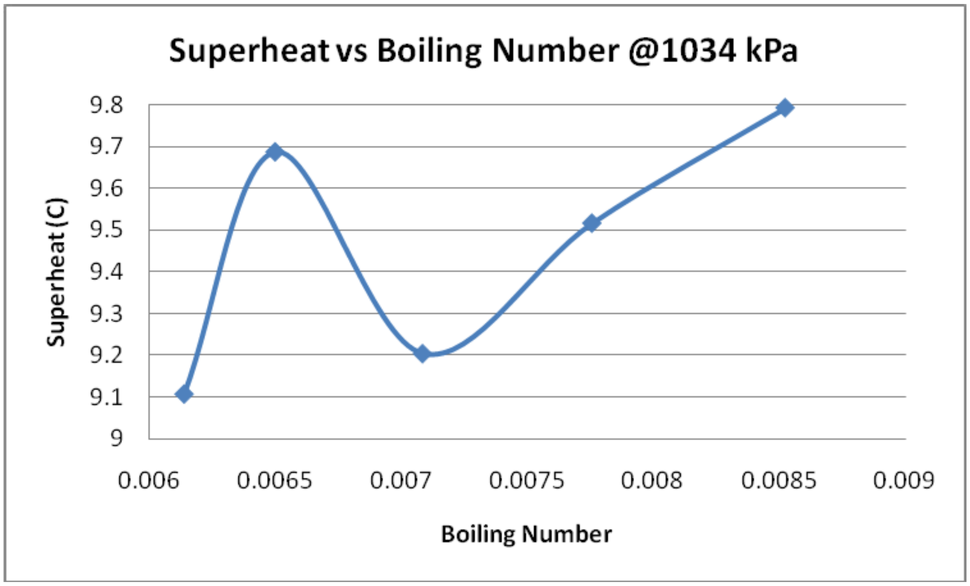

Figure 36: Superheat vs. Boiling Number @ 1034kPa

Effect of non-dimensional heat flux on dimensionless bubble size:

The departure bubble size can be classified as the first signs of displacement from the nucleation site. By evaluating some literature, the behavior of the departure bubble size can be better predicted. Based on the work using water by Kandlikar in 1992, the primary mechanism by bubble release at low mass flux is due to shear forces [28]. Zeng et al in 1993 postulated that in upflow boiling the shear forces keep the bubble along the wall, preventing lift off of the bubbles. Similarly, Thorncroft et al in 1998 conducted an upflow experiment using refrigerant FC-87 whereby bubbles departing the nucleation site typically slide along the heater wall instead of lifting off [55]. Thorncroft et al in 1998 and Callizo et al in 2010 predicted that bubbles within bubbly flow will be spherical in shape [40, 55]. Fu et al in 2010 performed an experiment using liquid nitrogen whereby the bubble departure diameter increased with an increase in heat flux [16]. In order to obtain the non-dimensional bubble size, the Cole and Rohsenow (1969) correlation for determining the departure bubble size is used [13].

The correlation is useful in defining the theoretical bubble departure diameters and comparing them with the experimental bubble departure diameters. If the bubble departure correlation is approximately one, then the experimental bubble departure diameter matches well with the theoretical bubble departure diameter. If the correlation is below or above, then the experimental bubble departure diameter under-predicted or over-predicted the theoretical bubble departure diameter. Assessing the data in figures 37-38, the data does not follow the trend of an increasing departure bubble size with an increase in heat flux. An explanation for figures 37-38 differentiating from trends is a water study performed by Kandlikar et al in 1996 whereby they postulated that an increase in wall superheat causes a decrease in the departure bubble size. The researchers also noted that a very low inlet subcooling can also lead to a reduction in departure bubble size [29]. By coupling the wall superheat and low inlet subcooling, this could explain why figures 37-38 exhibit the opposite trend of literature. In figures 39-50, the data is now representative of trends in literature. For each case, as the heat flux increases the bubble departure size also increases. Moreover, it can be seen that the bubble departure size increased by more than a factor of two when going from the lowest pressure readings to the highest pressure readings for a particular range of heat fluxes. It can be seen similarly for the non-dimensional quantities. In figures 38 and 40, the experimental bubble departure sizes under-predict the correlation. In figures 42, 44, and 46, the experimental bubble departure sizes approximately predict the correlation well. In figures 48 and 50, the experimental bubble departure sizes over-predict the correlation well. Other correlations should be used to obtain better matches between the theoretical and experimental bubble departure sizes.

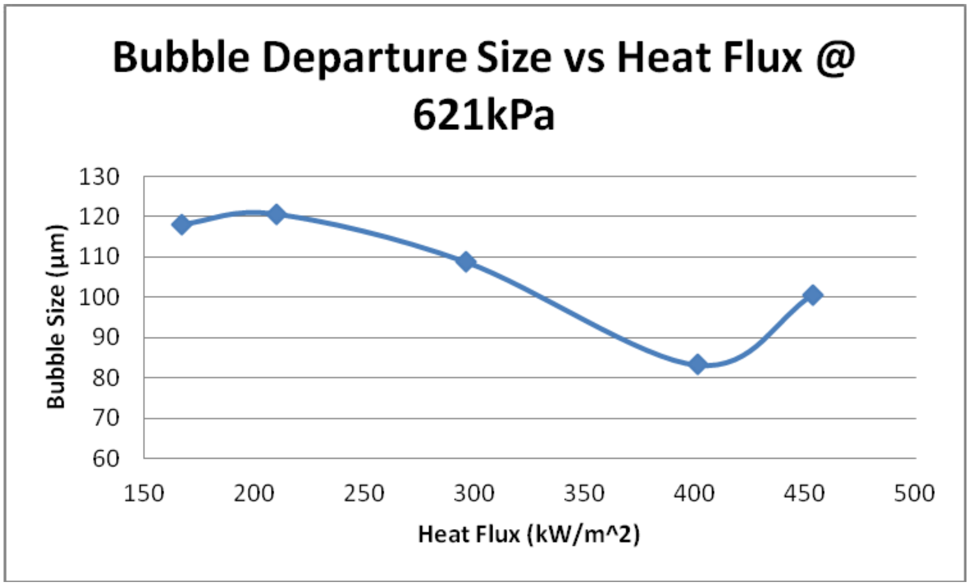

Figure 37: Bubble Departure Size vs. Heat Flux @621 kPa

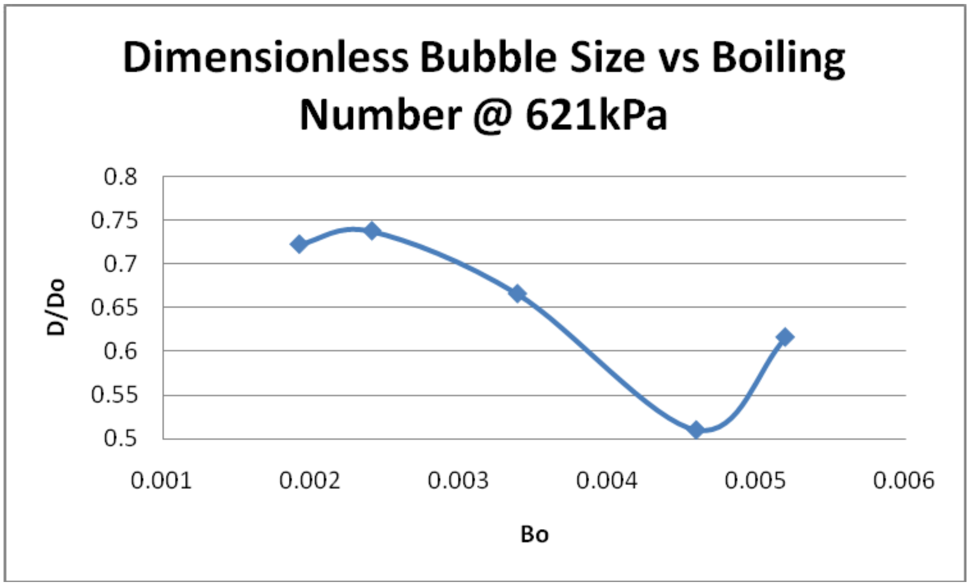

Figure 38: Dimensionless Bubble Departure Ratio (D/Do) vs. Bo @ 621kPa

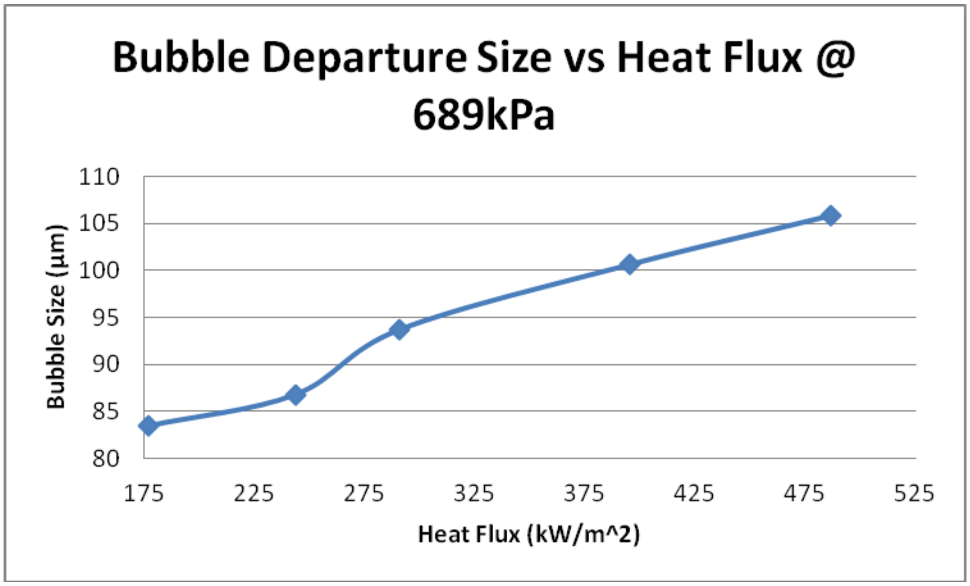

Figure 39: Bubble Departure Size vs. Heat Flux @689 kPa

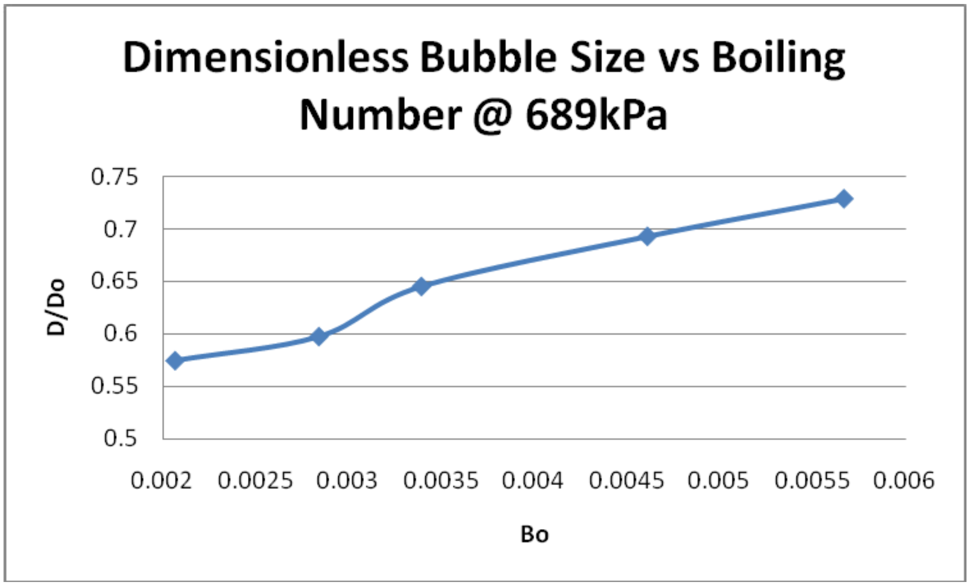

Figure 40: Dimensionless Bubble Departure Ratio (D/Do) vs. Bo @ 689kPa

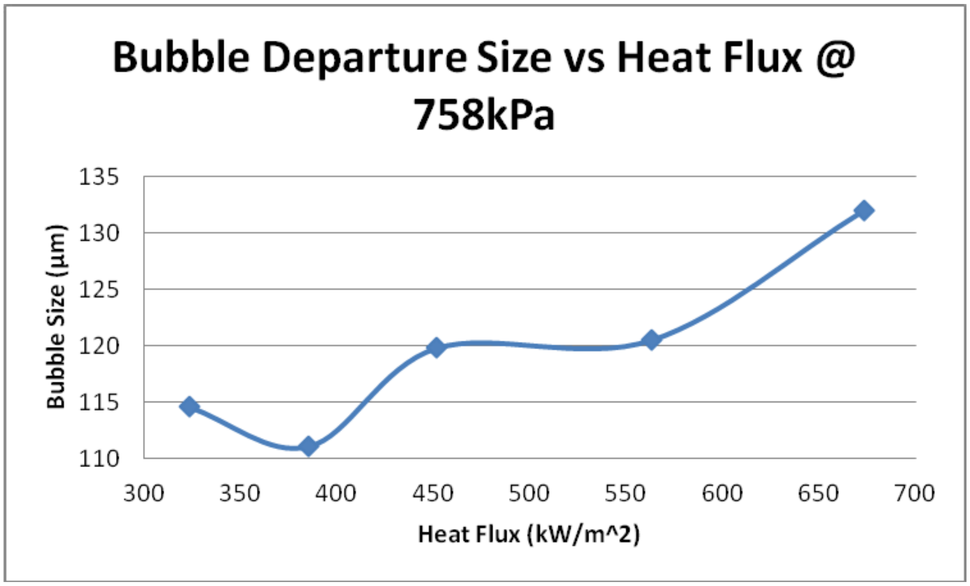

Figure 41: Bubble Departure Size vs. Heat Flux @758 kPa

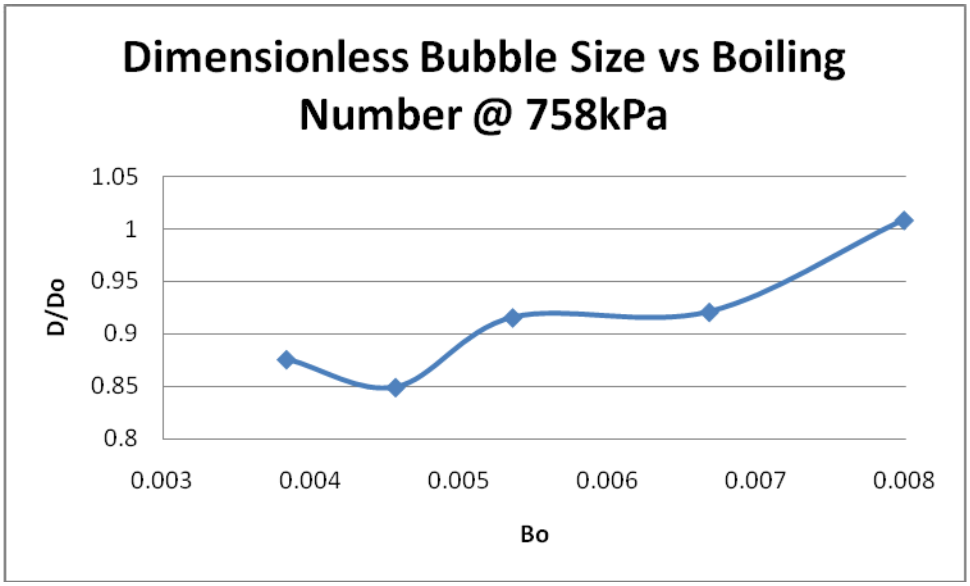

Figure 42: Dimensionless Bubble Departure Ratio (D/Do) vs. Bo @ 758kPa

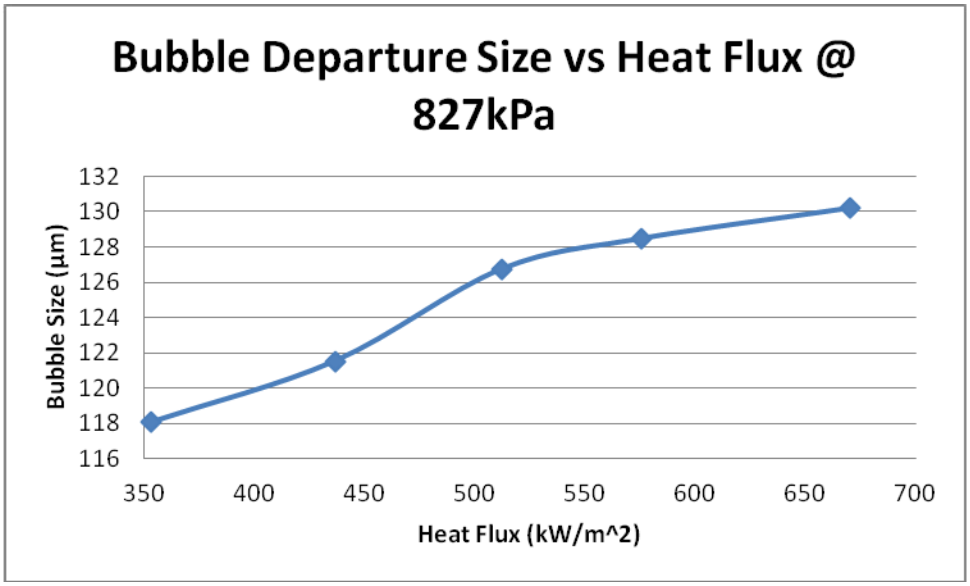

Figure 43: Bubble Departure Size vs. Heat Flux @827 kPa

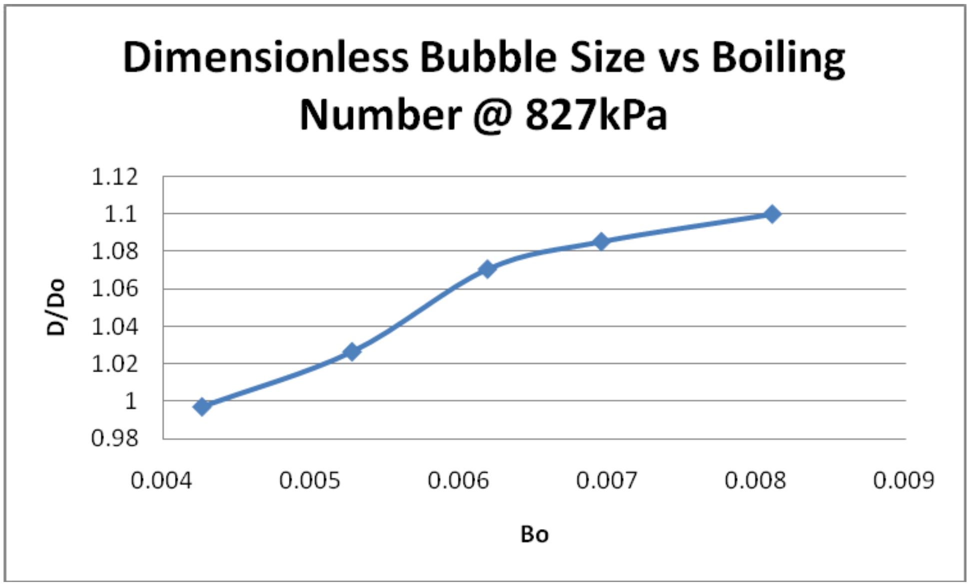

Figure 44: Dimensionless Bubble Departure Ratio (D/Do) vs. Bo @ 827kPa

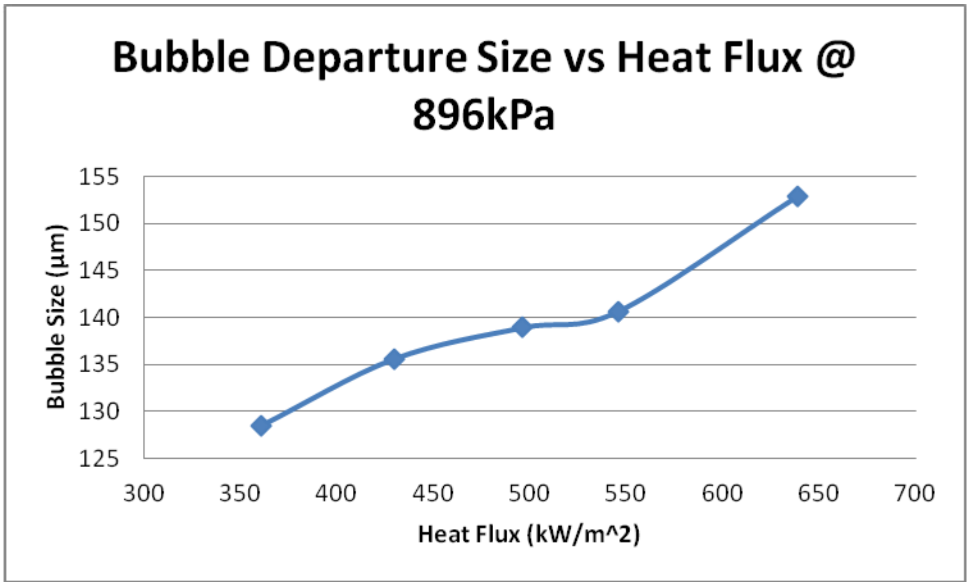

Figure 45: Bubble Departure Size vs. Heat Flux @896 kPa

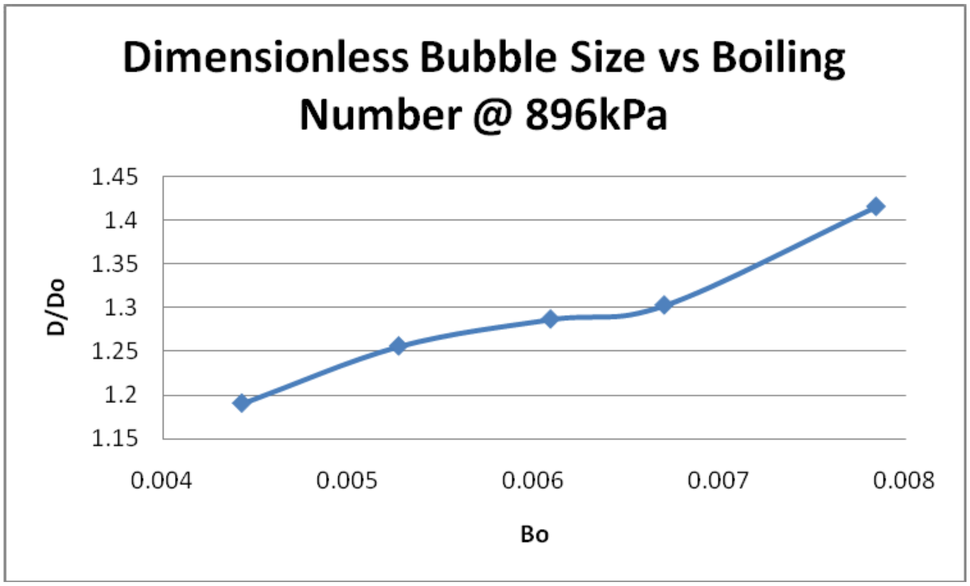

Figure 46: Dimensionless Bubble Departure Ratio (D/Do) vs. Bo @ 896kPa

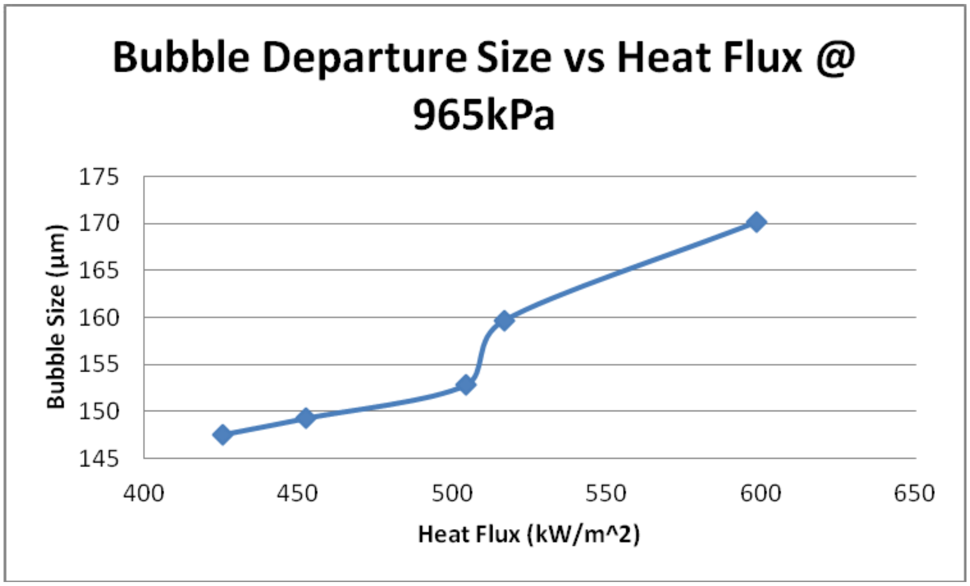

Figure 47: Bubble Departure Size vs. Heat Flux @965 kPa

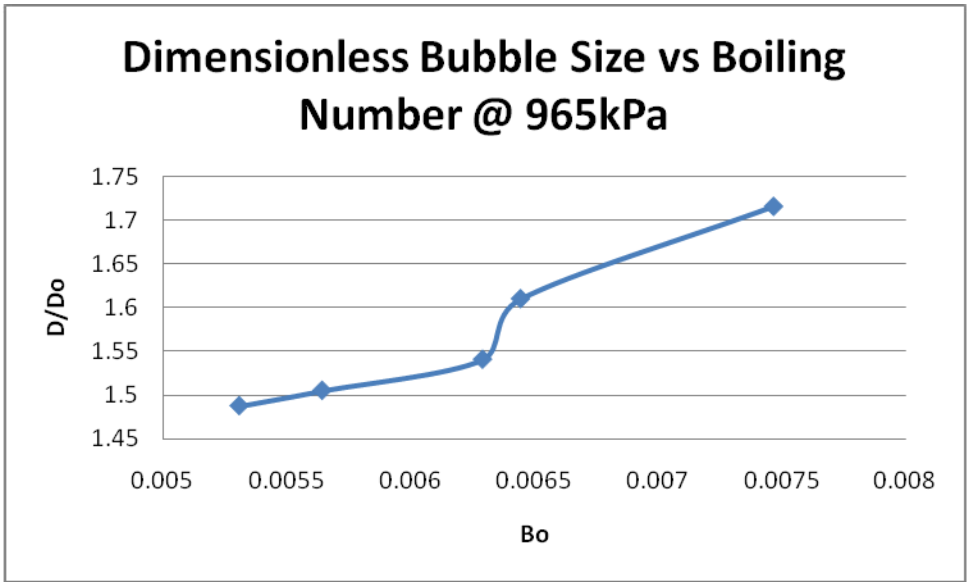

Figure 48: Dimensionless Bubble Departure Ratio (D/Do) vs. Bo @ 965kPa

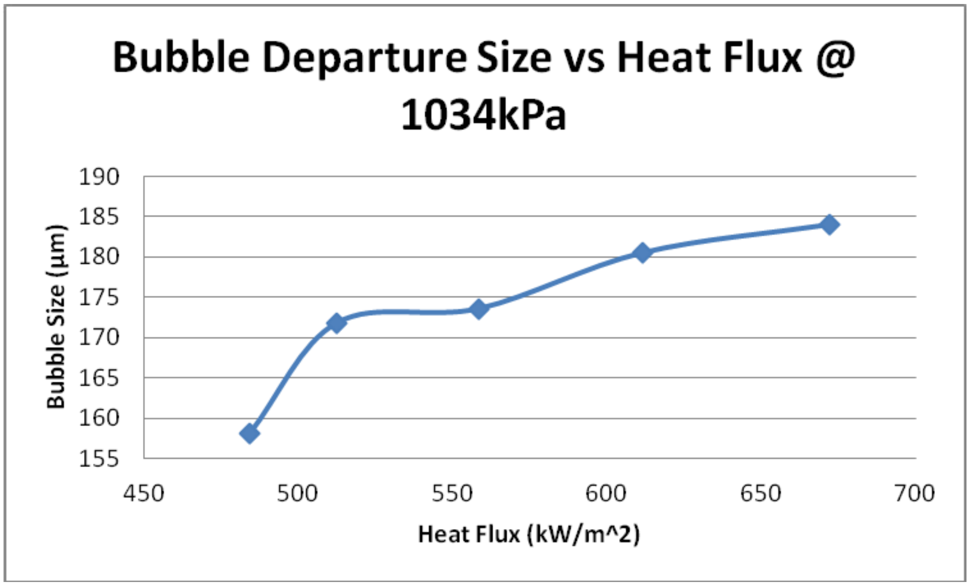

Figure 49: Bubble Departure Size vs. Heat Flux @1034 kPa

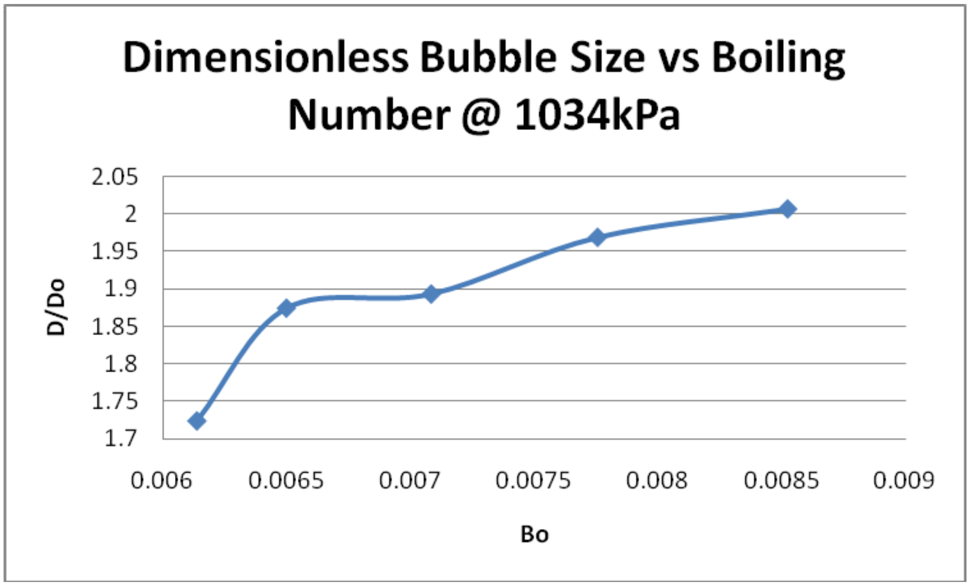

Figure 50: Dimensionless Bubble Departure Ratio (D/Do) vs. Bo @ 1034kPa

Effect of non-dimensional heat flux (Bo) on non-dimensional bubble frequency (N_f):

In Table 1, the impact of heat flux on bubble frequency at different pressures is outlined. From the table, the bubble frequency increases with an increase in heat flux. At any given pressure, the bubble frequency always increases with an increase in heat flux. With an increase in pressure, the bubble frequency typically increases with increase in heat flux. The first few pressures 621 kPa to 689 kPa do not always follow the trend. At a pressure of 758 kPa, the bubble frequency is shown to increase with an increase in pressure. For instance, the bubble frequency increased by 47Hz when the pressure increased from 758 kPa to 827 kPa at approximately a heat flux of 670 kW/m^2. It also has to be noted that since bubble generation is not always at the same nucleation site the rate of growth would be different for newly activated sites.

Table 1: Frequency dependence on Heat Flux

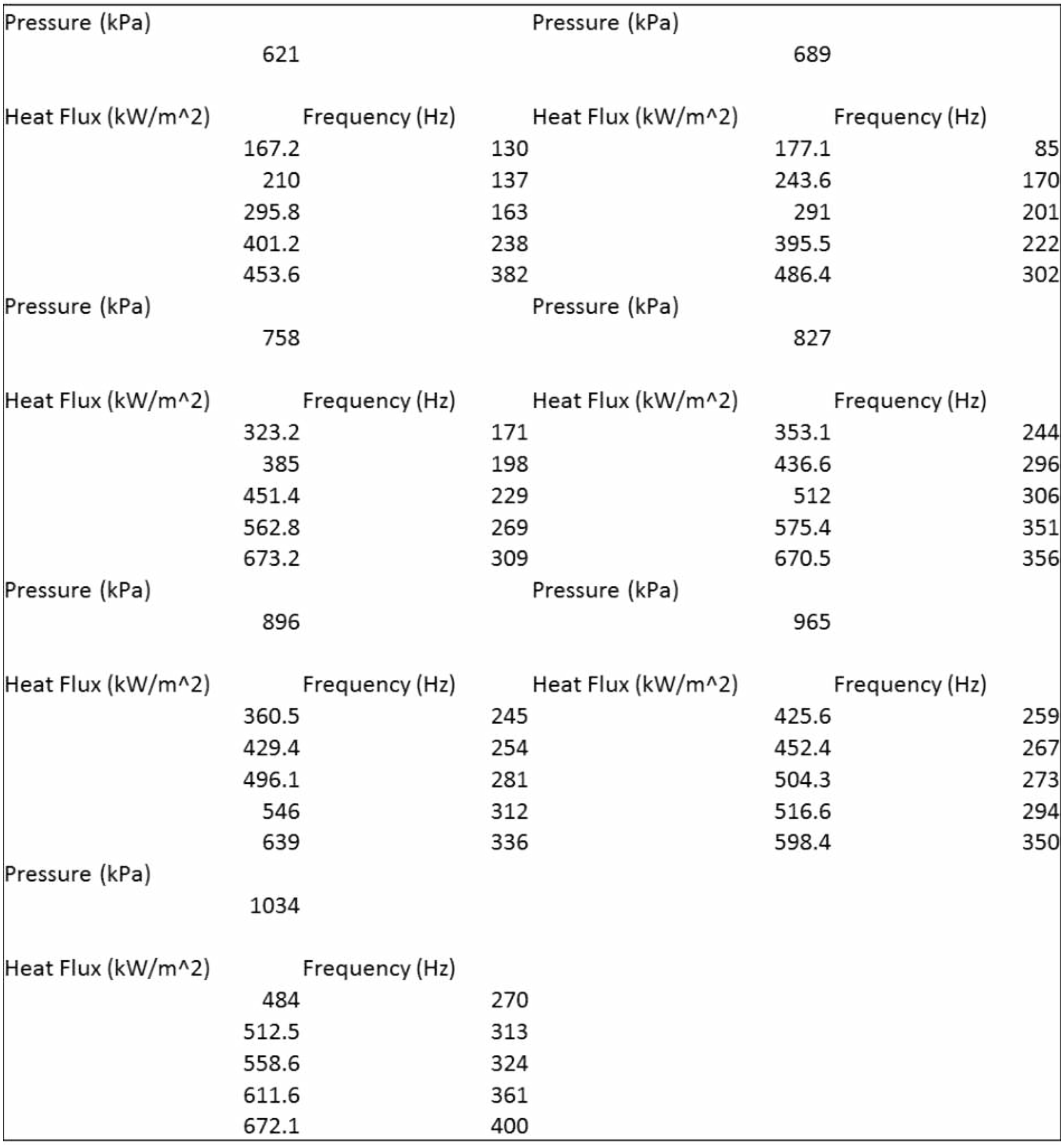

Pressure (kPa)		Pressure (kPa)	
621		689	
Heat Flux (kW/m^2)	Frequency (Hz)	Heat Flux (kW/m^2)	Frequency (Hz)
167.2	130	177.1	85
210	137	243.6	170
295.8	163	291	201
401.2	238	395.5	222
453.6	382	486.4	302
Pressure (kPa)		Pressure (kPa)	
758		827	
Heat Flux (kW/m^2)	Frequency (Hz)	Heat Flux (kW/m^2)	Frequency (Hz)
323.2	171	353.1	244
385	198	436.6	296
451.4	229	512	306
562.8	269	575.4	351
673.2	309	670.5	356
Pressure (kPa)		Pressure (kPa)	
896		965	
Heat Flux (kW/m^2)	Frequency (Hz)	Heat Flux (kW/m^2)	Frequency (Hz)
360.5	245	425.6	259
429.4	254	452.4	267
496.1	281	504.3	273
546	312	516.6	294
639	336	598.4	350
Pressure (kPa)			
1034			
Heat Flux (kW/m^2)	Frequency (Hz)		
484	270		
512.5	313		
558.6	324		
611.6	361		
672.1	400		

The following figures below will outline the effect of heat flux on the frequency of bubble generation. The dimensional data is shown in correspondence with the non-dimensional variables to show the trends. In figures 51, the dimensional bubble frequency is not increasing linearly with respect to the increase in the heat flux. From the first heat flux value to the heat flux value, the bubble frequency is still shown to increase at a pressure of 621 kPa. In figures 53-64, a linear profile is exhibited for the bubble frequency as the heat flux increases. Based on these figures, it is clear that as the pressure increases, the bubble frequency begins at a higher value than at the lower pressure. Therefore, there are more activity sites and faster growth rates at higher pressures based on the trends. Similar trends are visualized for the corresponding non-dimensional variables.

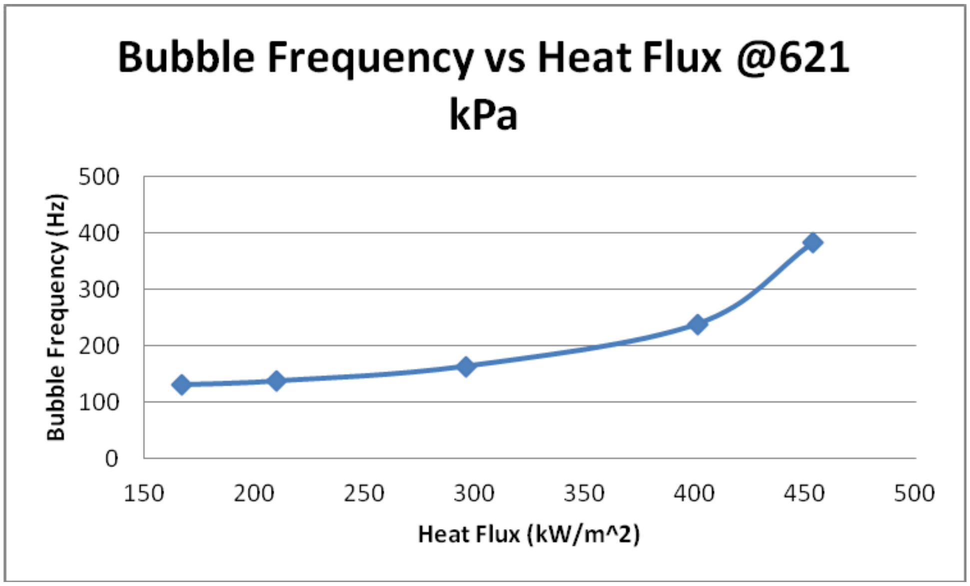

Figure 51: Bubble Frequency vs. Heat Flux at P=621 kPa

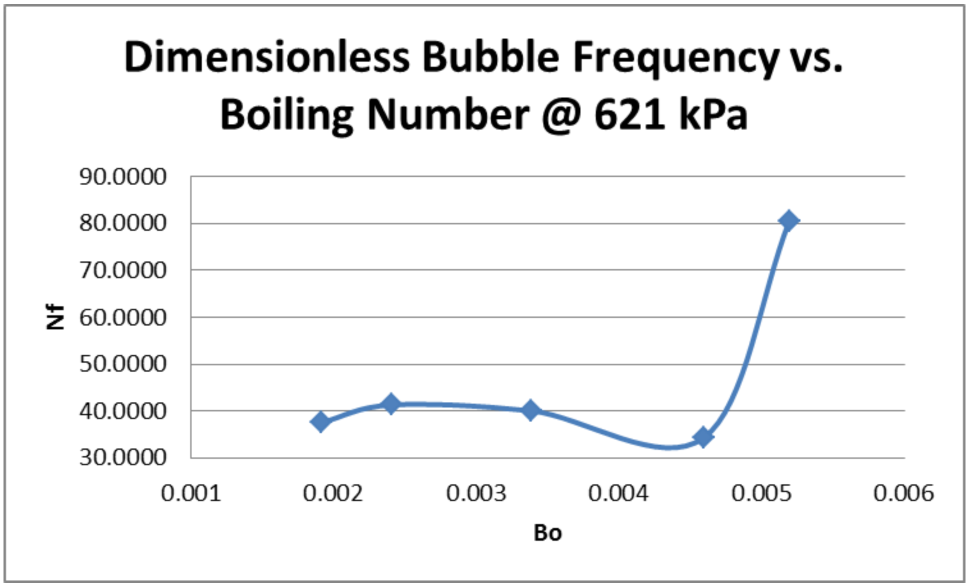

Figure 52: Dimensionless Bubble Generation Frequency vs. Boiling Number at P=621 kPa

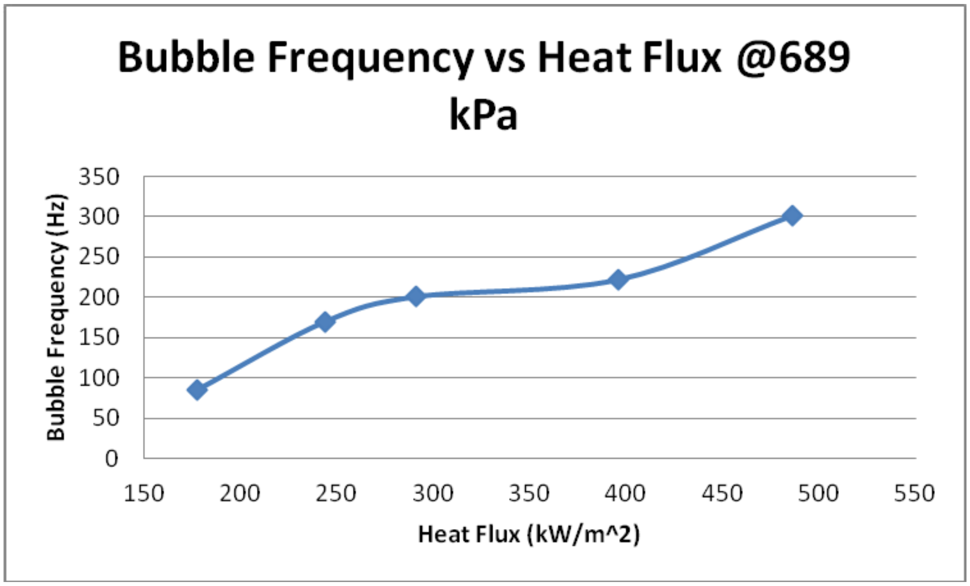

Figure 53: Bubble Frequency vs. Heat Flux at P=689 kPa

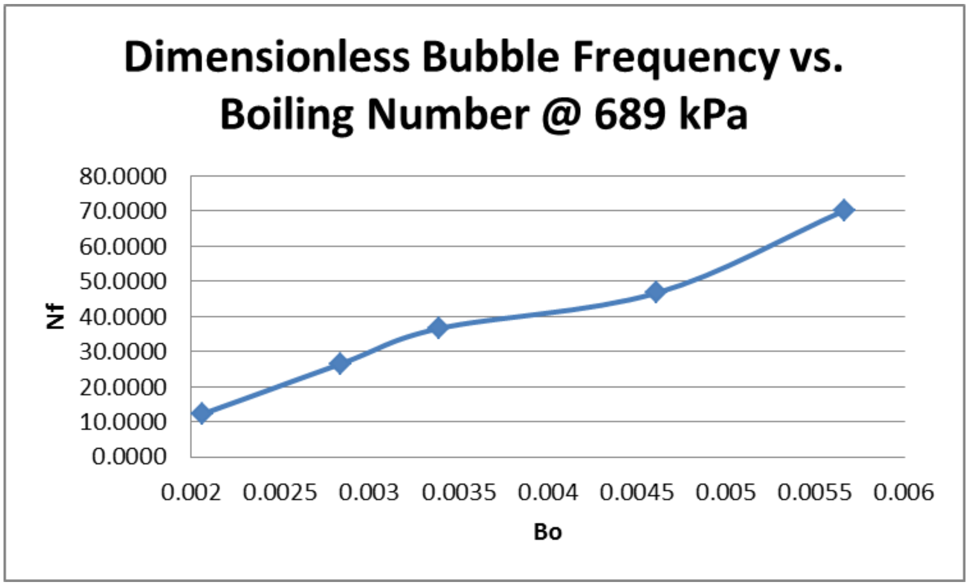

Figure 54: Dimensionless Bubble Generation Frequency vs. Boiling Number at P=689 kPa

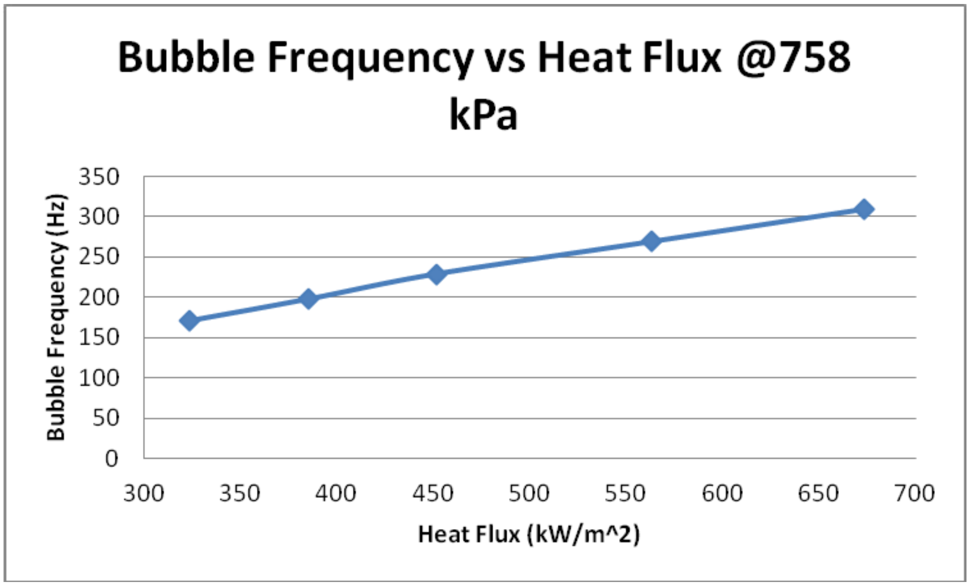

Figure 55: Bubble Frequency vs. Heat Flux at P=758 kPa

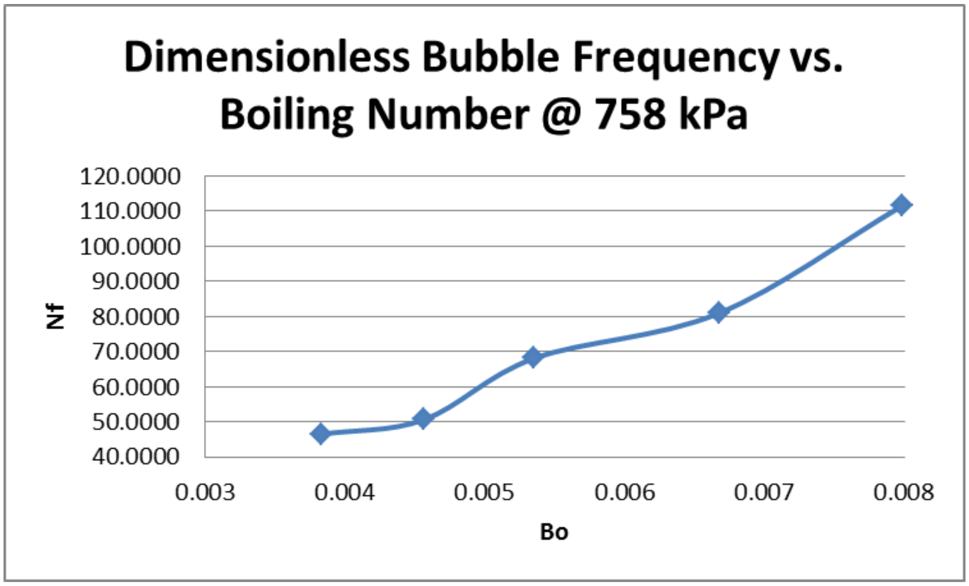

Figure 56: Dimensionless Bubble Generation Frequency vs. Boiling Number at P=758 kPa

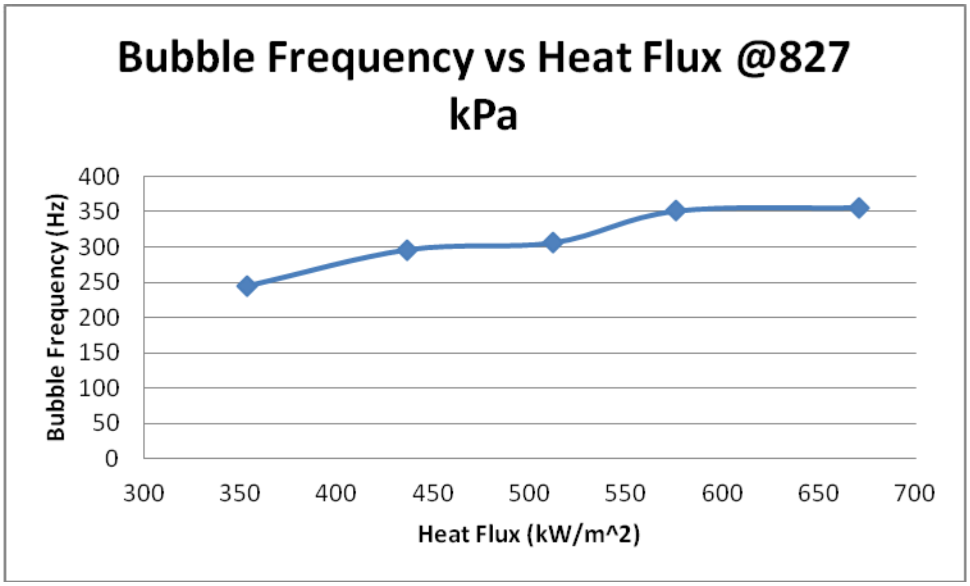

Figure 57: Bubble Frequency vs. Heat Flux at P=827 kPa

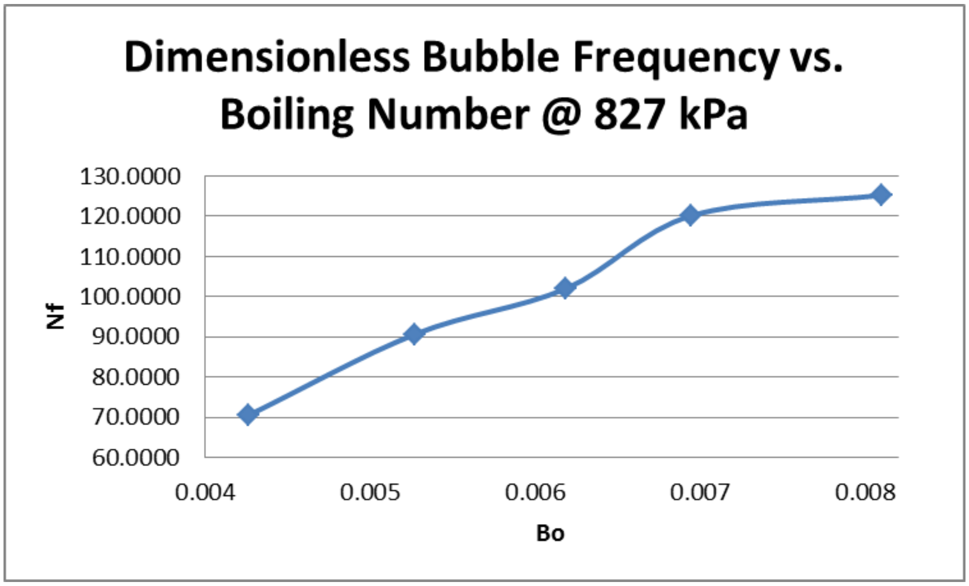

Figure 58: Dimensionless Bubble Generation Frequency vs. Boiling Number at P=827 kPa

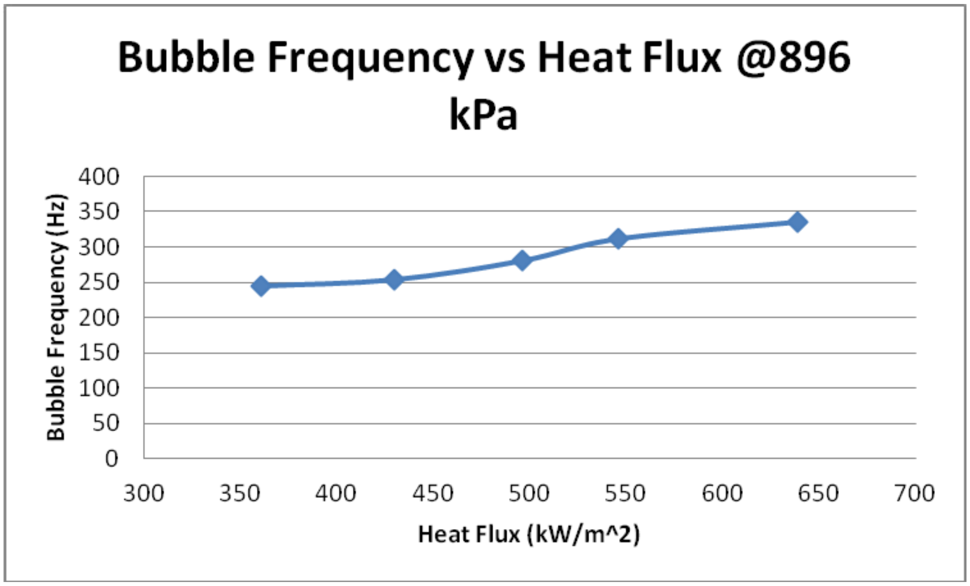

Figure 59: Bubble Frequency vs. Heat Flux at P=896 kPa

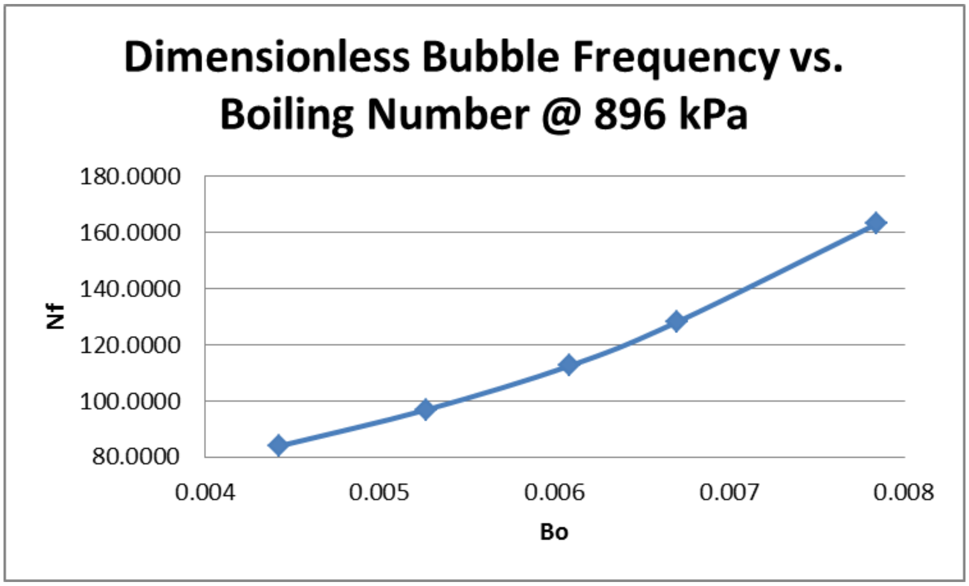

Figure 60: Dimensionless Bubble Generation Frequency vs. Boiling Number at P=896 kPa

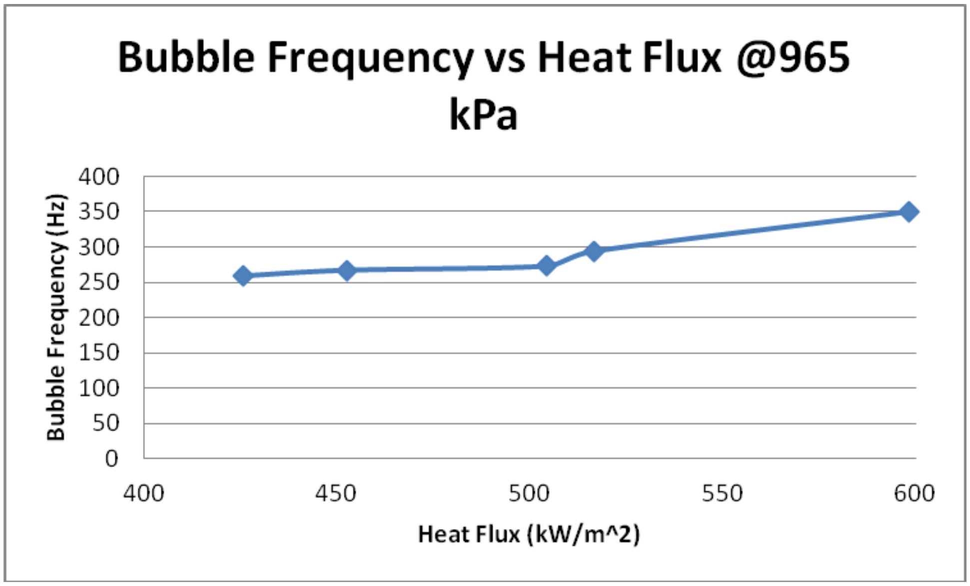

Figure 61: Bubble Frequency vs. Heat Flux at P=965 kPa

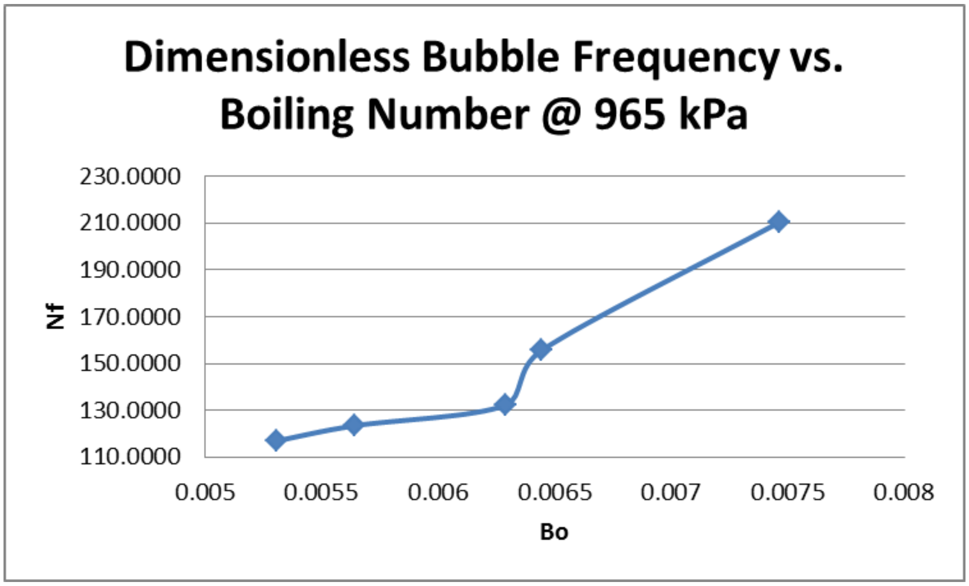

Figure 62: Dimensionless Bubble Generation Frequency vs. Boiling Number at P=965 kPa

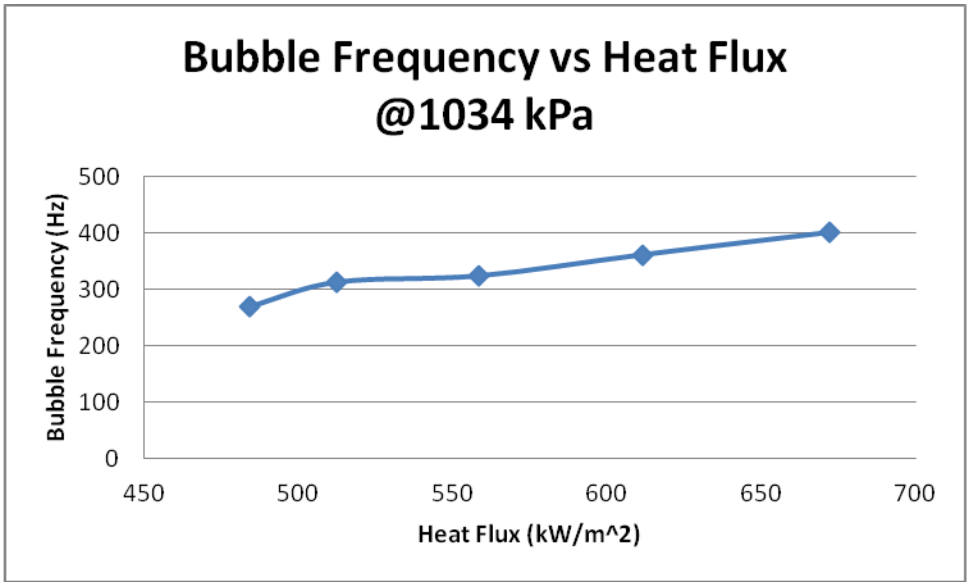

Figure 63: Bubble Frequency vs. Heat Flux at P=1034 kPa

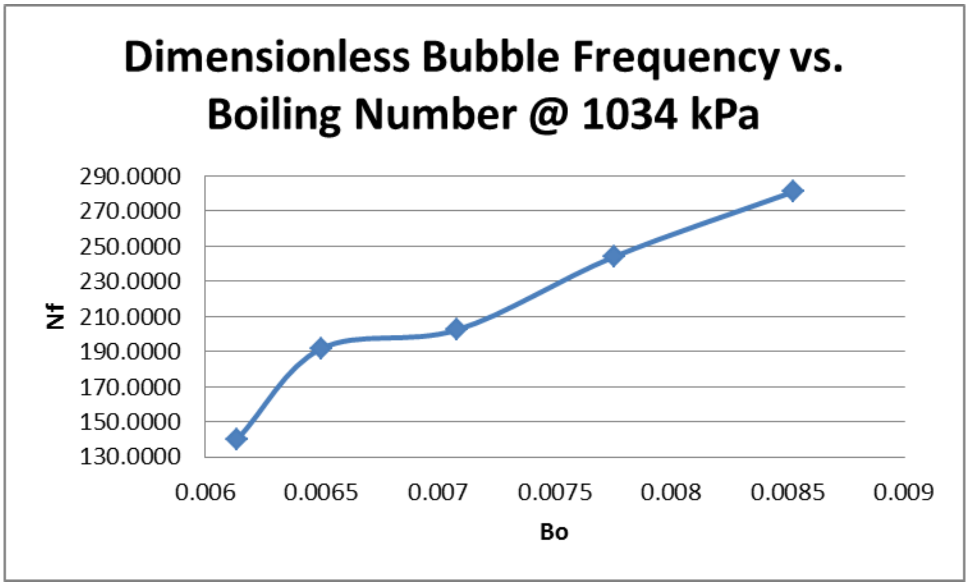

Figure 64: Dimensionless Bubble Generation Frequency vs. Boiling Number at P=1034 kPa

Inlet Subcooling at Different Pressures

Table 2: Inlet Subcooling at Different Pressures

Pressure (kPa)	**Inlet Subcooling Diff. °C**	**Avg. Inlet Subcooling**
621	0.25	0.446±0.088
689	0.19	2.620±0.068
758	0.09	5.884±0.032
827	0.13	9.072±0.050
896	0.61	12.715±0.215
965	0.28	14.432±0.104
1034	0.16	16.441±0.060

In Table 2 above, numerical calculations are performed to obtain the inlet subcooling difference and average inlet subcooling. The calculations are performed to assess the severity of changes in the inlet subcooling. The difference in inlet subcooling shows that for any given system pressure, the inlet subcooling never deviates more than 1°C throughout all of the imposed heat flux cases. The average inlet subcooling is the average of the inlet subcooling values for all heat flux cases at any particular system pressure. The standard deviation for the entire population of heat flux cases is also exhibited.

Bubble Propagation

Generally, it is accepted that flow boiling experiments under subcooled conditions will be characterized as bubbly flow on the surface heater. In the figures below, the bubble growth is shown with respect to time. The bubble propagation shown below is a snapshot of the flow phenomenon at a pressure of 896 kPa, low mass flux of 484.838 kg/m^2s, and heat flux of 496.1 kW/m^2.

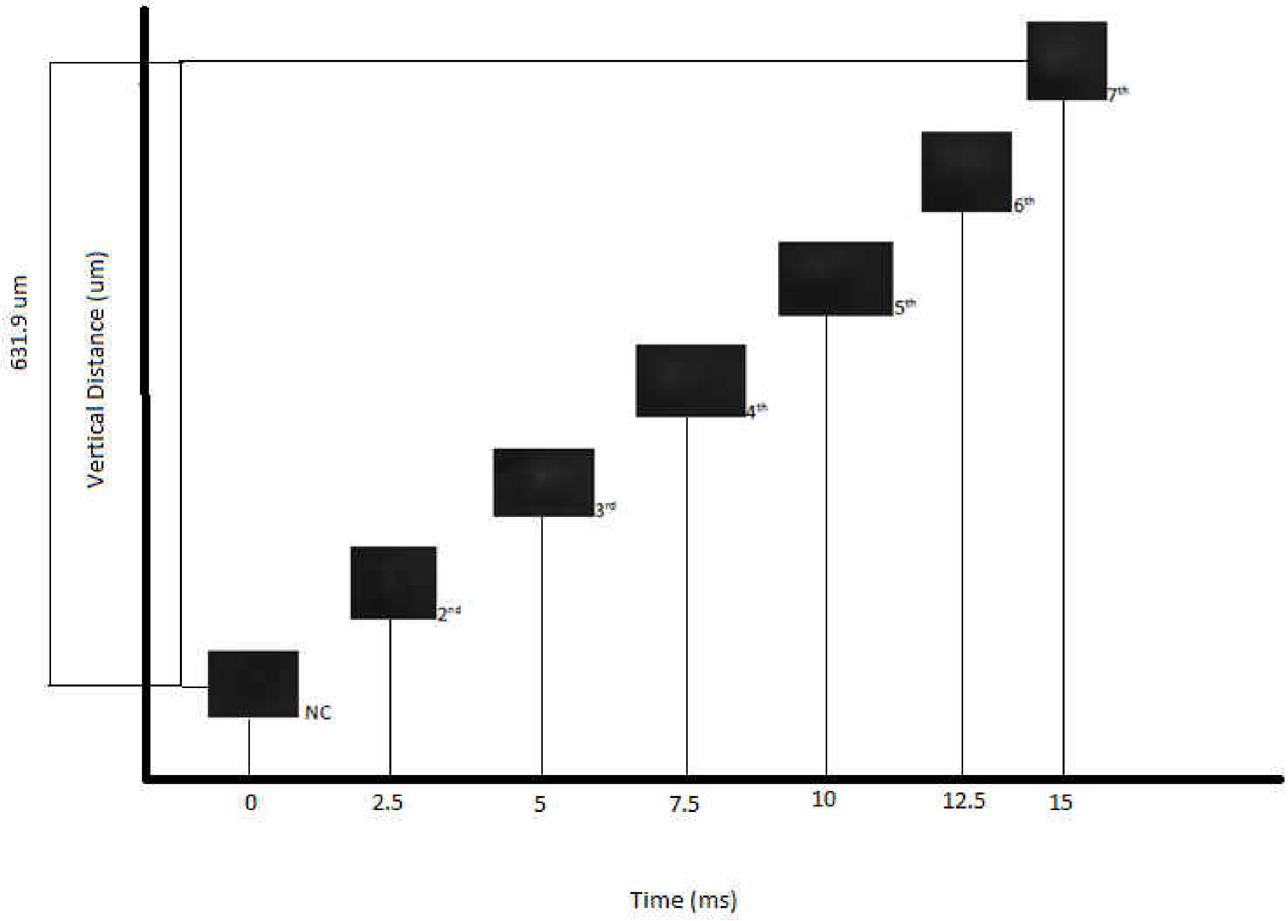

Figure 65: Visual bubble propagation with respect to time at P=896 kPa and q''=496.1 kW/m2

In the figure above, the bubble propagation is shown with respect to time. The images illustrate the incipience of boiling starting at the nucleation site. Afterward, the subsequent images propagate up to the seventh image, the peak bubble size, before coalesce or collide with another bubble. From incipience to peak bubble diameter, the bubbles travel a total of 631.9 µm in total vertical distance.

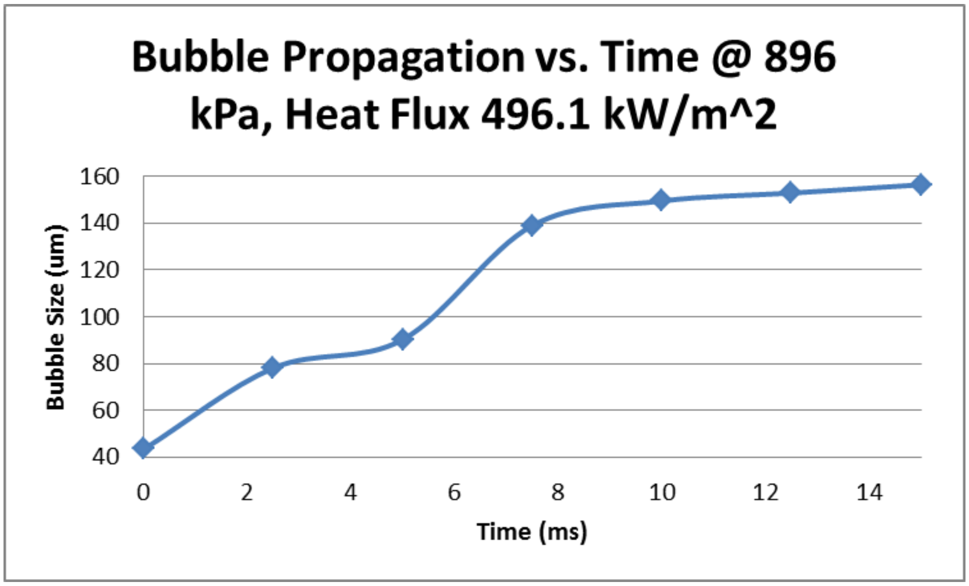

Figure 66: Bubble growth with respect to time a P=896 kPa and q''=496.1 kW/m2

In the figure above, the size of bubble propagation is outlined versus time. The figure above portrays the nucleation site, the growth, the departure, and the subsequent rising bubbles along the heater surface. After nucleation, the bubble size obtains more energy (more latent heat of vaporization) until departure (the 4th image). After departure, the bubble growth rate begins to gradually decline as can be depicted in the figure above.

Sequential Wall Temperature at Nucleation

Utilizing the same case as used in the bubble propagation, the sequential wall temperature at the nucleation site will be determined over a period of time. In the figure below, the sequential wall temperature is shown for a pressure of 896 kPa with heat flux of 496.1 kW/m^2. The sequential temperature profile illustrates the possible cooling effects during boiling.

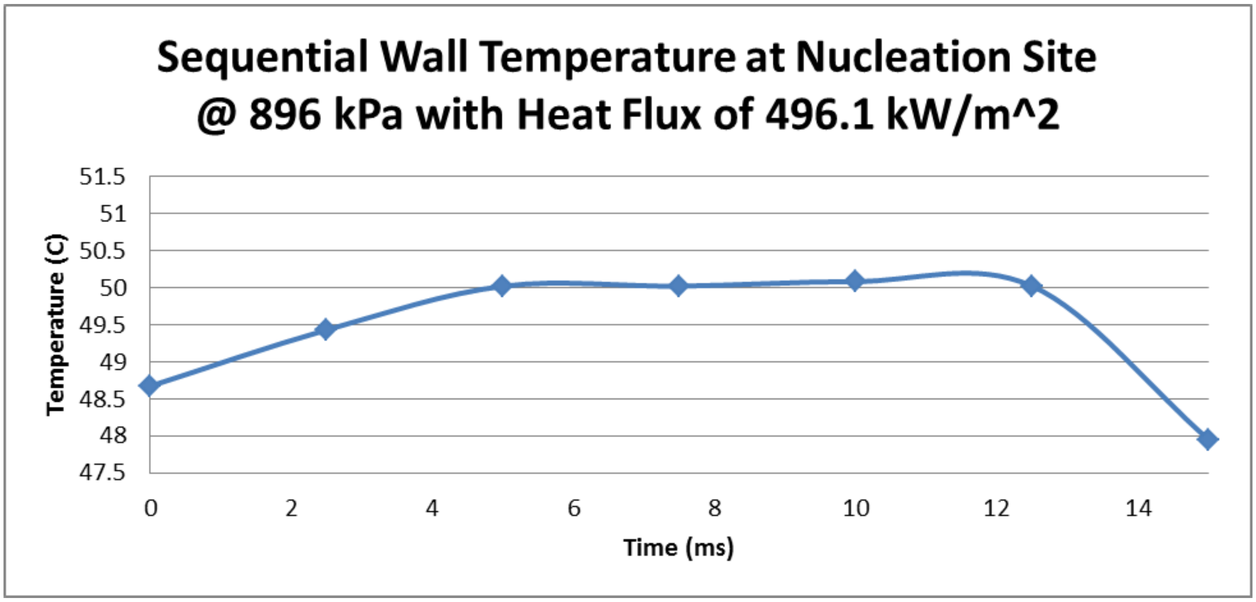

Figure 67: Sequential Wall Temperature at Nucleation Site at Pressure of 896 kPa with Heat Flux of 496.1 kW/m2.

In figure 67 above, the temperature profiles at nucleation are shown. At a particular nucleation site, the site gains a certain amount of latent heat energy whereby the local wall temperature increases with the growth of the bubble. The bubble reaches a critical size and junction where it displaces away from the nucleation site known as the departure point. After departure, the temperature at the nucleation site drops in temperature until another bubble nucleates at the same activity site. In the figure above, the rise and fall phenomenon (typically characteristic of a sinusoidal trend) can be exhibited whereby the wall temperature increases along with the bubble until departure (after 7.5ms). Afterward, the temperature at the activity site drops in temperature, then grows agains once a new bubble originates.

Effect of Pressure on Bubble Characteristics

Table 3: Effect of Pressure on Bubble Characteristics

Pressure (kPa)	Heat Flux (kW/m^2)	Mass Flux (kg/m^2s)	Tw (C)	frequency (Hz)	Bubble size (um)
896	429.4	484.838	45.67	254.00	135.60
965	425.6	484.838	48.38	259.00	147.56
ΔP	$\Delta\ Heat\ Flux$	$\Delta Mass\ Flux$	ΔT	Δf	ΔD_b
69	3.8	0	2.71	5.00	11.96

Experimental results are shown in the table above. The table assesses the effect of pressure on bubble dynamic parameters by increasing the pressure from 896 kPa to 965 kPa while maintaining the mass flux and keeping the heat flux approximately around 430 kW/m^2. It is found that the pressure does affect the bubble dynamic parameters. For example, an increase in the pressure of about 69 kPa increased the bubble frequency and size by about 5Hz and 11.96μm respectively. It is also shown that the wall temperature increased by 2.71°C. Since there was an increase in wall temperature, another assessment is made to understand the cooling effects at different pressures. In the figure below, the cooling effects are illustrated at different pressures.

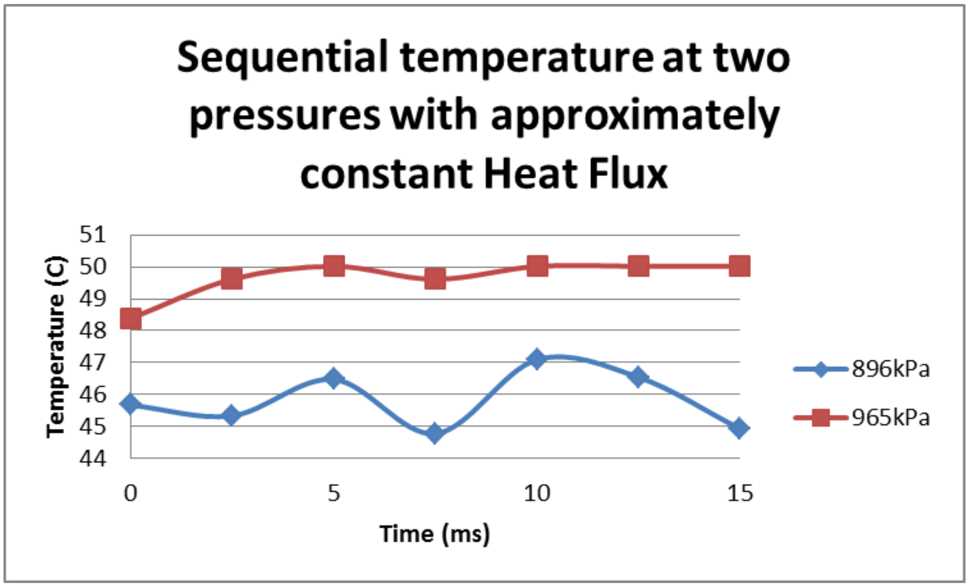

Figure 68: Sequential temperature profile at two different pressures with approximately constant heat flux of 430 kW/m2. The mass flux is held constant at 484.838 kg/m2s.

In figure 68 above, the plot represents a time dependent temperature profile at a particular localized nucleation site for two different pressures. As expected, the lower pressure has a lower temperature profile. The higher pressure has a higher temperature profile. Both time dependent temperature profiles exhibit similar trends. Therefore, researchers can conclude that at higher pressures it requires a higher wall temperature to generate the same or similar nucleation activity.

Bubble Coalescence

For visualization purposes, the figure below has a few images pre and post bubble coalescence at high pressure of 1034 kPa and high heat flux of 672.1 kW/m^2. During the pre-coalescence stage, the bubble images are still spherical in shape. As the bubbles begin to coalescence, the combined bubble is elongated horizontally. During the post-coalescence stage, the bubble image shows an elongated bubble vertically as it continually rises along the wall. After the post-coalescence stage, the bubble reshapes into spherical formation. The process in the figure below goes from bottom to top.

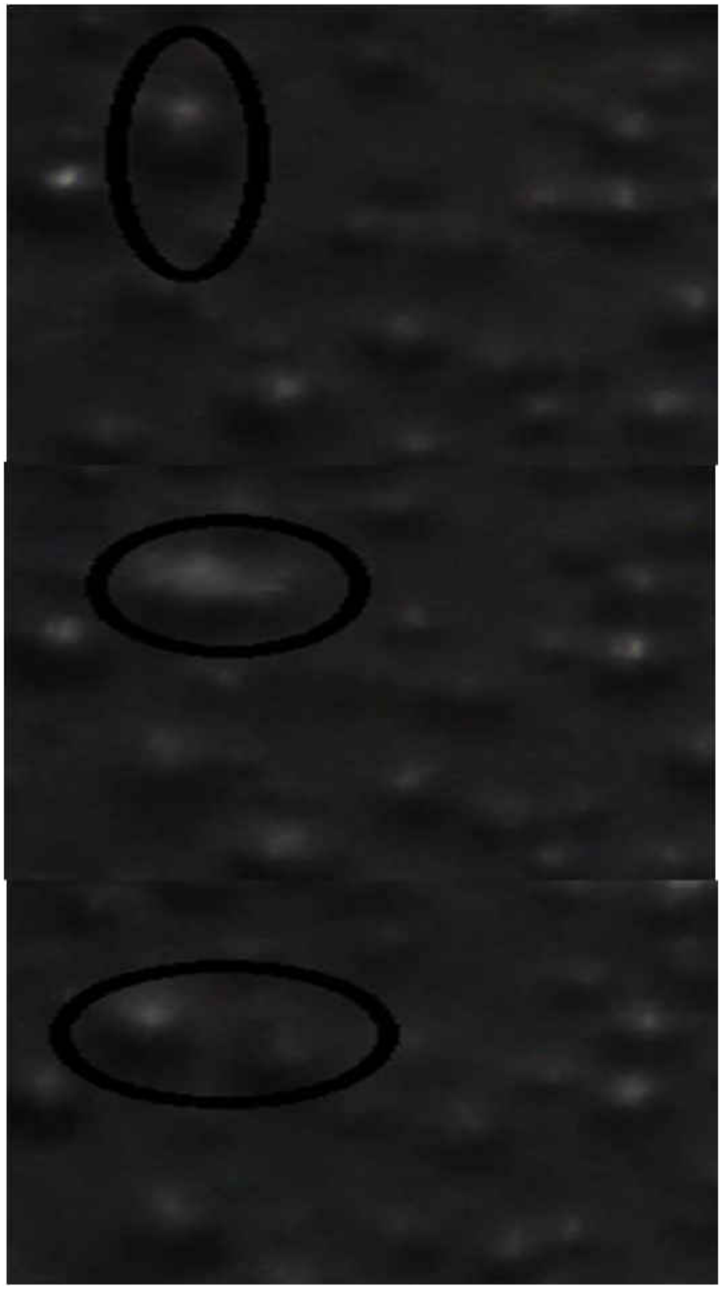

Figure 69: Bubble Coalescence at P=1034 kPa and Heat Flux of 672.1 kW/m^2

Effect of Different Mass Fluxes on Bubble Dynamic Parameters

With an increase in the mass flux, it has been postulated by many other researchers that the bubble dynamic parameters would be affected. From literature, it has been shown by Kandlikar et al, and others that the departure bubble size should decrease with an increase in the mass flux. With a higer flow velocity, the inertial forces are greatly enhanced which allows the bubbles to leave the nucleation site faster; ultimately, decreasing the overall size of the departed bubble. To illustrate this point, a comparison was performed to assess the bubble dynamic parameters. From other studies within literature, it was postulated that increasing mass flux would ultimately decrease the wall superheat while increasing the bubble frequency. Specifically, mass fluxes of 484.838 kg/m^{2}s and 1212.1 kg/m^{2}s will be compared at a pressure of 758 kPa. It should also be noted that in order to induce bubble generation at higher flow velocity it requires more heat flux for similar pressures. For instance, the table below shows how much more heat flux is required to generate bubbles.

Table 4: Effect of Mass Flux on Heat Flux Requirement

Pressure: 758 kPa	
Mass Flux: 484.838 kg/m^{2}s	Mass Flux: 1212.1 kg/m^{2}s
Heat Flux (kW/m^2)	
323.2	410.7
385	488
451.4	576.2
562.8	620.4
673.2	720

In the figures below, the bubble dynamic parameters are compared for different mass fluxes. In figure 70, it is shown that with an increase in mass flux the wall superheat increases. This result is opposite to that found in literature studies. In figure 71, the bubble departure size is shown to decrease with an increase in mass flux which matches results found from other literature studies. As the heat flux gets very high, the departure bubble size for the higher mass flux eventually gets closer to the values of the lower mass flux. Therefore, even though the flow velocity ultimately makes the system capable of transfering heat more efficiently, the heat flux plays a significant role in the rate of increase for any of the bubble dynamic parameters. In figure 72, the bubble frequency increased with an increase in mass flux. At this particular pressure, the heat flux values are approximately 100 kW/m^2 bigger than the low mass flux cases. As a result, bubble generation occurs at a faster rate.

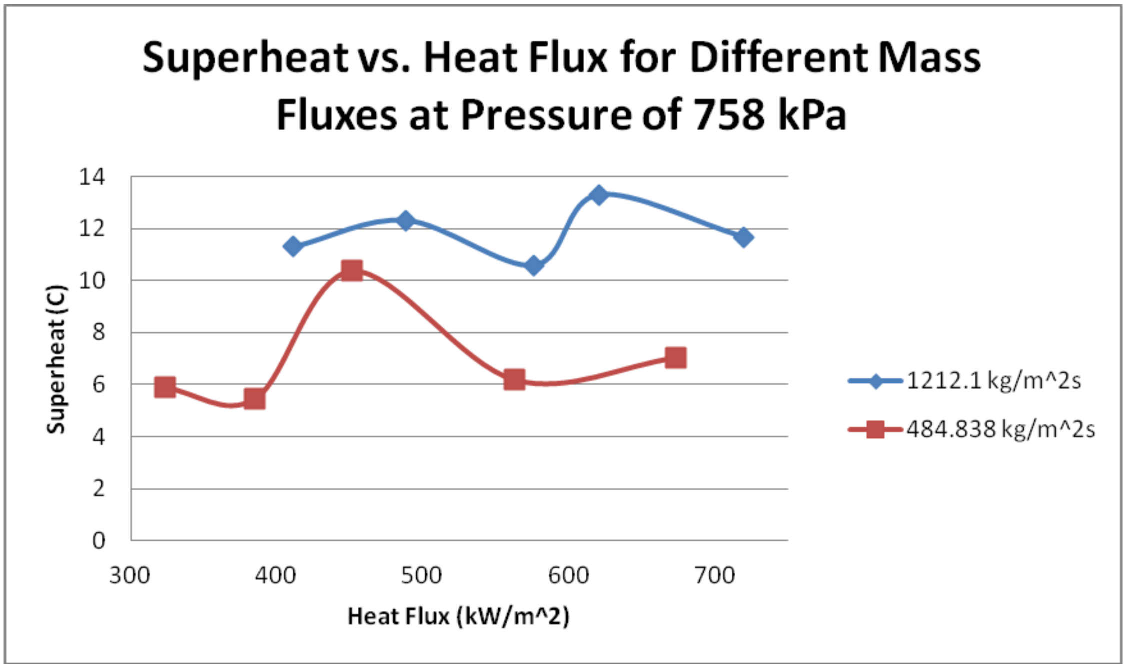

Figure 70: Superheat vs. Heat Flux for Different Mass Fluxes at P=758 kPa

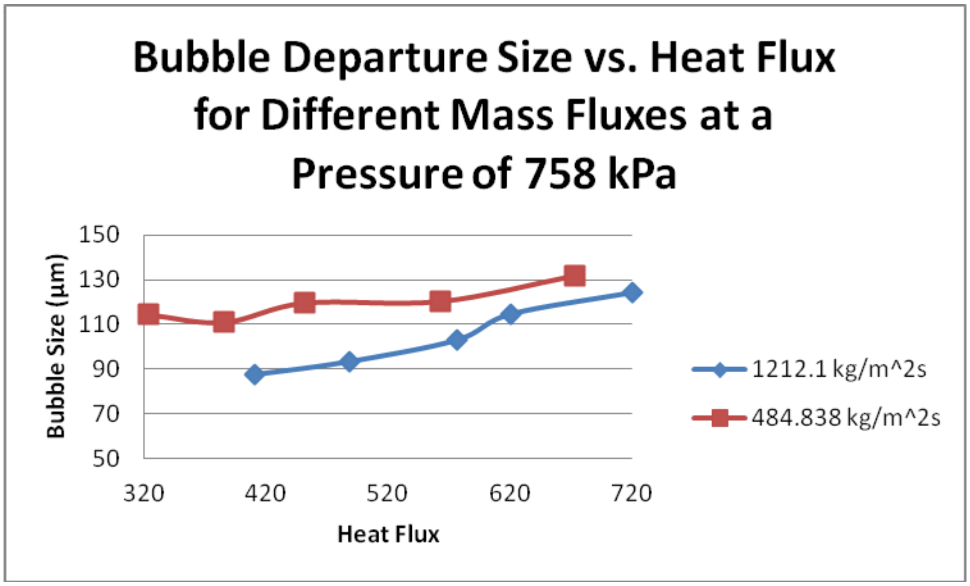

Figure 71: Bubble Departure Size vs. Heat Flux for Different Mass Fluxes at P=758 kPa

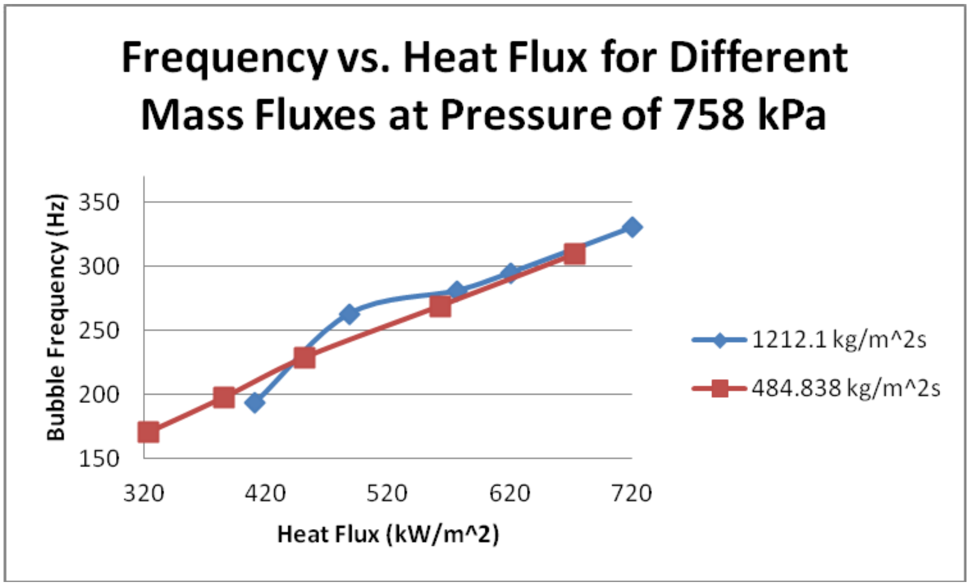

Figure 72: Bubble Frequency vs. Heat Flux for Different Mass Fluxes at P=758 kPa

The full set of mass flux data for 1212.1 kg/m^{2}s can be found in Appendix F. Since the non-dimensional variables are based off of the dimensional variables with similar trends, Appendix F will only illustrate the dimensional variables. From this data analysis, the bubble departure size will ultimately reduce with an increase in mass flux with more or less similar heat flux. The bubble generation frequency will increase with an increase in mass flux. From the analysis, the wall superheat for pressures ranging from 621 kPa to 827 kPa will increase with an increase in mass flux while pressures ranging from 896 kPa to 1034 kPa will decrease with an increase in mass flux.

CHAPTER FIVE: CONCLUSION

An experimental study is performed to determine the effect of heat flux and pressure on the flow boiling of refrigerant R-134a. A non-intrusive technique called thermochromic liquid crystallography (TLC) ranging from 30-50°C is used to map the surface temperature of the corresponding bubble nucleation site. Since the experiments are conducted under subcooled conditions, the flow region observed is bubbly flow. Based on the analysis completed, bubble parameters such as size and frequency are calculated. Temperature contours are utilized to determine the surface wall temperature. Bubble propagation and coalescence are visualized.

Results provided analysis on size, frequency, and wall superheat for different pressures with incremental changes in heat flux. The variables were non-dimensionalized to note trends in parameters. The results are summarized below.

- No conclusive evidence on wall superheats with increase in non –dimensional heat flux for the particular heat flux range. The localized activity site tends to play a significant role in wall superheat.
- An increase in the non-dimensional heat flux yields an increase in the non-dimensional bubble size ratio. As the pressure increases, the bubble departure correlation increases.
- An increase in the non-dimensional heat flux yields an increase in the non-dimensional bubble generation frequency. With higher pressures, more of the region of interest is filled with activity sites. Therefore, there are faster growth rates at higher pressures with high heat flux values.

- Under subcooled conditions, the bubble maintains its spherical shape. After departure, the bubble typically slides along the wall surface. After departure, the bubbles' growth plateaus.
- An increase in pressure, while maintaining mass flux and heat flux increases the wall temperature, departure bubble size, and bubble frequency.
- With an increase in mass flux, the bubble generation frequency always increased; the wall superheat increased between pressures of 621 kPa to 827 kPa then decreased from 896 kPa to 1034 kPa; the bubble departure size decreased with increase in mass flux.

APPENDIX A: REFRIGERANT R134A CHARACTERISTICS

Table 5: R134a Characteristics; utilizing the gravitational constant (g) of 9.8 m/s2

Psat (kPa)	Tsat	Psat (psi)	density pl [kg/m^3]	density pv [kg/m^3]	delta density (rho)	hl [kJ/kg]	hlv [kJ/kg]	cpl [kJ/kg*K]
620.53	22.25	90.00	1217.09	30.20	1186.88	230.51	180.17	1.42
689.48	25.72	100.00	1203.95	33.60	1170.35	235.56	177.00	1.43
758.42	29.19	110.00	1190.82	36.99	1153.82	240.61	173.83	1.45
827.37	32.50	120.00	1178.09	40.42	1137.67	245.44	170.73	1.46
896.32	35.08	130.00	1167.24	44.01	1123.23	249.19	168.03	1.47
965.27	37.65	140.00	1156.39	47.59	1108.79	252.93	165.33	1.49
1034.21	40.23	150.00	1145.54	51.18	1094.36	256.68	162.63	1.50
cpv [kJ/kg*K]	**ul [uNs/m^2]**	**uv [uNs/m^2]**	**kl [mW/mK]**	**kv [mW/mK]**	**Prl**	**Prv**	**sigma [mN/m]**	**Do**
1.02	205.55	11.68	82.30	13.73	3.53	0.88	8.46	1.63E-04
1.04	196.90	11.83	80.82	14.01	3.48	0.88	8.02	1.45E-04
1.07	188.25	11.98	79.33	14.28	3.42	0.89	7.57	1.31E-04
1.08	180.14	12.12	77.91	14.56	3.38	0.90	7.14	1.18E-04
1.10	174.60	12.27	76.81	14.87	3.35	0.91	6.81	1.08E-04
1.12	169.07	12.42	75.71	15.19	3.32	0.92	6.48	9.92E-05
1.14	163.53	12.57	74.61	15.50	3.29	0.93	6.15	9.17E-05

APPENDIX B: SAFETY PROTOCOL

While the experiment is running, there are certain safety precautions that need to be taken.

1. Wear safety glasses at all times during the experiment
2. Put in place the acrylic shields that will enclose the experiment to protect the rest of the lab in the event of a high pressure explosion

APPENDIX C: PRE-EXPERIMENTAL SETUP

Pressure Test

1. Use the Husky compressor to fill up the loop to a system pressure of 135 psi
2. The system pressure should hold for a least sixty minutes
3. If there is the slightest leak during the pressure test, the entire loop has to be re-tighten including the test section until the leak stops
4. Once the loop has passed the pressure test, then the experiment can be safely filled up with refrigerant R134a without having any leaks

Calibration Test

1. For every new TLC installed into the test section, there needs to be a new in situ calibration since every TLC doesn't yield exactly the same calibration curve.
2. In order to perform a correct in-situ calibration, the lighting has to be the same as it will be during experimentation.
3. The high current power supply heats up the TLC and thus increases the temperature.
4. Once the temperature is above the maximum range of the TLC, the power supplied to the system is shut off and the TLC is allowed to cool down toward the minimum temperature.
5. LabVIEW acquires the temperature with accompanying time stamps
6. Streampix camera software takes a single snapshot of the thermocouple location to pinpoint its (x, y) location using the GUI interface

7. Streampix camera software takes the time-stamped images of the color camera and imports them into the GUI interface. After doing a proper-alignment of the monochrome camera and the RGB camera using reference points, the (x, y) location for the color images can be directly matched to the thermocouple location.
8. The GUI interface will export the hue angles into a excel file
9. The calibration curve becomes generated with a fifth order polynomial fit

Vacuum Test

1. The test occurs after completing the pressure test and prior to filling the loop up with R134a.
2. The R134a tank has to be attached so that its line can be vacuumed as well.
3. The system has to vacuum any air out of the system to avoid contamination between air and R134a.
4. Before running the vacuum pump, discharge port needs to be open
5. the blue dial on the yellow jacket manifold needs to be open
6. the red dial on the yellow jacket manifold needs to be open
7. The Platinum JB vacuum pump will run for approximately two minutes
8. after, close the discharge port
9. close the red dial on the yellow jacket manifold
10. the system is ready for experimentation

Electrical Connection Test

1. Check for contact to ensure that electricity will be supplied to the system prior to running.
2. Use Ex330 Auto Ranging Multimeter to check contact within the system. Place the black and red leads onto the electrical connections of the test section.
3. Turn the dial on the multimeter to resistance and check to see if the reader goes to 0.000 Ohms.
4. If not, then there is something wrong and power cannot be supplied to the system without proper contact.
5. Contact has to be established before experiment begins. The connections cannot be adjusted due to the increased risk of leaks which would leaks to cracks to propagate within the test section.

APPENDIX D: EXPERIMENTAL SETUP

Loop Filling Procedure

1. Connect recovery pump to recovery tank
2. close discharge port
3. open evac port
4. open refrigerant port
5. turn on leak detector
6. open refrigerant valve to allow for the refrigerant to flow into the system
7. refrigerant R134a will fill up the loop up to its own system pressure around 70 psi
8. the heat gun is turned on and applied to the refrigerant tank to increase the amount of refrigerant in the system
9. A full loop is considered to be around a mass flow at 0.5 GPM or mass flux of $G=1212.1$ kg/m^{2}s.
10. From the pressure gauge, the system pressure should increase to 110 psi. After this system pressure is reached, the loop can be considered full.
11. Afterward, close the refrigerant valve and close the refrigerant port
12. turn on the chiller at a desirable temperature
13. turn on the flow pump

Testing Procedure

1. turn on LabVIEW and Streampix
2. turn on LED controller and set it at 70% intensity to yield optimum lighting
3. adjust chiller to yield a particular system pressure
4. once the system pressure has held for over two minutes, the system can be considered to be in equilibrium
5. Afterward, data collection can commence
6. begin to adjust the amount of electricity being supplied to the system using the high current power supply
7. once there is simultaneous color change of TLC and corresponding nucleation of bubbles, then collect data at that particular heat flux
8. gather a total of five different heat flux conditions at the same system pressure and same mass flux
9. the process is repeated until all sets of data are gathered

Discharge Procedure

1. turn off the power supply
2. turn off the chiller
3. turn off the flow pump
4. turn off the LED controller
5. re-open the refrigerant port

6. on the yellow jacket manifold, the red dial should be closed and the blue dial should be open

Recovery Pump Section:

7. black knob should be on recovery
8. red knob should be open with the recovery tank valve open (alleviate high pressure buildup within recovery pump)
9. blue knob should be on liquid
10. turn on the recovery pump by pressing power button first, then the start button
11. afterward, open the discharge port
12. oscillate the blue knob on recovery pump between open and liquid until all refrigerant has been removed from the system
13. on the blue pressure gauge of the yellow jacket manifold, the pressure readings should show well below zero
14. If this is the case, then close the discharge port
15. turn the blue knob on the recovery pump to closed
16. turn off the recovery pump
17. turn the blue knob on recovery pump to purge
18. turn the recovery pump back on
19. let the pump discharge all the refrigerant into the recovery tank
20. after the blue pressure gauge on the recovery pump has gone down to zero, turn the red knob on the recovery pump to closed

21. close the recovery tank valve (red)
22. shut off the recovery pump and turn the black knob back to recovery
23. afterward, take both the refrigerant and recovery tanks off to be measured
24. The refrigerant tank will be weighed (checking for emptiness) ----empty around 10 lbs.
25. The recovery tank will be weighed (checking for safety) ---this tank cannot exceed over 32 lbs.
26. store refrigerant and recovery tanks in their storage units

APPENDIX E: ERROR PROPAGATION AND UNCERTAINTY

There are two types of errors in this experiment. The systematic errors or bias errors are the errors that remain constant over repeated trials of similar variables. The systematic errors are minimized by performing careful calibration procedures. The other type of error in this experiment is the precision error. This error varies randomly over repeated trials of similar variables. Statistical operations are utilized to deal with the precision error. When determining the uncertainties of measured parameters such as heat flux, inlet bulk temperature, and TLC wall temperature, the combined elemental approach root-sum squares (RSS) method is used. The relative heat flux uncertainty is shown in the equations below. The uncertainties for the supply voltage and current are ±0.2% and ±0.5% respectively. The heater area uncertainty is considered ±0.2%. Inputting the values into the RSS method, the combined elemental uncertainty for the heat flux is considered ±0.6%. The relative uncertainties for other parameters are also shown in Table 6 below.

$$\frac{\delta q}{q} = \sqrt{\left(\frac{\delta I}{I}\right)^2 + \left(\frac{\delta V}{V}\right)^2 + \left(\frac{\delta A}{A}\right)^2} = \sqrt{0.2^2 + 0.5^2 + 0.2^2} = \pm 0.6\%$$

Table 6: Parameters with included estimated uncertainties

Parameters	**Equipment/Materials**	**Relative Uncertainty (±)**
Pressure	Yellow Jacket Manifold Pressure Gauge	1%
Inlet Temperature	K-type thermocouple at inlet portion of test section	0.3%
Wall Temperature	TLC sandwiched on Fecralloy heater foil section	0.5%
R134a flow rate	Omega Flow Meter	1%
Heat Flux	BK Precision 1794 DC Power Supply and Heater Area	0.6%

Repeatability Cases

In order to access whether or not the data and analysis are valid, repeatability cases are performed. Under these cases, the system pressure is set at 689 kPa (T_{sat}=25.716°C), the mass flux is set at 484.838 kg/m^{2}s, and the heat flux is set at 356.5 kW/m^2. These parameters are held constant throughout the repeat cases (total of 3 cases). Under observation, the following items are compared: wall temperature, degree of superheat, initial bubble size, departure bubble size, bubble frequency, bubble velocity, non-dimensional bubble frequency, and non-dimensional bubble diameter ratio. The following items with their corresponding arithmetic means and standard deviations are shown in Table 7 below.

Table 7: Repeatable cases with constant system pressure, mass flux, and heat flux. P=689 kPa (Tsat=25.716°C), G=484.838 kg/m2s, and q"=356.5 kW/m2.

	T_w (C)	Superheat (C)	Initial Bubble Size (um)	Departure Bubble Size (um)	Frequency (Hz)	Velocity (m/s)	N_f	D/D_o
Case 1	33.691	7.975	82.013	157.556	154.000	0.029	79.313	1.084
Case 2	34.668	8.951	84.030	155.540	158.000	0.029	79.303	1.070
Case 3	34.790	9.074	84.030	155.456	154.000	0.028	77.212	1.069
Mean	34.383	8.666	83.358	156.184	155.333	0.029	78.610	1.074
Standard Deviation	0.492	0.492	0.951	0.971	1.886	1.405E-04	0.988	0.007

In the plots below, a visual representation of the cases outlined in Table 7 above will be shown with the corresponding error bars provided.

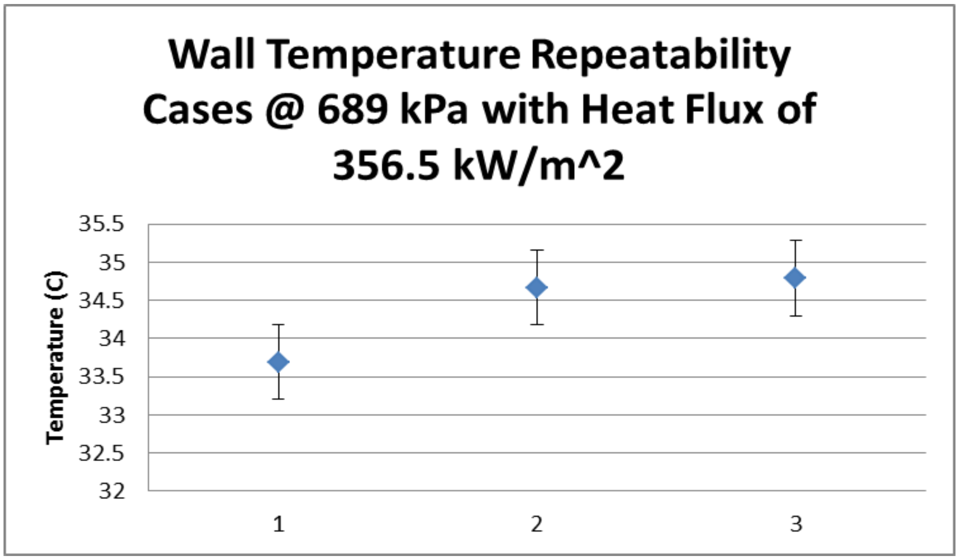

Figure 73: Wall Temperature Repeatability Cases. The error bars show that the wall temperature falls within ±0.5°C of the mean

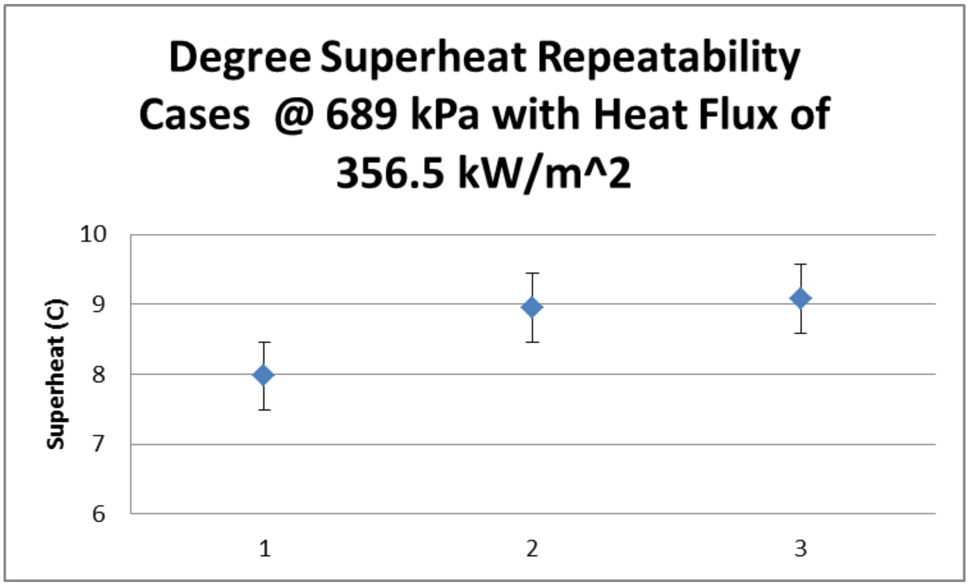

Figure 74: Degree of Superheat Cases. The error bars show that the degree of superheat falls within ±0.5°C of the mean value for each case.

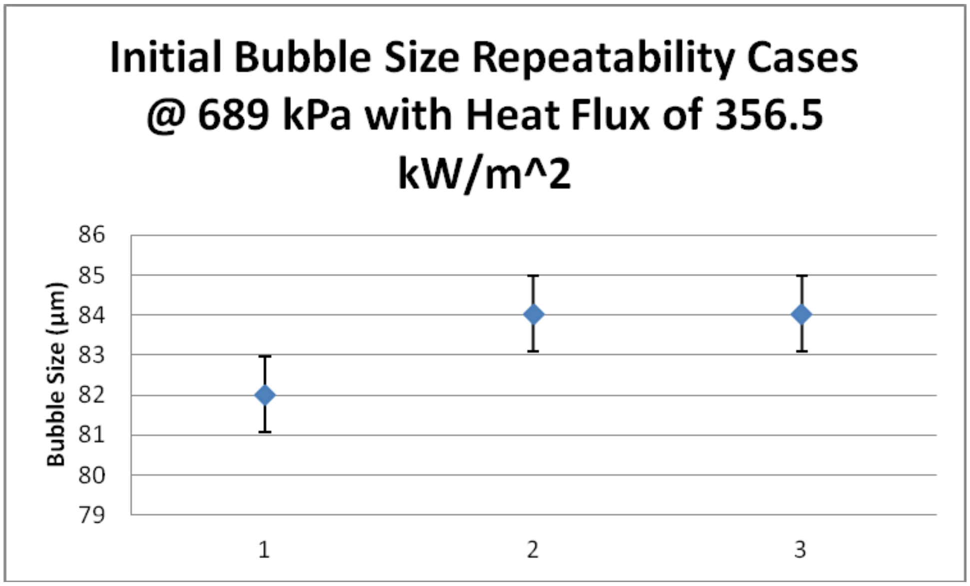

Figure 75: Nucleation Bubble Size Repeatable Cases. The cases are within ±1µm of the mean.

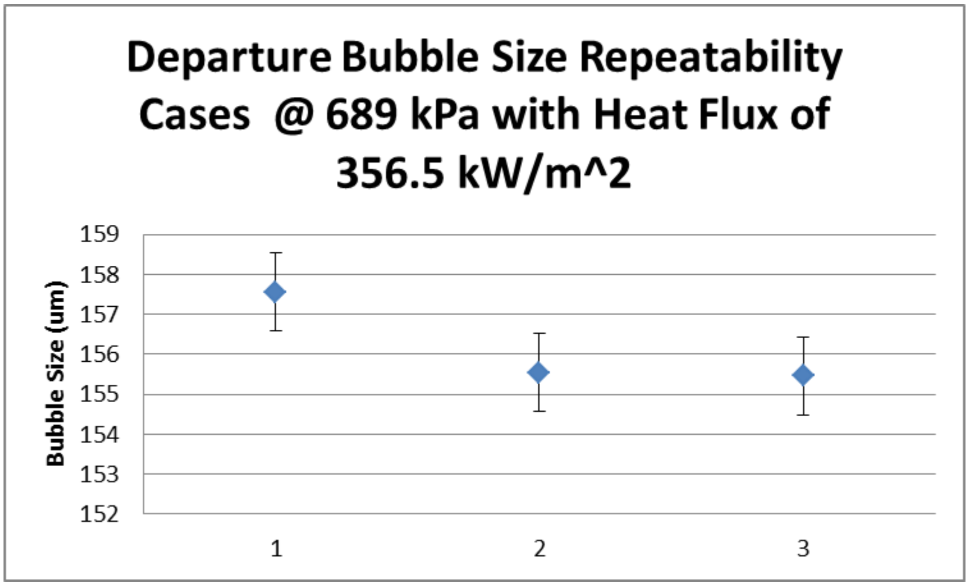

Figure 76: Departure Bubble Size Repeatable Cases. The cases are within ±1µm of the mean.

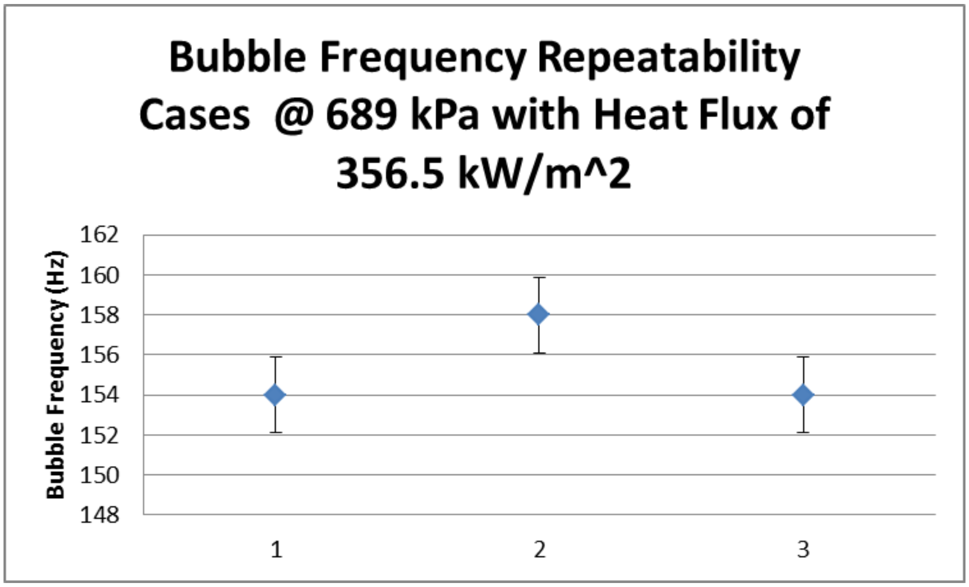

Figure 77: The bubble frequency repeatability cases are within approximately ±2Hz of the mean.

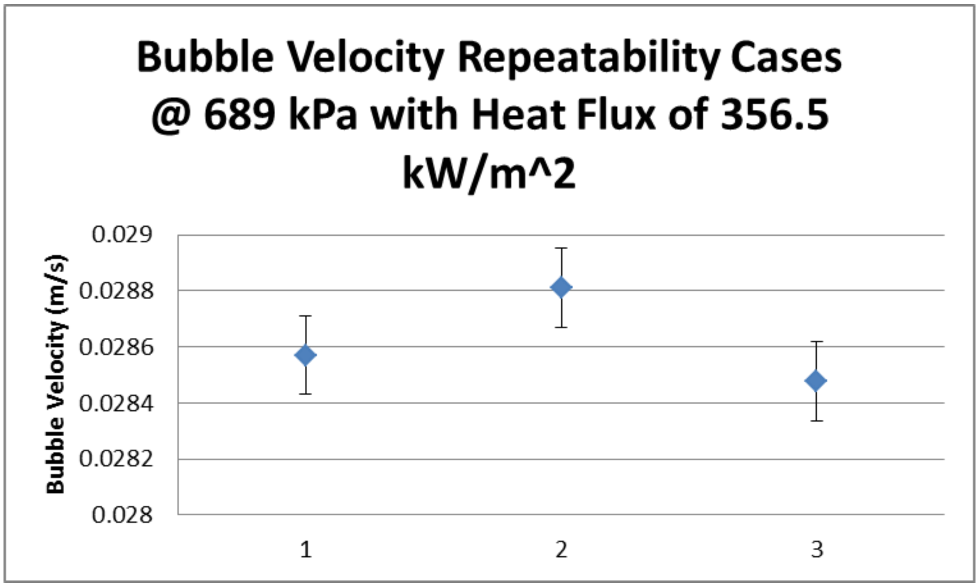

Figure 78: The bubble velocity repeatability cases are within approximately ±.00015 m/s of the mean.

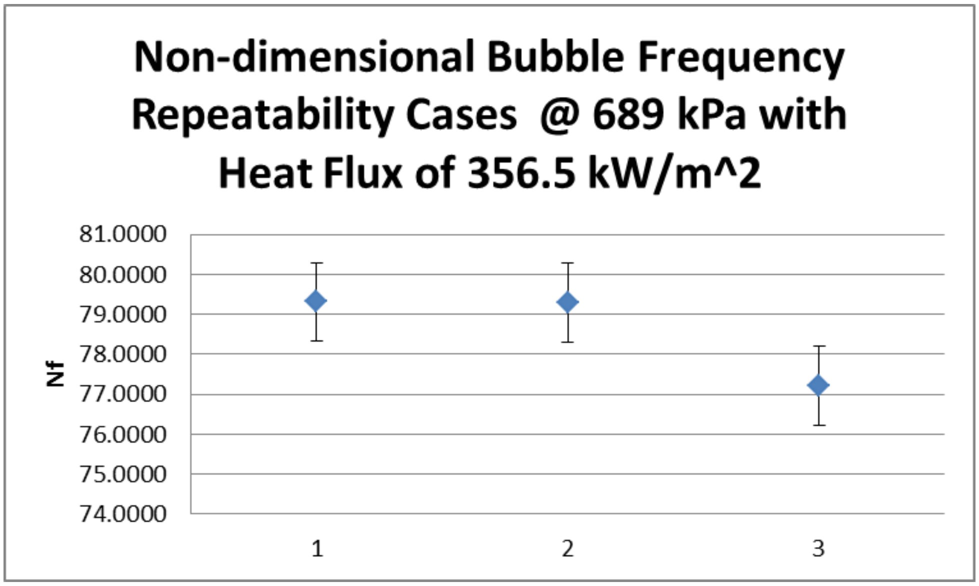

Figure 79: The dimensionless bubble frequency repeatability cases are within approximately ±1 of the mean

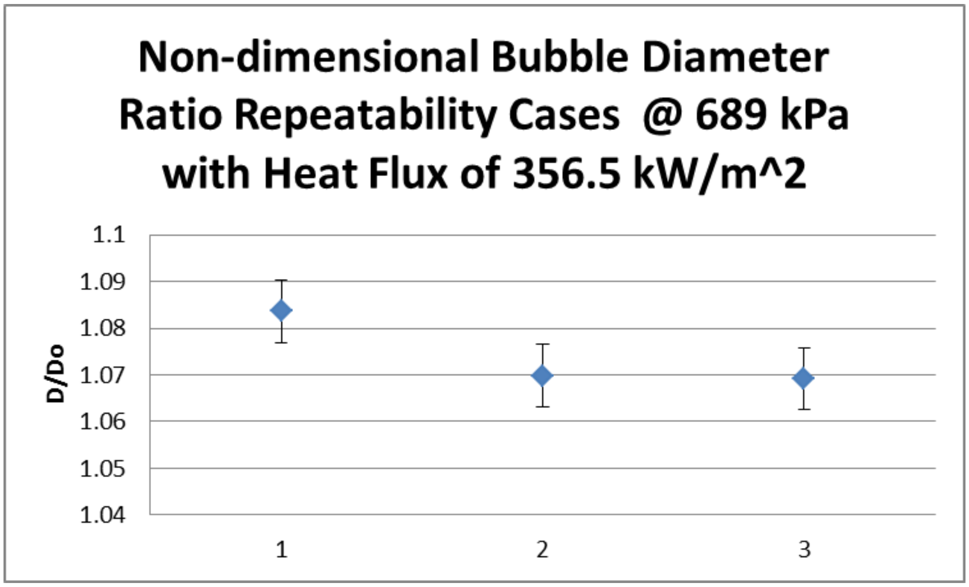

Figure 80: The dimensionless bubble diameter ratio repeatability cases are within approximately ±0.007 of the mean. Also, the above repeatable cases match well with the Cole and Rohsenow correlation.

By performing analysis on the cases above, it is clear that the data is repeatable. It is also noticeable that for each item under analysis, the error is relatively low compared to the mean.

APPENDIX F: DATA ANALYSIS ON MASS FLUX OF 1212.1 KG/M^{2}S

Effect of Heat Flux on Degree of Superheat

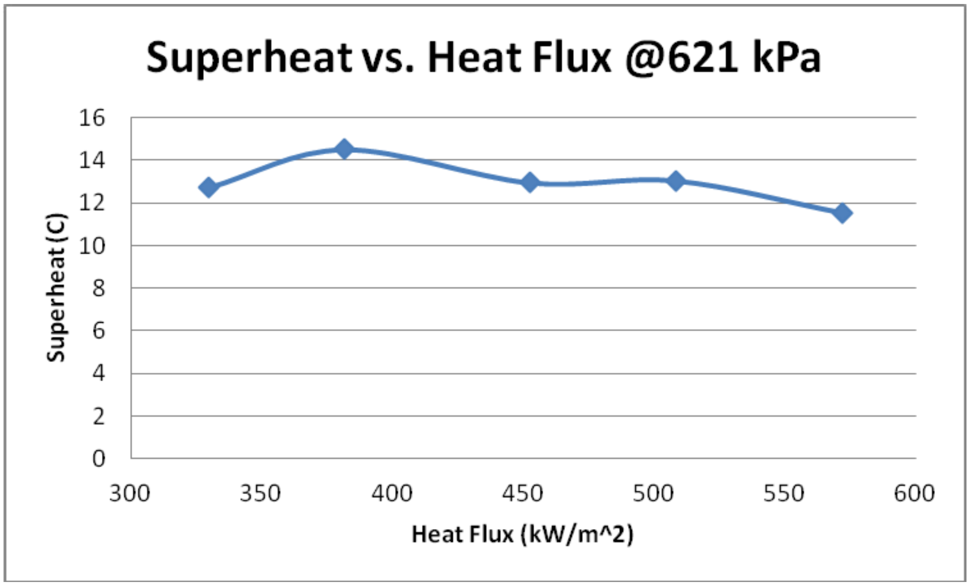

Figure 81: Superheat vs. Heat Flux @621 kPa, G=1212.1 kg/m^{2}s

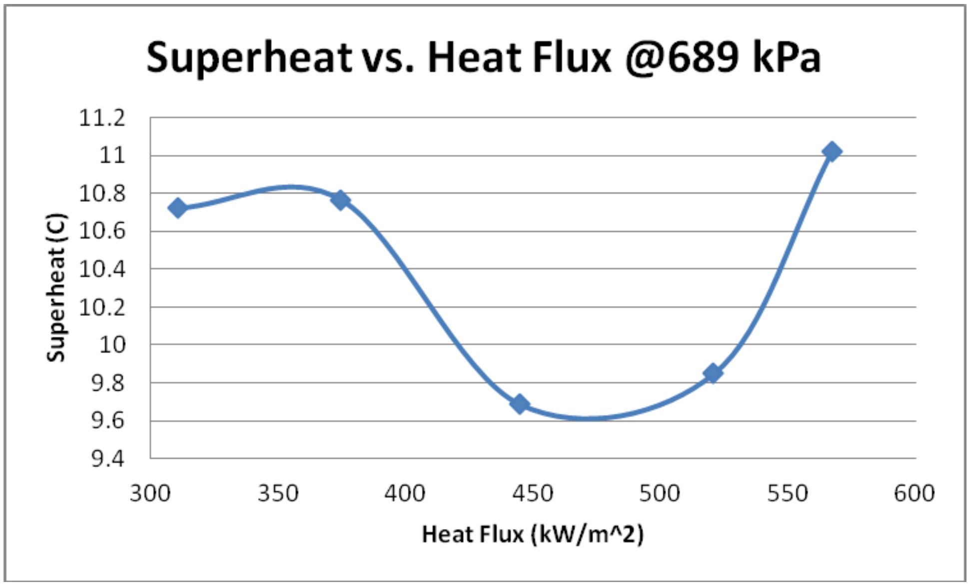

Figure 82: Superheat vs. Heat Flux @689 kPa, G=1212.1 kg/m^{2}s

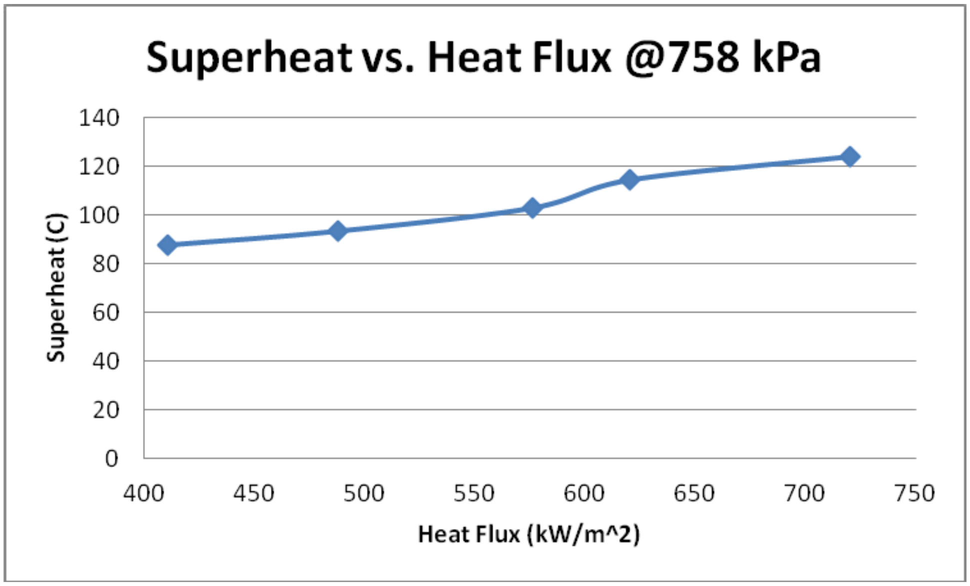

Figure 83: Superheat vs. Heat Flux @758 kPa, G=1212.1 kg/m^{2}s

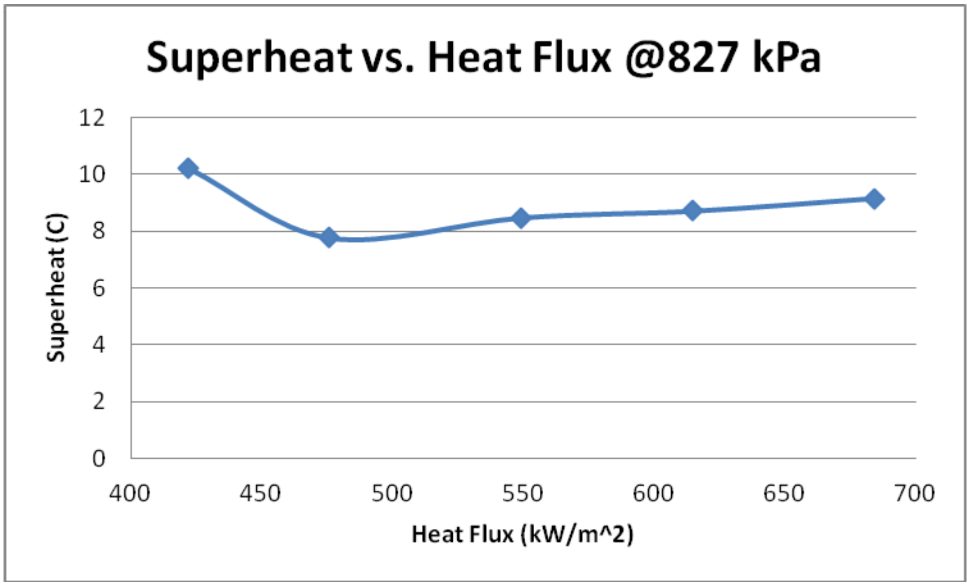

Figure 84: Superheat vs. Heat Flux @827 kPa, G=1212.1 kg/m^{2}s

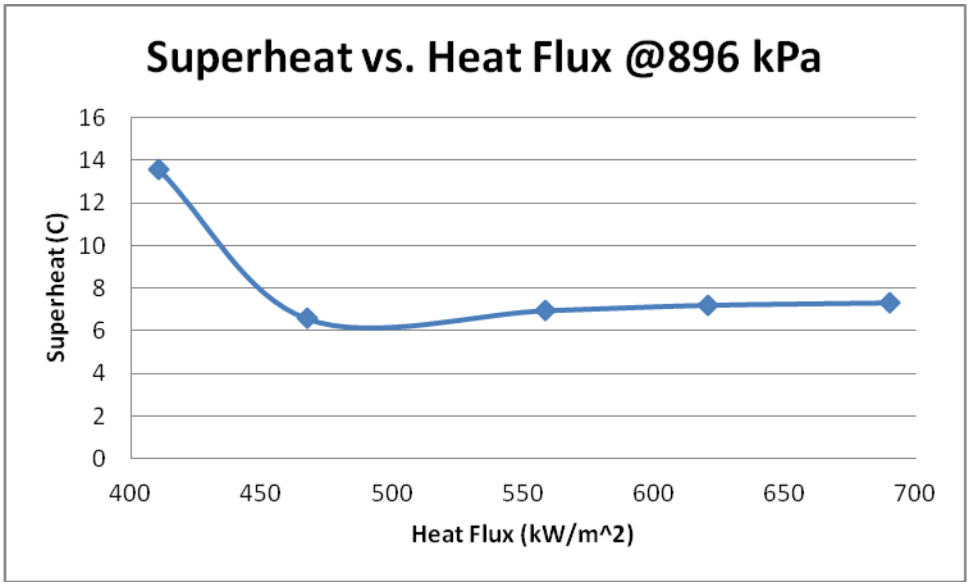

Figure 85: Superheat vs. Heat Flux @896 kPa, G=1212.1 kg/m^{2}s

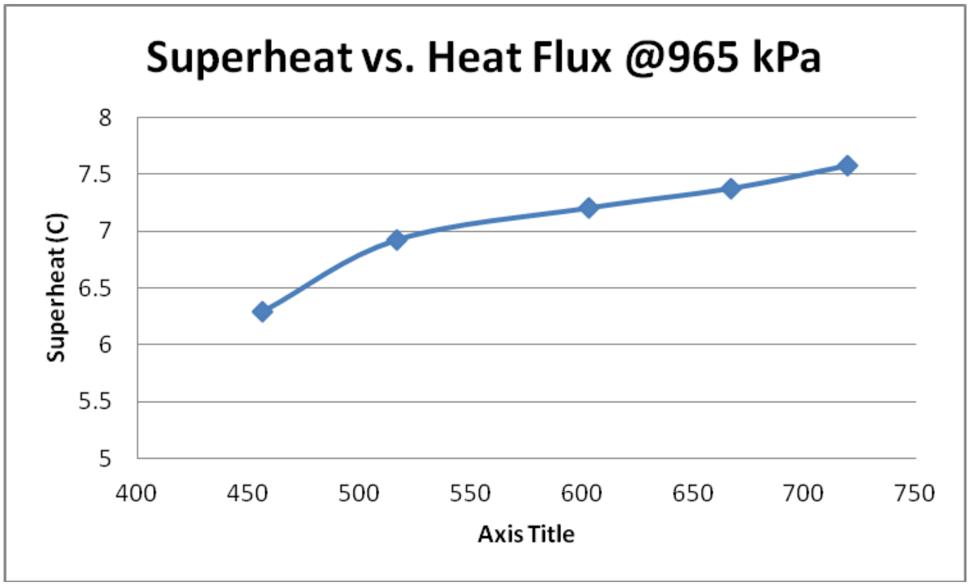

Figure 86: Superheat vs. Heat Flux @965 kPa, G=1212.1 kg/m^{2}s

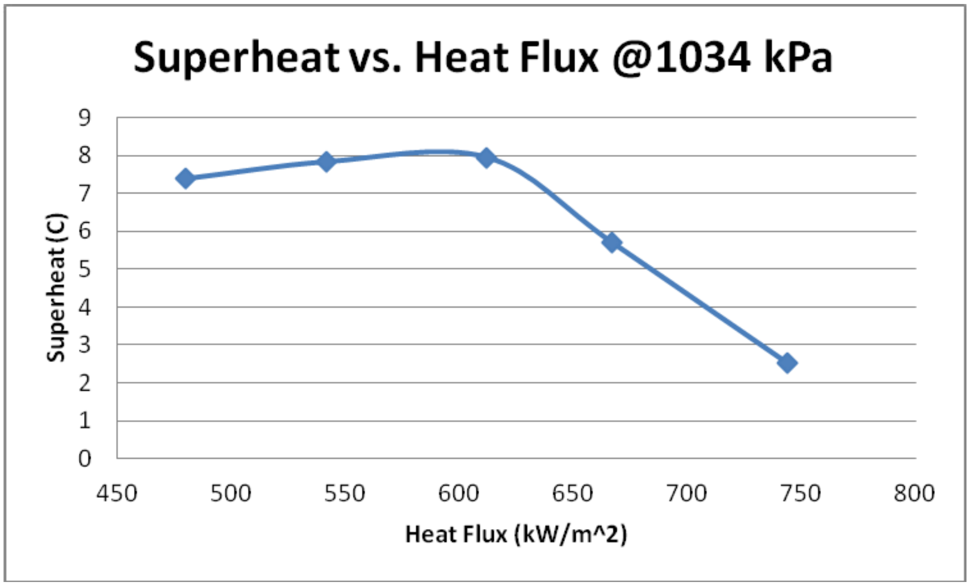

Figure 87: Superheat vs. Heat Flux @1034 kPa, G=1212.1 kg/m^{2}s

Effect of Heat Flux on Departure Bubble Size

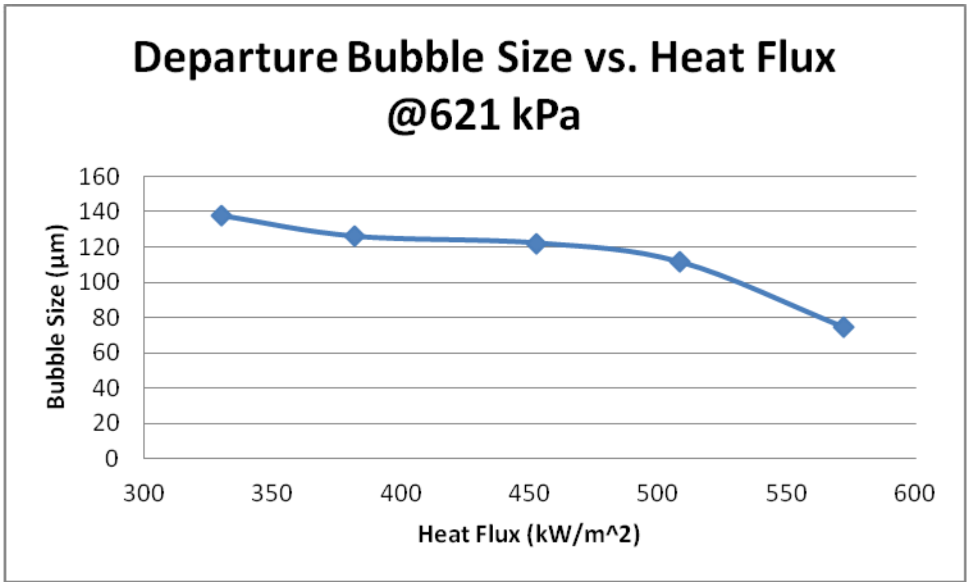

Figure 88: Departure Bubble Size vs. Heat Flux @621 kPa, G=1212.1 kg/m^{2}s

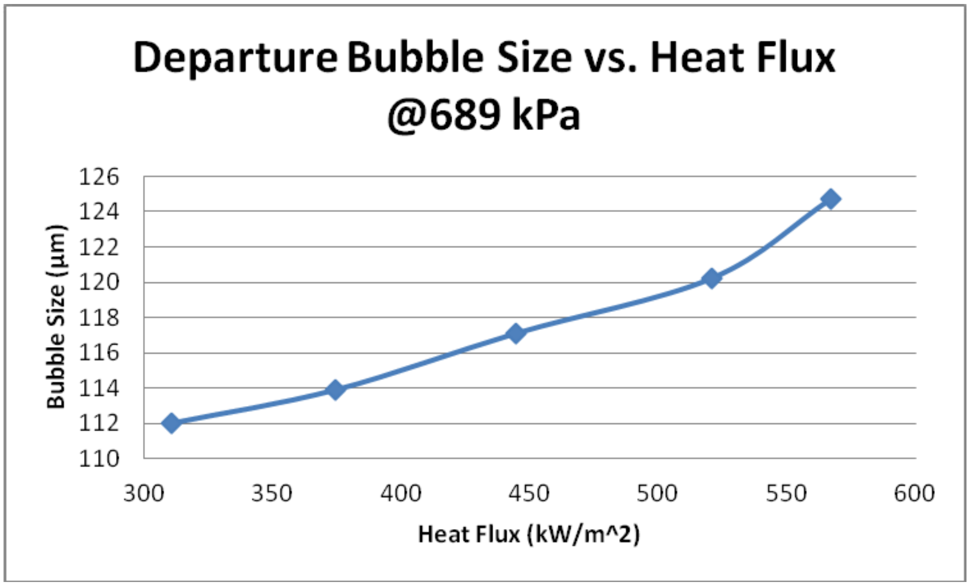

Figure 89: Departure Bubble Size vs. Heat Flux @689 kPa, G=1212.1 kg/m^{2}s

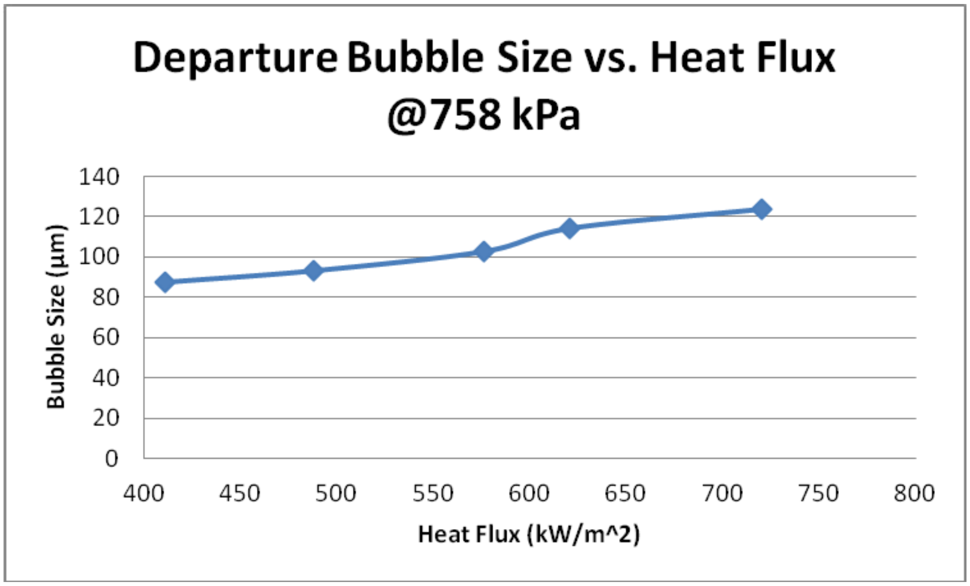

Figure 90: Departure Bubble Size vs. Heat Flux @758 kPa, G=1212.1 kg/m^{2}s

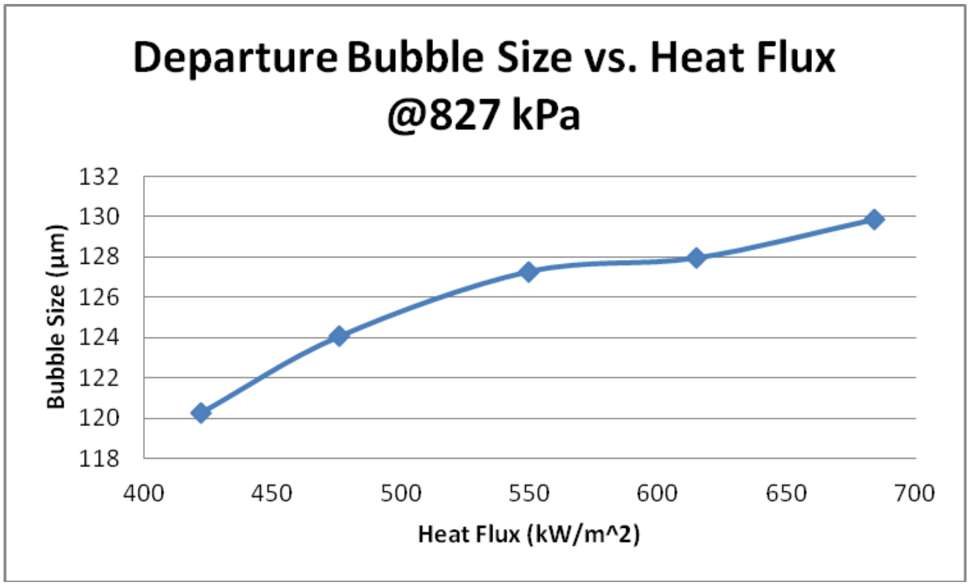

Figure 91: Departure Bubble Size vs. Heat Flux @827 kPa, G=1212.1 kg/m^{2}s

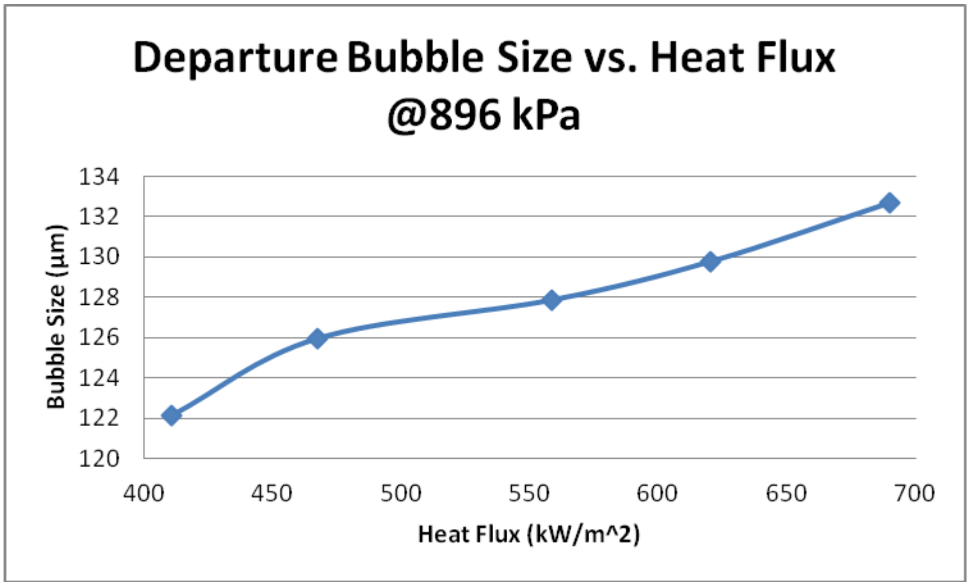

Figure 92: Departure Bubble Size vs. Heat Flux @896 kPa, G=1212.1 kg/m^{2}s

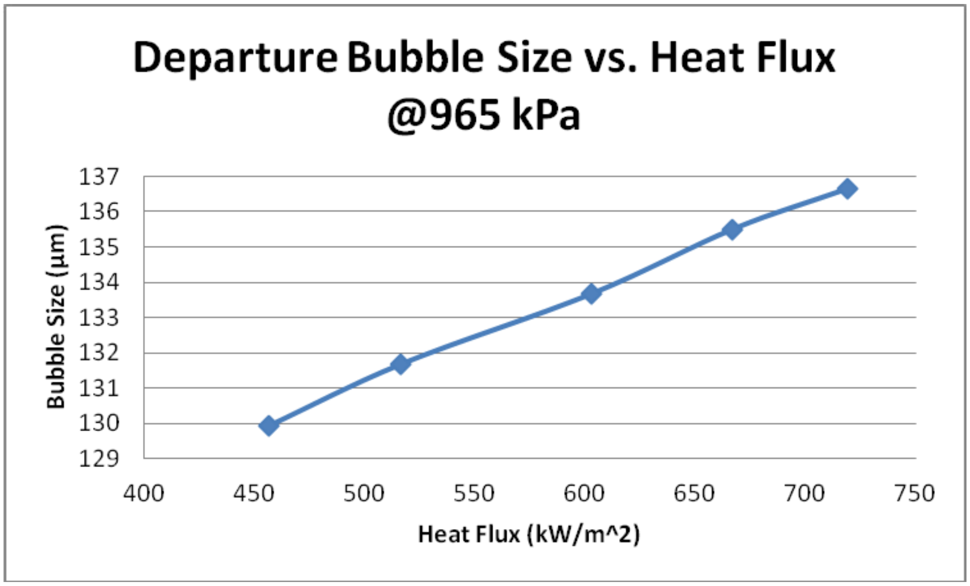

Figure 93: Departure Bubble Size vs. Heat Flux @965 kPa, G=1212.1 kg/m^{2}s

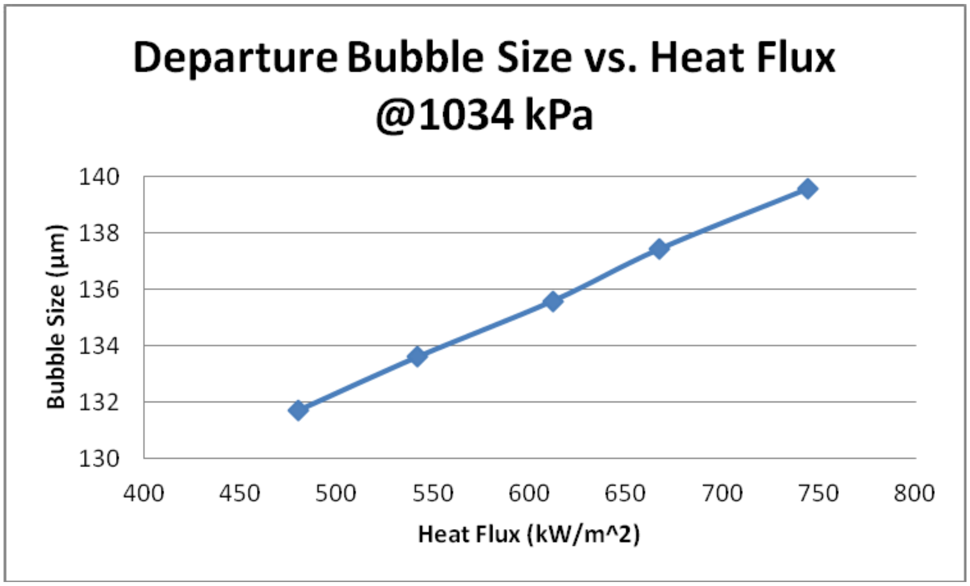

Figure 94: Departure Bubble Size vs. Heat Flux @1034 kPa, G=1212.1 kg/m^{2}s

<u>Effect of Heat Flux on Bubble Frequency</u>

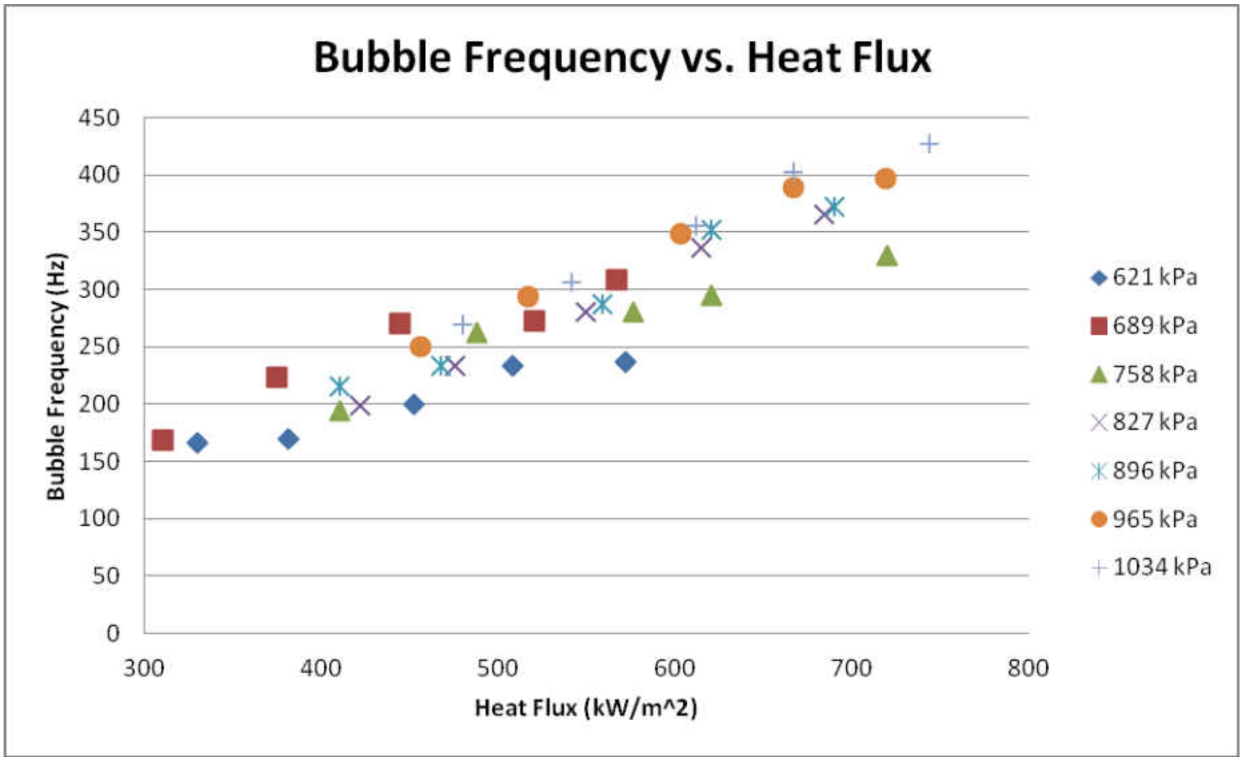

Figure 95: Bubble Frequency vs. Heat Flux, G=1212.1 kg/m^{2}s, 621 kPa to 1034 kPa

LIST OF REFERENCES

[1] R. Abernethy, R. Benedict and R. Dowdell. ASME measurement uncertainty. *Journal of Fluids Engineering 107(2),* pp. 161-163. 1985.

[2] S. Ashforth-Frost and U. Rüdel. Thermal and hydrodynamic visualisation of a water jet impinging on a flat surface using microencapsulated liquid crystals. *International Journal of Fluid Dynamics 7(1),* pp. 1-7. 2002.

[3] H. Auracher and M. Buchholz. Experiments on the fundamental mechanisms of boiling heat transfer. *Journal of the Brazilian Society of Mechanical Sciences and Engineering 27*pp. 1-22. 2005.

[4] S. Bakrania and A. M. Anderson. A transient technique for calibrating thermochromic liquid crystals: The effects of surface preparation, lighting and overheat. 2002, .

[5] I. C. Bang, S. H. Chang and W. P. Baek. Visualization of the subcooled flow boiling of R-134a in a vertical rectangular channel with an electrically heated wall. *Int. J. Heat Mass Transfer 47(19-20),* pp. 4349-4363. 2004.

[6] N. Basu, G. R. Warrier and V. K. Dhir. Onset of nucleate boiling and active nucleation site density during subcooled flow boiling. *Journal of Heat Transfer 124*pp. 717. 2002.

[7] J. W. Baughn. Liquid crystal methods for studying turbulent heat transfer. *Int J Heat Fluid Flow 16(5),* pp. 365-375. 1995.

[8] C. Buffone, K. Sefiane and J. Christy. Experimental investigation of the hydrodynamics and stability of an evaporating wetting film placed in a temperature gradient. *Appl. Therm. Eng. 24(8-9),* pp. 1157-1170. 2004.

[9] C. M. Callizo. Flow boiling heat transfer in single vertical channels of small diameter.

[10] V. P. Carey. *Liquid-Vapor Phase-Change Phenomena: An Introduction to the Thermophysics of Vaporization and Condensation Processes in Heat Transfer Equipment* 1992.

[11] J. Chen. Correlation for boiling heat transfer to saturated fluids in convective flow. *Industrial & Engineering Chemistry Process Design and Development 5(3),* pp. 322-329. 1966.

[12] P. H. Chen, P. P. Ding and D. Ai. An improved data reduction method for transient liquid crystal thermography on film cooling measurements. *Int. J. Heat Mass Transfer 44(7),* pp. 1379-1387. 2001.

[13] R. Cole and W. Rohsenow. Correlation of bubble departure diameters for boiling of saturated liquids. Presented at Chem. Eng. Prog. Symp. Ser. 1969, .

[14] V. Dhir. Boiling heat transfer. *Annu. Rev. Fluid Mech. 30(1),* pp. 365-401. 1998.

[15] M. C. Díaz, H. Boye, I. Hapke, J. Schmidt, Y. Staate and Z. Zhekov. Investigation of flow boiling in narrow channels by thermographic measurement of local wall temperatures. *Microfluidics and Nanofluidics 2(1),* pp. 1-11. 2006.

[16] X. Fu, P. Zhang, C. Huang and R. Wang. Bubble growth, departure and the following flow pattern evolution during flow boiling in a mini-tube. *Int. J. Heat Mass Transfer 53(21-22),* pp. 4819-4831. 2010.

[17] W. Grassi, D. Testi, D. Della Vista and G. Torelli. Calibration of a sheet of thermosensitive liquid crystals viewed non-orthogonally. *Measurement 40(9-10),* pp. 898-903. 2007.

[18] L. Guo, S. Zhang, Y. Chen and L. Cheng. Study on bubble dynamics of boiling in vertical rectangular mini-channel. Presented at Computer and Communication Technologies in Agriculture Engineering (CCTAE), 2010 International Conference on.

[19] C. Höhmann and P. Stephan. Microscale temperature measurement at an evaporating liquid meniscus. *Exp. Therm. Fluid Sci. 26(2-4),* pp. 157-162. 2002.

[20] Y. Y. Hsieh, L. J. Chiang and T. F. Lin. Subcooled flow boiling heat transfer of R-134a and the associated bubble characteristics in a vertical plate heat exchanger. *Int. J. Heat Mass Transfer 45(9),* pp. 1791-1806. 2002.

[21] P. T. Ireland, A. J. Neely, D. R. H. Gillespie and A. J. Robertson. Turbulent heat transfer measurements using liquid crystals1. *Int J Heat Fluid Flow 20(4),* pp. 355-367. 1999.

[22] P. Ireland and T. Jones. Liquid crystal measurements of heat transfer and surface shear stress. *Measurement Science and Technology 11*pp. 969. 2000.

[23] P. Ireland and T. Jones. The response time of a surface thermometer employing encapsulated thermochromic liquid crystals. *Journal of Physics E: Scientific Instruments 20*pp. 1195. 1987.

[24] D. Joo. Experiments in pool boiling heat transfer and nucleation dynamics of high pressure refrigerants. 2006.

[25] D. Joo and R. Kumar. Experiments in nucleation dynamics of high pressure refrigerant in pool boiling using thermo liquid crystals. *ASME 2007(43025),* pp. 325-331. 2007.

[26] S. G. Kandlikar. Nucleation characteristics and stability considerations during flow boiling in microchannels. *Exp. Therm. Fluid Sci. 30(5),* pp. 441-447. 2006.

[27] S. G. Kandlikar. Critical heat flux in subcooled flow boiling—An assessment of current understanding and future directions for research. *Multiphase Science and Technology 13(3-4),* pp. 105-130. 2001.

[28] S. G. Kandlikar. Bubble behavior and departure bubble diameter of bubbles generated over nucleating cavities in flow boiling. Presented at Pool and External Flow Boiling, Eds. V. K. Dhir and AE Bergles, Proceedings of the Engineering Foundaton Conference.

[29] S. G. Kandlikar, V. R. Mizo and M. D. Cartwright. Investigation of bubble departure mechanism in subcooled flow boiling of water using high-speed photography. Presented at Convective Flow Boiling: Proceedings of Convective Flow Boiling, an International Conference Held at the Banff Center for Conferences, Banff, Alberta, Canada, April 30-may 5, 1995. 1996, .

[30] S. G. Kandlikar and M. E. Steinke. Flow boiling heat transfer coefficient in minichannels–correlation and trends. Presented at Proc. of 12th Int. Heat Transfer Conference, Grenoble, France, Paper. 2002.

[31] S. G. Kandlikar, M. Steinke, S. Tian and L. A. Campbell. High-speed photographic observation of flow boiling of water in parallel mini-channels. Presented at Proc. of 35 The National Heat Transfer Conference, ASME.

[32] D. Kenning, T. Kono and M. Wienecke. Investigation of boiling heat transfer by liquid crystal thermography. *Exp. Therm. Fluid Sci. 25(5),* pp. 219-229. 2001.

[33] D. B. R. Kenning and Y. Yan. Pool boiling heat transfer on a thin plate: Features revealed by liquid crystal thermography. *Int. J. Heat Mass Transfer 39(15),* pp. 3117-3137. 1996.

[34] W. K. Kuan and S. G. Kandlikar. Experimental study on saturated flow boiling critical heat flux in microchannels. Presented at Proceedings of the 4th International Conference on Nanochannels, Microchannels and Minichannels. 2006, .

[35] J. M. Le Corre, S. C. Yao and C. H. Amon. Two-phase flow regimes and mechanisms of critical heat flux under subcooled flow boiling conditions. *Nucl. Eng. Des. 240(2),* pp. 245-251. 2010.

[36] J. Lee and I. Mudawar. Two-phase flow in high-heat-flux micro-channel heat sink for refrigeration cooling applications: Part II—heat transfer characteristics. *Int. J. Heat Mass Transfer 48(5),* pp. 941-955. 2005.

[37] D. N. Licu, M. J. Findlay, I. S. Gartshore and M. Salcudean. Transient heat transfer measurements using a single wide-band liquid crystal test. *Journal of Turbomachinery 122*pp. 546. 2000.

[38] C. Martín-Callizo, R. Ali and B. Palm. New experimental results on flow boiling of R-134a in a vertical microchannel. *UK Heat Transfer 2007 Proceedings* pp. 10-11. 2007.

[39] C. Martín-Callizo, B. Palm and W. Owhaib. Subcooled flow boiling of R-134a in vertical channels of small diameter. *Int. J. Multiphase Flow 33(8),* pp. 822-832. 2007.

[40] C. Martín-Callizo, B. Palm, W. Owhaib and R. Ali. Flow boiling visualization of R-134a in a vertical channel of small diameter. *Journal of Heat Transfer 132*pp. 031503. 2010.

[41] I. Mudawar. Assessment of high-heat-flux thermal management schemes. *Components and Packaging Technologies, IEEE Transactions on 24(2),* pp. 122-141. 2001.

[42] S. M. S. Murshed, K. Vereen, D. Strayer and R. Kumar. An experimental investigation of bubble nucleation of a refrigerant in pressurized boiling flows. *Energy 35(12),* pp. 5143-5150. 2010.

[43] R. Muwanga and I. Hassan. A flow boiling heat transfer investigation of FC-72 in a microtube using liquid crystal thermography. *Journal of Heat Transfer 129*pp. 977. 2007.

[44] C. Ong and J. Thome. Macro-to-microchannel transition in two-phase flow: Part 2-flow boiling heat transfer and critical heat flux. *Exp. Therm. Fluid Sci.* 2011.

[45] M. Parsley. The use of thermochromic liquid crystals in research applications, thermal mapping and non-destructive testing. Presented at Semiconductor Thermal Measurement and Management Symposium, 1991. SEMI-THERM VII. Proceedings., Seventh Annual IEEE. 1991, .

[46] X. F. Peng, H. Y. Hu and B. X. Wang. Boiling nucleation during liquid flow in microchannels. *Int. J. Heat Mass Transfer 41(1),* pp. 101-106. 1998.

[47] M. Piasecka and M. E. Poniewski. Hysteresis phenomena at the onset of subcooled nucleate flow boiling in microchannels. *Heat Transfer Eng. 25(3),* pp. 44-51. 2004.

[48] V. Prodanovic, D. Fraser and M. Salcudean. Bubble behavior in subcooled flow boiling of water at low pressures and low flow rates. *Int. J. Multiphase Flow 28(1),* pp. 1-19. 2002.

[49] W. L. Qu and I. Mudawar. Flow boiling heat transfer in two-phase micro-channel heat sinks - I. experimental investigation and assessment of correlation methods. *Int. J. Heat Mass Transfer 46(15),* pp. 2755-2771. 2003.

[50] D. Sabatino, T. Praisner and C. Smith. A high-accuracy calibration technique for thermochromic liquid crystal temperature measurements. *Exp. Fluids 28(6),* pp. 497-505. 2000.

[51] R. Situ, M. Ishii, T. Hibiki, J. Tu, G. H. Yeoh and M. Mori. Bubble departure frequency in forced convective subcooled boiling flow. *Int. J. Heat Mass Transfer 51(25-26),* pp. 6268-6282. 2008.

[52] C. Smith, D. Sabatino and T. Praisner. Temperature sensing with thermochromic liquid crystals. *Exp. Fluids 30(2),* pp. 190-201. 2001.

[53] J. Stasiek and T. Kowalewski. Thermochromic liquid crystals applied for heat transfer research. *Opto-Electronics Review 10(1),* pp. 1-10. 2002.

[54] M. E. Steinke and S. G. Kandlikar. An experimental investigation of flow boiling characteristics of water in parallel microchannels. *Journal of Heat Transfer-Transactions of the Asme 126(4),* pp. 518-526. 2004.

[55] G. E. Thorncroft, J. F. Klausner and R. Mei. An experimental investigation of bubble growth and detachment in vertical upflow and downflow boiling. *Int. J. Heat Mass Transfer 41(23),* pp. 3857-3871. 1998.

[56] L. Tong and Y. S. Tang. *Boiling Heat Transfer and Two-Phase Flow* 1997.

[57] T. Tran, M. Wambsganss, M. Chyu and D. France. A correlation for nucleate flow boiling in small channels. Presented at Compact Heat Exchangers for the Process Industries Conference, Snowbird, UT (United States), 22-27 Jun 1997. 1997, .

[58] G. Vogel, A. Graf, J. Von Wolfersdorf and B. Weigand. A novel transient heater-foil technique for liquid crystal experiments on film-cooled surfaces. *Journal of Turbomachinery 125*pp. 529. 2003.

[59] W. Zhang, T. Hibiki and K. Mishima. Correlation for flow boiling heat transfer in mini-channels. *Int. J. Heat Mass Transfer 47(26),* pp. 5749-5763. 2004.

[60] H. Zhang, I. Mudawar and M. M. Hasan. Investigation of interfacial behavior during the flow boiling CHF transient. *Int. J. Heat Mass Transfer 47(6-7),* pp. 1275-1288. 2004.